

# **A study of InAs nanowires based quantum structures for use in optoelectronic devices**

Hayfaa Raheem Abdulkareem Alradhi

Master of Physics



Physics

Department of Physics

Lancaster University

April 2018

A thesis submitted to Lancaster University for the degree of  
Doctor of Philosophy in the Faculty of Science and Technology

# Abstract

Due to increasing demand of nanowires (NWs) in the areas of electrical and photonic devices applications, it is imperative to try to improve their properties that are found to degrade their device performances. This thesis provides an extensive investigation of InAs based NWs for use in the photodetection applications. To achieve this goal, the structural and optical properties of InAs NWs and InAs NW-based quantum materials (e.g., InAsSb NWs, InAs/AlSb NWs and InAs/GaSb core-shell NWs) have been investigated.

The NW samples were grown by molecular beam epitaxy (MBE); self-catalysed droplet epitaxy was used as the growth mechanism for them. To improve the optical properties of InAs NWs, we further optimised the MBE growth for the NWs based on our previous growth understanding, which resulted in InAs NWs give strong room temperature photoluminescence (PL) at room temperature. We also notified that the substrate doping type gives significant effect on PL emission. In order to improve the axial growth rate for the epitaxy of NW devices, we developed a new 3-step growth technique: step 1 – droplet seeding, step – 2: NW growth initiation, step - 3 NW growth at high growth rate. The above new growth method yielded high quality InAs NWs with much higher axial growth rate compared to conventional growth methods. This method offers cost-effectiveness and reduction in time consumption. The NW samples grown by this method demonstrated denser, longer and enhanced optical properties.

The thesis also studied the incorporation of Sb into the InAs NWs to synthesis InAsSb NWs which is very challenging but has many interesting device applications. Through

comprehensive growth study, we demonstrated the realization of InAsSb NWs with increased Sb content through reducing growth rate of the NWs. For the first time, we produced optically active InAsSb NWs with 19% of Sb content which gives PL emission at a long wavelength of 5.1  $\mu\text{m}$  at 10 K. This achievement reveals that our InAsSb NWs could be used for infrared photodetectors and emitters operating in entire mid wavelength infrared spectral range (MWIR), e.g. 3-5  $\mu\text{m}$ .

It is well known that NW structures suffer from severe surface states which degrade the resulting devices performance, due to the large surface to volume ratio. To overcome this problem, in this thesis, we developed several advanced NW-based quantum materials with a core-shell structure (heterojunction), e.g., the NW core is passivated with shell layer of different material. Two novel core-shell NW materials namely, InAs/AlSb and InAs/GaSb were grown. Transmission electron microscopy (TEM) and electron diffraction x-ray (EDX) confirmed the success of the core-shell structure. More importantly, the PL study indicates a massive enhancement in the PL emission, by 5 times in comparison with the bare InAs NWs. Temperature dependence PL measurements proved that surface states were significantly eliminated. Our core-shell NW structure is a great success in surface passivation.

Mesa device of bare InAs NWs were fabricated and its current-voltage (I-V) were tested in room temperature. I-V measurements showed that the NW device is a working device with relatively high dark current of 0.0011A and negative photocurrent of  $(-8.9526 \times 10^4 \text{A})$ .

Single NW field effect transistors (FET) were fabricated using bare InAs NWs and InAs/ AlSb core-shell NWs and operated as photodetectors. The dark current measurements reveal that the bare InAs NW device gives a high dark current  $1.5 \times 10^{-6}$  A, while the core-shell NW device has a much more suppressed dark current of

$2.8 \times 10^{-8}$  A, which is 186 times less than bare InAs NW device. This is a further evidence of the surface passivation induced by the shell layer, which is important for fabricating photodetectors with high directivity. The photocurrent study show that the bare InAs device gives a photocurrent of 0.2  $\mu\text{m}$  leading to a signal-to-noise ratio of 13%, while core-shell NW devices exhibited anomalous photocurrent behaviour, e.g. The device gives a signal-to-noise ratio of 80%, which is 6 times higher than the bare InAs NW device. These striking device properties were attributed to the efficient surface passivation caused by the shell layer of the materials. The anomalous photocurrent behavior was attributed to the trap centres in the shell layer. Our study demonstrates the great potential of the core-shell structure in the use of highly efficient infrared photodetectors.

# **Declaration**

This thesis is my own work and no portion of the work referred to in this thesis has been submitted in support of an application for another degree or qualification at this or any other institute of learning.

# Acknowledgment

First and foremost, I would like to thank my lord (ALLAH) for blessing me to start and finish this work. I would like to express my deep gratitude and appreciation to my beloved parents, to whom I owe my being and existing.

I would like to thank my supervisor Dr. Qiandong Zhuang for all his support, guidance and encouragement. His deep knowledge of the MBE growth and semiconductor nanostructures has been of immense help to my research. My profound and gratitude to Prof. Colin Lambert.

I also want to thank my external collaborators Dr Ana M. Sanchez of the department of Physics, University of Warwick, Coventry for assistance with HRTEM measurements; Prof. Ken Durose, Peter Yates for their help with SEM and Dr. Ian Sandall for his help in fabricating mesa NW devices. As well as I would like to thank Dr. Wojcioech Linhart and prof Robert Kudrawiec of faculty of fundamental problems of technology Wroclaw, Poland, for assistance in PL measurements. Dr. Handong Li and Prof. Zhiming Wang of institute of fundamental and frontier sciences, university of electronic science and technology of China, Chengdu, China. Dr. Hehai Fang and Prof Weida Hu of state key laboratory of infrared physics Shanghai, China for the help in the devices. I am so grateful to Dr Stuart Lawson, Dr. Nathan Halcovitch for their help with X-ray diffraction and Dr. Sara Baldock for her assistance with SEM in Chemistry department, Lancaster University.

I am also grateful to my past office mates Dr. Kylie O'shea, Dr. Claire Tinker-Mill, Dr. Ezekiel Anyebe, Dr Samuel Harrison, Dr. Alex Robson Dr Jonathan Hayton , Dr Michael Thompson, Dr. Juanita Asirvatham, Dr. Qi Lu and Dr. and Dr. Aiyeshah

Alhodaib, current PhD students in my office, Zhiming Jin , James Keen ,Veronica Letka, Laura Hanks, Denise Cardenes, Eli Castanon, Eva Menendez and Furat Al-Saymari.

I would like to thank the Iraqi ministry of higher education and scientific research for their sponsorship throughout my PhD.

I would like to express my thankfulness and gratitude to my beloved husband Mr. Muayad Al-zubaidi for his unlimited support. Thanks for your encouragement assistance in good and difficult time. I greatly appreciate your patience and understanding at times when you needed my attention but I was glued to my work and unavailable. Thanks to my children, Ghadeer, Hayder and Hasanain for their understanding for my absence while they desperately needed me. Finally, a great thank for all my brothers and sisters for their support encouragement.

# List of Publications and presentations

## Journal Papers

1. Q D Zhuang, H Alradhi, Z M Jin, X R Chen, J Shao, X Chen, Ana M Sanchez, Y C Cao, J Y Liu, P Yates, K Durose and C J Jin. “Optically efficient InAsSb nanowires for silicon-based mid-wavelength infrared optoelectronics” *Nanotechnology* 28,105710(2017).
2. Xiren Chen, Qiandong Zhuang, H. Alradhi, Zh. M. Jin, Liangqing Zhu, Xin Chen, and Jun Shao. “Midinfrared Photoluminescence up to 290 K Reveals Radiative Mechanisms and Substrate Doping-Type Effects of InAs Nanowires”. *Nanoletter* 17, 1545 (2017).
3. Handong Li, Hayfaa Alradhi, Zhiming Jin, Ezekiel A. Anyebe, Ana M. Sanchez, Wojciech M. Linhart, Robert Kudrawiec, Hehai Fang, Zhiming Wang, Weida Hu, and Qiandong Zhuang. “Novel Type-II InAs/AlSb Core–Shell Nanowires and Their Enhanced Negative Photocurrent for Efficient Photodetection”. *Advanced functional materials* 28, 1705382(2018).

## Conference Presentations

1. H. Alradhi, A. Ezek, A. Sanchez, A. zhuko and Q. Zhuang. “ X-ray diffraction study of InAsSb nanowires grown by molecular beam epitaxy”. UK semiconductors 2015,(poster presentation).
2. Hayfaa Alradhi, X. R. Chen, J. Shao, Zhiming Jin, A. M. Sanchez, P. Yates, K. Durose, and Q. D. Zhuang. “Realization of InAs/AlSb core-shell nanowires by MBE with enhanced optical properties” Nanowires workshop, Spain , Barcelona 2015 , (poster presentation).
3. Hayfaa Alradhi, Zhiming Jin, A. M. Sanchez, P. Yates, K. Durose, and Q. D. Zhuang. “Realization of InAs/AlSb core-shell NWs grown by MBE”. Lancaster University Science and Technology Christmas Conference 2015 (Poster presentation).
4. Q. D. Zhuang, H. Alradhi, X. R. Chen, J. Shao, H. H. Fang, W. D Hu, S. H. Hu., Z. M. Jin, A. M. Sanchez. “InAs/AlSb core-shell nanowires with enhanced optical properties for phototransistors” ICMBE Montpellier, France 2016(oral presentation).
5. H. Alradhi, J. Zhiming, A. Sanchez, P. Yates, K. Durose X Chen, J Shao and optically efficient InAsSb/GaSb core-shell nanowires grown by molecular beam epitaxy. Conference: European Workshop on Molecular Beam Epitaxy at: St Petersburg, Russia 2017 (poster presentation)Z. Jin, E. Anybe, H. Alradhi, I. Sandall, A Sanchez, T. D Veal, M. Rajpalke, Y.C. Cao, H.D. Li, R. Harvey and

# Contents

Abstract.....	i
Declaration.....	ii
Acknowledgements .....	iii
List of Publications and Presentations .....	iv
Contents.....	v
<b>Chapter 1 Introduction .....</b>	<b>1</b>
1.1 Infra-red photodetector .....	1
1.2 The significance of NWs .....	2
1.3 The Challenges of NWs.....	3
<b>Chapter 2 Theoretical Concepts.....</b>	<b>10</b>
2.1 InAs crystal structure and the crystalline defects in nanowires.....	10
2.2 NWs growth technique and mechanisms.....	12
2.2.1 The vapor- liquid -solid process.....	13
2.2.2 The vapor solid process.....	16
2.3 Self-catalysed droplet epitaxy (DE)for InAs nanowires.....	16
2.4 Substrate orientation and NWs growth direction.....	17
2.5 Carrier occupation and Fermi level.....	17
2.6 Direct and indirect bandgap semiconductor.....	18
2.7 Bandgap engineering.....	19
2.8 Temperature dependence of the bandgap.....	20
2.9 Energy band alignment .....	20
2.9.1 Type I band alignment .....	21
2.9.2 Type II band alignment .....	21
2.9.3 Type III band alignment.....	22
2.10 Recombination Mechanisms.....	22
2.10.1 Band-to-Band recombination.....	23
2.10.2 Free to bound recombination.....	23
2.10.3 Donor to acceptor pair recombination.....	24
2.10.4 Exciton recombination .....	24
2.11 Non-radiative recombination .....	24
2.11.1 Surface recombination.....	25
2.11.2 Auger recombination .....	25
2.11.3 Shockley-Read-Hall Recombination .....	26
2.12 p-n junction .....	26
2.13 Photodetector and Principle of Operation .....	27

2.13.1	A p-i-n photodetector .....	28
2.13.2	Heterostructure photodetector .....	29
2.13.3	Metal-semiconductor photodiode .....	29
2.14	Photodetector characterization parameters .....	30
2.14.1	Quantum efficiency EQE ( $\eta$ ) .....	30
2.14.2	Internal quantum efficiency IQE ( $\eta_i$ ) .....	30
2.14.3	Responsivity ( $R_\lambda$ ) .....	31
2.14.4	Noise equivalent power (NEP) .....	31
<b>Chapter 3 Literature Review.....</b>		<b>36</b>
3.1	History of IR photodetector .....	36
3.2	InAsSb NWs photodetector .....	40
3.4	InAs and InAsSb NWs.....	43
3.5	Core-shell NWs.....	46
3.5.1	InAs/GaSb core-shell nanowires.....	46
3.5.2	InAs/AlSb core-shell NWs.....	49
<b>Chapter 4 Experimental Techniques.....</b>		<b>59</b>
4.1	Molecular Beam Epitaxy.....	59
4.1.1	MBE apparatus.....	59
4.1.2	Reflection high energy electron diffraction (RHEED).....	61
4.2	X-Ray diffraction (XRD).....	62
4.2.1.	Determination lattice parameters.....	64
4.2.2.	Determining the composition of the nanowires.....	65
4.3	Scanning Electron Microscopy (SEM).....	67
4.4	Transmission Electron Microscopy (TEM).....	69
4.5	Atomic force microscopy (AFM).....	72
4.6	Photoluminescence measurements.....	74
4.7	Current-Voltage measurements.....	76
<b>Chapter 5 Growth and Structural Analysis.....</b>		<b>80</b>
5.1	Introduction.....	80
5.2	Growth procedure of InAs nanowires by In-assisted droplet epitaxy.....	81
5.2.1	Substrate preparation.....	81
5.2.2.	Epitaxial growth details.....	82
5.2.3	Morphological and structural characteristics.....	83
5.2.4	Growth optimizing of InAs NWs.....	84
5.3	Growth of InAsSb NWs.....	86
5.3.1.	Epitaxial growth details.....	86
5.4	Growth of InAs/AlSb core-shell NWs.....	88
5.4.1	Epitaxial growth details.....	88

5.4.2.	Morphological and structural characteristics.....	89
5.5	Growth InAs/GaSb core-shell NWs.....	96
5.5.1	Epitaxial growth details.....	96
5.5.2	Morphological and structural characteristics.....	97
5.6	Summary.....	101

## **Chapter 6 Photoluminescence Properties of NWs.....107**

6.1	Introduction.....	105
6.2	Optical properties of bare InAs NWs.....	108
6.3	Low temperature (10 K) Photoluminescence of InAsSb nanowires.....	111
6.4	The effect of substrate doping type on 8-290K Photoluminescence of InAs NWs.....	116
6.5	PL of core-shell NWs.....	121
6.6	Summary.....	125

## **Chapter 7 Device Characterisation.....130**

7.1	Introduction.....	130
7.2	Conventional InAs NW ensemble Photodetectors.....	130
7.2.1	Device design and structure.....	130
7.2.2	I-V characterization.....	132
7.3	Single InAs NW and InAs/AlSb core-shell NWs Phototransistor .....	134
7.3.1	Device design and structure.....	134
7.3.2	Device characterization.....	135
7.4	Summary.....	140

## **Chapter 8 Conclusion.....143**

8.1	Summary of achievement.....	143
8.2	Structural and optical characterisation.....	143
8.3	Device characterisation.....	146
8.4	Outlook and future suggestions.....	147

# Chapter 1

## Introduction

### 1.1 Infrared-photodetectors:

Photodetectors are semiconductor devices that convert the optical signal into electrical current. They have been used widely, in military applications (e.g., navigation, night vision, weapons detection), commercial applications (e.g., communications, aerospace, medical imaging), public applications (e.g., atmospheric sounding, pollution control, meteorology, environmental monitoring), and academic applications (e.g., astronomy)[1]. The operation principle of photodetectors is based on the quantum photoelectric effect: incident photons generate carriers, which contribute to the photocurrent/photovoltage. Their output depends on the number of absorbed photons. To initiate photoelectric emission, a certain minimum energy of the incident photon is required. Therefore, photon detectors show a wavelength dependence of response per unit of incident photon power.

There are a few dominant technologies for photodetectors in the market. The first type is based on HgCdTe (MCT) and InSb. Photodetectors based on these materials encountered weakness such as noise non-uniformity and cooling requirements for photon detector with wavelengths exceeding 3  $\mu\text{m}$ . Cooling is important to avoid thermal generation of charge carriers. Non-cooled devices are very noisy because thermal transition competes with optical ones [2, 3]. To avoid this, the device must be cooled. The cooling requirement is the most common problem in the IR systems making them heavy, bulky and expensive [4-7]. This created a need to invent a new group of materials to improve the photodetector performance.

Quantum well IR photodetectors (QWIPs) is another existing IR technology have been used as an alternative solution. They must grow on lattice-matched expensive substrates (InGaAs, InAs, InSb) and suffer from high dark current, low quantum efficiency and lack of normal incidence absorption [7]. QDIRPs based on III-V materials have some issues in their growth and in the variability in the size and shape of the dots [3, 8-10]. Type- II superlattice (T2SL) has been developed in device design because of their versatility in bandgap engineering which are not existing in other material systems. However, T2SL photodetectors have their own challenges, such as producing thick SLs structure without degrading the material quality. Thick superlattice is necessary for achieving high quantum efficiency photodiode. Considerable surface leakage is a serious problem of in T2SL which results by the discontinuity in the periodic crystal structure [6]. All the above drawbacks remain a problem for infrared photo detection.

Semiconductor nanowires are a new class of materials that can improve the photodetection technology. The small footprint of NWs makes them readily release the strain induced by the lattice-mismatch without the generation of dislocations. This feature enables epitaxial growth on inexpensive Si substrates and therefore could solve the problems detailed above.

## **1.2 The significance of nanowires**

Nanowires (NWs) are one-dimensional structures with length of the order of few microns and diameter in the range of tens to hundreds of nanometres. NWs have exhibited attractive physical properties that are not available in bulk materials, such as electrical carrier confinement in two dimensions of the NWs. Quantum confinement occurs when the wavelength of the electron in a material is of the same dimension as the material. This means that the motion of the electrons becomes quantized in the

confining dimension [9]. This implies that the energy levels of NWs will be discrete instead of continuous as found in bulk materials, as shown in Fig 1.1. All the above features make NWs favorable to optoelectronic applications. For instance, NWs have demonstrated enhanced light absorption [11], and efficient carrier separation and collection [11, 12] leading to applications in InP NW solar cells which recorded efficiency of 13.8% [13], GaAs NW solar cells with a record efficiency of 15.3% [14], InAsSb NW photodetectors [15], and III-V NW phototransistors [16].

The hybrid structure of combining III-V and silicon has attracted historic attention due to their exceptional physical properties. The conductivity of semiconductors can be enhanced using electric field. In addition, their electric properties can be controlled by adding impurities (dopants). These properties make semiconductor materials very versatile.

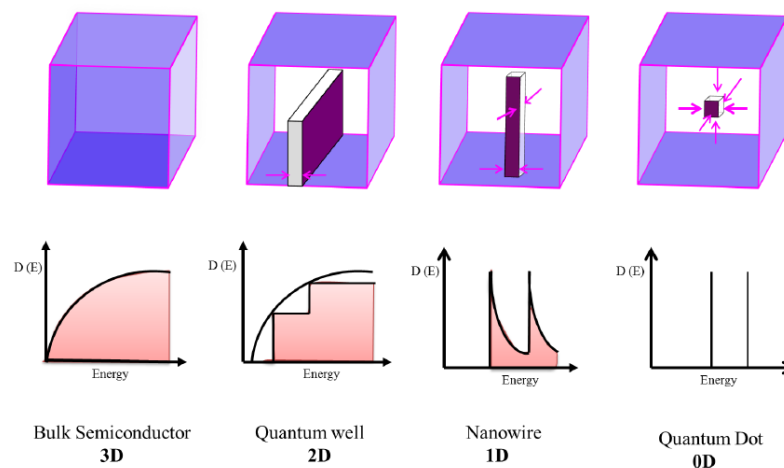


Figure 1.1: Electronic density of states for different dimensions of nanostructures.

### 1.3 Challenges of NWs

Although there are many advantages of using NWs grown on silicon substrates, several challenges still stand in the way of further improvement of NW device performance, the crystalline quality, surface states, efficient recombination and quantum

confinement. It is difficult to control the geometry and density of NWs, stacking faults, and the variations in stacking that produce mixed phases such as zinc-blende (ZB) and wurtzite (WZ) [17, 18]. These difficulties can be controlled through optimized growth conditions and the use of impurities [19] and surfactants [20, 21]. Due to the huge surface area-to-volume ratio of NWs, the surface states significantly degrade their optical and electronic properties and impede their use in optoelectronic devices [22]. This problem could be eliminated through engineering a chemically inactive surface to produce a proper surface passivation hence to prevent the formation of surface states. Several approaches have been developed including coating the surface with polymers; [23, 24]treating the NWs with chemicals [25, 26]; and monolithic growth of a shell layer to encapsulate the core NWs [27, 28]. Amongst these approaches, the latter offers several advantages, e.g. avoiding the risk of contamination and oxidation in device processing, providing a bandgap engineering capability and efficient quantum confinement if appropriate materials combinations are realized.

Many core-shell NWs based devices have been reported; such as LEDs [29-31] , solar cells [32-34] , lasers [35] and photodetectors [36, 37]. However, there are very few reports of core-shell NWs involving InAs, which is one of the most important narrow bandgap optoelectronic materials. InAs ( $E_g = 0.35\text{eV}$ ) has a very high mobility ( $8 \times 10^5 \text{ cm}^2 / \text{Vs}$  at 4.2 K), its combination with III-antimonies gives a small lattice-mismatch (about 0.66% for InAs/GaSb and 1.18% for InAs/AlSb), and has a large conduction-band offset ( $\sim 1.12\text{eV}$  for InAs/GaSb and  $\sim 1.35 \text{ eV}$  for InAs/AlSb). These factors produce excellent electron confinement. Together with its type-II bandgap alignment, InAs/antimonite heterostructures are thus promising candidates for high-speed and high performance electronic/optoelectronics devices operating in the mid wavelength infrared spectral range [38].

This thesis focuses on the growth and physical characteristics of InAs NWs, InAsSb NWs and two core-shell structures, which have the same core (InAs) but are wrapped with different shell materials, AlSb and GaSb. The study involves molecular beam epitaxial growth, structural analysis including geometry and morphology, and analysis of the optical properties. The InAs/AlSb NWs were fabricated into photodetector devices. Their characteristics and photoresponse are also presented in the thesis.

The outline of the thesis is structured as follows:

- Chapter 1 - Highlights the motivation of this thesis.
- Chapter 2 - Presents the relevant fundamentals and background theory.
- Chapter 3 - Reviews the literature related to the materials and the structures of this study.
- Chapter 4 - Shows the experimental techniques employed for growing and characterizing the NWs.
- Chapter 5 - Addresses the results of the growth and analyses the characteristics of NWs.
- Chapter 6 - Presents the results of photoluminescence measurements and optical properties of the NWs.
- Chapter 7 - Analyses the NW photodetector design and presents the results of the I-V testing.
- Chapter 8 - Concludes and addresses the possibility of future work to extend the research in this thesis.

## References

- [1] C. Downs, and T. Vandervelde, "Progress in Infrared Photodetectors Since 2000," *Sensors*, vol. 13, no. 4, pp. 5054-5098, 2013.
- [2] A. Rogalski, "Quantum well photoconductors in infrared detector technology," *Journal of Applied Physics*, vol. 93, no. 8, pp. 4355-4391, 2003.
- [3] M. Henini, and M. Razeghi, *Handbook of infrared detection technologies*: Elsevier, 2002.
- [4] A. Karim, and J. Y. Andersson, "Infrared detectors: Advances, challenges and new technologies." p. 012001.
- [5] A. Rogalski, "HgCdTe infrared detector material: history, status and outlook," *Reports on Progress in Physics*, vol. 68, no. 10, pp. 2267-2336, 2005.
- [6] A. Rogalski, "Recent progress in infrared detector technologies," *Infrared Physics and Technology*, vol. 54, no. 3, pp. 136-154, 2011.
- [7] A. V. Barve, S. J. Lee, S. K. Noh, and S. Krishna, "Review of current progress in quantum dot infrared photodetectors," *Laser & Photonics Reviews*, vol. 4, no. 6, pp. 738-750, 2010.
- [8] A. Rogalski, "Infrared detectors: an overview," *Infrared Physics and Technology*, vol. 43, no. 3, pp. 187-210, 2002.
- [9] K. A. Dick, "A review of nanowire growth promoted by alloys and non-alloying elements with emphasis on Au-assisted III-V nanowires," *Progress in Crystal Growth and Characterization of Materials*, vol. 54, no. 3, pp. 138-173, 2008.
- [10] Z. Y. Jia Zhu, George F. Burkhard, Ching-Mei Hsu, Stephen T. Connor., and Q. W. Yueqin Xu, Michael McGehee, Shanhui Fan, and Yi Cui., "Optical absorption enhancement in amorphous silicon nanowire and nanocone arrays," *Nano Letters*, vol. 9, no. 1, 2009.
- [11] Y. Vaynzof, D. Kabra, R. H. Friend, L. Zhao, P. K. H. Ho, and A. T. S. Wee, "Improved photoinduced charge carriers separation in organic- inorganic hybrid photovoltaic devices," *Applied Physics Letters*, vol. 97, no. 3, 2010.
- [12] K. Prashanthi, P. Dhandharia, N. Miriyala, R. Gaikwad, D. Barlage, and T. Thundat, "Enhanced photo- collection in single BiFeO<sub>3</sub> nanowire due to carrier separation from radial surface field," *Nano Energy*, vol. 13, pp. 240-248, 2015.

- [13] J. Wallentin, N. Anttu, D. Asoli, M. Huffman, I. Aberg, M. H. Magnusson, G. Siefert, P. Fuss-Kailuweit, F. Dimroth, B. Witzigmann, H. Q. Xu, L. Samuelson, K. Deppert, and M. T. Borgström, “InP nanowire array solar cells achieving 13.8% efficiency by exceeding the ray optics limit,” *Science (New York, N.Y.)*, vol. 339, no. 6123, pp. 1057, 2013.
- [14] I. Aberg, G. Vescovi, D. Asoli, U. Naseem, J. P. Gilboy, C. Sundvall, A. Dahlgren, K. E. Svensson, N. Anttu, M. T. Bjork, and L. Samuelson, “A GaAs nanowire array solar cell with 15.3% efficiency at 1 sun,” vol. 6, no. 1, pp. 185-190, 2015.
- [15] N. A. J. Svensson, N. Vainorius, B. M. Borg., and a. L.-E. Wernersson, “Diameter-dependent photocurrent in InAsSb nanowire infrared photodetectors,” *Nano Letter*, vol. 13, no. 4, pp. 1380-1385, 2013.
- [16] M. S. Vitiello, D. Coquillat, L. Viti, D. Ercolani, F. Teppe, A. Pitanti, F. Beltram, L. Sorba, W. Knap, and A. Tredicucci, “Room- temperature terahertz detectors based on semiconductor nanowire field- effect transistors,” *Nano letters*, vol. 12, no. 1, pp. 96, 2012.
- [17] P. Caroff, J. Bolinsson, and J. Johansson, “Crystal phases in III- V nanowires: from random toward engineered polytypism,” *IEEE Journal of Selected Topics in Quantum Electronics*, vol. 17, no. 4, pp. 829-846, 2011.
- [18] K. A. Dick, C. Thelander, L. Samuelson, and P. Caroff, “Crystal phase engineering in single InAs nanowires,” *Nano Lett.*, vol. 10, no. 9, pp. 3494-3499, 2010.
- [19] H. Shtrikman, R. Popovitz-Biro, A. Kretinin, L. Houben, M. Heiblum, M. Bukala, M. Galicka, R. Buczko, and P. Kacman, “Method for suppression of stacking faults in Wurtzite III- V nanowires,” *Nano letters*, vol. 9, no. 4, pp. 1506, 2009.
- [20] Q. Zhuang, E. A. Anyebe, R. Chen, H. Liu, A. M. Sanchez, M. K. Rajpalke, T. D. Veal, Z. Wang, Y. Huang, and H. Sun, “Sb-induced phase control of InAsSb nanowires grown by molecular beam epitaxy,” *Nano letters*, vol. 15, no. 2, pp. 1109-1116, 2015.
- [21] E. Anyebe, M. Rajpalke, T. Veal, C. Jin, Z. Wang, and Q. Zhuang, “Surfactant effect of antimony addition to the morphology of self- catalyzed InAs  $1-x$  Sb  $x$  nanowires,” *Nano Research*, vol. 8, no. 4, pp. 1309-1319, 2015.
- [22] M. H. Sun, H. J. Joyce, Q. Gao, H. H. Tan, C. Jagadish, and C. Z. Ning, “Removal of surface states and recovery of band- edge emission in InAs nanowires through surface passivation,” *Nano letters*, vol. 12, no. 7, pp. 3378, 2012.

- [23] C. K. Yong, K. Noori, Q. Gao, H. J. Joyce, H. H. Tan, C. Jagadish, F. Giustino, M. B. Johnston, and L. M. Herz, "Strong carrier lifetime enhancement in GaAs nanowires coated with semiconducting polymer," *Nano letters*, vol. 12, no. 12, pp. 6293, 2012.
- [24] X. Wang, Y. Hu, L. Song, W. Xing, H. Lu, P. Lv, and G. Jie, "Effect of antimony doped tin oxide on behaviors of waterborne polyurethane acrylate nanocomposite coatings," *Surface & Coatings Technology*, vol. 205, no. 7, pp. 1864-1869, 2010.
- [25] T. Hanrath, and B. A. Korgel, "Chemical surface passivation of Ge nanowires," *Journal of the American Chemical Society*, vol. 126, no. 47, pp. 15466, 2004.
- [26] M. Bashouti, T. Stelzner, A. Berger, S. Christiansen, and H. Haick, "Chemical Passivation of Silicon Nanowires with C-1- C-6 Alkyl Chains through Covalent Si- C Bonds," *J. Phys. Chem. C*, vol. 112, no. 49, pp. 19168-19172, 2008.
- [27] D. W. Feng Ning, Li-Ming Tang, Yong Zhang, and Ke-Qiu Chen, "The effects of the chemical composition and strain on the electronic properties of GaSb/InAs core-shell nanowires," *J. Appl. Phys.*, vol. 116, pp. 094308, 2014.
- [28] B. Ganjipour, S. Sepehri, A. W. Dey, O. Tizno, B. Mattias Borg, K. A. Dick, L. Samuelson, L.-E. Wernersson, and C. Thelander, "Electrical properties of gasb/ inassb core/ shell nanowires," *Nanotechnology*, vol. 25, no. 42, pp. 425201, 2014.
- [29] S. G. Mark, J. L. Lincoln, W. Jianfang, C. S. David, and M. L. Charles, "Growth of nanowire superlattice structures for nanoscale photonics and electronics," *Nature*, vol. 415, no. 6872, pp. 617, 2002.
- [30] C. P. T. Svensson, T. Mårtensson, J. Trägårdh, C. Larsson, M. Rask, D. Hessman, L. Samuelson, and J. Ohlsson, "Monolithic gaas/ ingap nanowire light emitting diodes on silicon," *Nanotechnology*, vol. 19, no. 30, pp. 305201, 2008.
- [31] K. Tomioka, J. Motohisa, S. Hara, K. Hiruma, and T. Fukui, "GaAs/ AlGaAs core multishell nanowire- based light- emitting diodes on Si," *Nano letters*, vol. 10, no. 5, pp. 1639, 2010.
- [32] B. M. Kayes, H. A. Atwater, and N. S. Lewis, "Comparison of the device physics principles of planar and radial p - n junction nanorod solar cells," *Journal of Applied Physics*, vol. 97, no. 11, 2005.
- [33] J. A. Czaban, D. A. Thompson, and R. R. Lapierre, "GaAs core-- shell nanowires for photovoltaic applications," *Nano letters*, vol. 9, no. 1, pp. 148, 2009.

- [34] C. Colombo, M. Heiß, M. Grätzel, and A. Fontcuberta I Morral, "Gallium arsenide p - i - n radial structures for photovoltaic applications," *Applied Physics Letters*, vol. 94, no. 17, 2009.
- [35] B. Hua, J. Motohisa, Y. Kobayashi, S. Hara, and T. Fukui, "Single GaAs/ GaAsP coaxial core- shell nanowire lasers," *Nano letters*, vol. 9, no. 1, pp. 112, 2009.
- [36] E. M. Gallo, G. Chen, M. Currie, T. McGuckin, P. Prete, N. Lovergine, B. Nabet, and J. E. Spanier, "Picosecond response times in GaAs/ AlGaAs core/ shell nanowire- based photodetectors," *Applied Physics Letters*, vol. 98, no. 24, 2011.
- [37] L. C. Chuang, F. G. Sedgwick, R. Chen, W. S. Ko, M. Moewe, K. W. Ng, T.-T. D. Tran, and C. Chang-Hasnain, "GaAs- based nanoneedle light emitting diode and avalanche photodiode monolithically integrated on a silicon substrate," *Nano letters*, vol. 11, no. 2, pp. 385, 2011.
- [38] C. Thelander, P. Caroff, S. Plissard, and K. Dick, "Electrical properties of InAs<sub>1-x</sub>Sb<sub>x</sub> and InSb nanowires grown by molecular beam epitaxy," *Applied Physics Letters*, vol. 100, no. 23, 2012.

# Chapter 2

## Theoretical concepts

This chapter presents the basic theoretical concepts relevant to this study, such as those of semiconductor materials, crystal structure, band gap alignment, recombination mechanism, p-n junction, and photodetector.

### 2.1 InAs crystal structure and the crystalline defects in nanowires

The most common crystal structure of semiconductor materials is divided into two types; cubic zincblende (ZB) structure and hexagonal or wurtzite (WZ) structure. The cubic ZB structural phase is composed of two face centre cubic (fcc) lattices shifted by one quarter along the space diagonal in (111) direction. The tetrahedral bonds between the nearest atoms are same for both phases. The sequences of ZB are composed of three distinct layers of III-V pairs, which are denoted as ABCABC, while WZ phase is described; by two repeated layers of III-V, pairs denoted by ABAB, see Fig 2.1a. InAs is similar to all other III-V materials; it crystallizes in the cubic ZB structure in bulk. However, when it is grown as nanowire, it features the hexagonal WZ phase. The major difference of these two structures is the stacking sequences along the growth direction. This stacking sequence gives the appearance of both phases for nanowires that is related to the growth direction of NWs. It is [111] direction for the cubic cell; it is in [0001] direction while in hexagonal cell.

In NW materials, pure ZB structure is the exception rather than the rule. In addition, many crystalline defects such as stacking faults; twin defects and ZB-WZ polytypism

are commonly present in it. These defects of several different types can be described below:

1. **Stacking faults:** Stacking faults (SF) occurs as a result of deviation from perfect WZ phase, which gives rise the sequence  $AB\underline{AB}|C\underline{BCB}$  with the fault line between B and C. This fault automatically creates single unit of ZB structure  $\underline{ABC}$  [1].
2. **Twin plane:** Twin plane is known as a mirror plane between two segments rotated by  $60^\circ$  from each other [2] and hence reverses the stacking sequence. In the ZB, a twin plane is created due to misplacement of a single bilayer from ABC to CBA [3, 4]. The new stacking sequence becomes  $ABC\underline{A}CBA$ , where A is the twin plane. In WZ phase, the misplacement of a single bilayer gives rise to the sequence  $ACBC\underline{B}AC$ . Based on the presentation made above, it may be noted that a single twin plane in the ZB phase cannot produce a WZ segment. In order to change the structure from ZB phase to WZ phase, it requires at least two sequential twin planes i.e;  $ABCA\underline{C}|A$ . That means the smallest WZ segment needs four bilayers, as underlined above.
3. **ZB-WZ polytypism:** Binary semiconductor nanowires such as InAs nanowires exhibit a high density of randomly distributed twin defects and stacking faults, and hence results in an uncontrolled, or polytypic, crystal structure. The polytypism results from a plane that is formed between ZB and WZ phases, and has density determining the size of segment of each phase. According to Caroff et al., for InAs, the smallest WZ segment in ZB phase should be 2.8 nm in length (ABAB). While ZB segment length should be at least 2.1 nm (ABC) to be found in WZ phase [2].

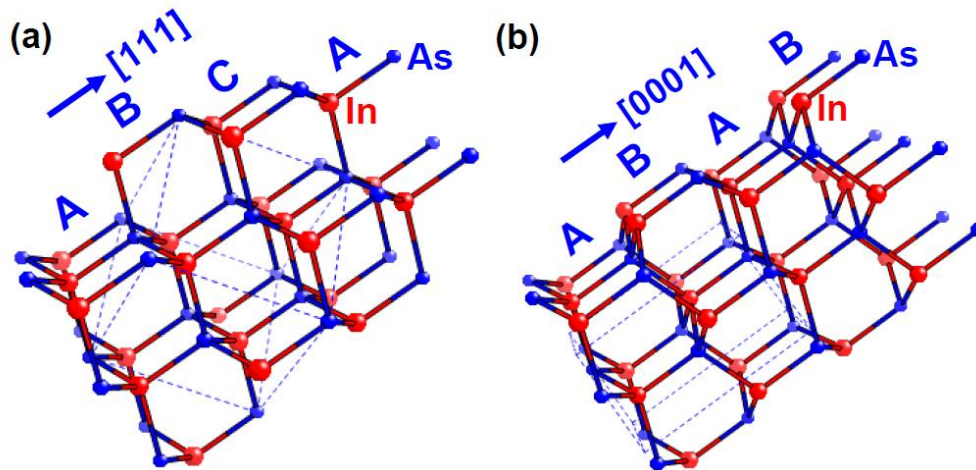


Figure 2.1: a) Schematic of the WZ crystal structure with ABAB layer stacking along the [0001] direction and (b) Schematic of the ZB crystal structure with ABCA layer stacking along the [111] direction [1].

## 2.2 NWs growth techniques and mechanisms

III-V nanowires can be synthesized by various growth techniques, including laser ablation [5, 6] chemical vapor deposition (CVD) [7-10], chemical beam epitaxy (CBE) [11], metalorganic chemical vapour deposition (MOVPE) [12-14] and molecular beam epitaxy (MBE) [15-17]. Regardless of the growth technique NWs can be grown by different mechanisms i.e metal catalysed growth mechanism such as the vapour-liquid-solid mechanism (VLS), oxide (for example,  $\text{SiO}_x$ ) assisted growth mechanism, and self-catalysed growth mechanism. All these mechanisms involve transition of the source species from the vapour phase to the solid semiconductor phase. For instance, MBE growth of InAs nanowires makes use of In and  $\text{As}_4$  beams, which when dissolved in droplet, undergo supersaturation yielding solid InAs NW by the VLS mechanism. Likewise, CVD growth of InAs nanowires make use of trimethylindium (TMIn) and arsine ( $\text{AsH}_3$ ) precursors at a substrate temperature range of 300-390 °C and on Au nanoparticles formed on Si substrate. Au and In form Au/In eutectic liquid droplet.

Subsequently, In and As dissolved in this droplet are supersaturated yielding InAs nanowires.

The self – catalysed growth of InAs nanowires does not necessarily make use of a metal catalyst and metal/In eutectic droplet. The growth is carried out by a mechanism called vapour-quasisolid-solid (VQS) mechanism. It is a corrected form of vapor-solid (VS) or vapour-solid-solid (VSS) mechanism. For some nanowires, such as GaAs nanowires, the VLS growth mechanism is apparent Ga droplet microscopically visible at the top of NWs. In contrast, it is challenging to judge either VLS, VS or VSS mode has been applied for InAs NWs growth. This is because droplet mediating NW growth is rarely visible on the top of the grown NWs. A brief overview of the VLS, and VS growth mechanisms are presented below.

### **2.2.1 The Vapor-Liquid-Solid (VLS) process**

Wagner and Ellis discovered the VLS mechanism in 1964 [18]. This mechanism, for example, for InAs nanowire growth, involves three main steps:

1. Choice of an appropriate metal catalyst for growth and the formation of small metal/In eutectic droplet at the eutectic temperature  $T_E$  on the substrate surface.
2. Passing of vapour-phase source species on the eutectic droplet at a temperature  $T \geq T_E$ .
3. Supersaturation of the vapour-phase source species at the liquid/solid (e.g., droplet/substrate) interface. Deposition of III-V solid material in the form of nanowires follow.

VLS process operates as long as liquid droplet exists [19]. As stated earlier, three phases of material; vapour phase V, intermediate liquid phase L and the final solid phase S participated in NW growth by the VLS mechanism. This growth mechanism can be ascertained by thermodynamic conditions, while the rate of growth process is

kinetically governed [20]. Both thermodynamic and kinetic growth processes depend on the growth conditions including, temperature, system pressure, and partial pressure of the precursor materials. These conditions can determine whether the growth is dominated by the thermodynamic or kinetic conditions. The crystal growth requires the fulfilment of Gibbs-Thomson effect for growth, including the existence of chemical potential difference between the supplied materials and the material intended to be grown (See Fig 2.2). It serves as the thermodynamic driving force for supersaturation and growth. It is given by

$$\Delta\mu_{VS} = \mu_V - \mu_S \quad (2.1)$$

Where  $\Delta\mu_{VS}$ , is the chemical potential difference between vapour and solid phases,  $\mu_V$  is the chemical potential of material in vapour phase and  $\mu_S$  is the chemical potential of material in solid phase. The chemical potential difference between the vapour phase and the solid phase should be positive to ensure supersaturation and solidification. For this, the chemical potential of the liquid phase, e.g.,  $\mu_L$  should be larger than that of the solid phase, e.g.,  $\mu_S$ , but smaller than that of the vapour phase, e.g.,  $\mu_V$ . It would drive the vapour-to-liquid-to-solid transition (eq. 2.2) [5].

$$\mu_V > \mu_L > \mu_S \quad \text{or} \quad \Delta\mu_{VS} > \mu_{LS} > 0 \quad (2.2)$$

If  $\Delta\mu_{VS}$  is zero, the system is at equilibrium and the growth will stop. If it is negative, the system is undersaturated and there is a thermodynamically driving force for desorption of material from the crystal into the supply.

Equation (2.2) is the conditions where the adsorption-induced VLS growth occurs. For group III-V nanowire growth, the chemical potential of each phase equal to the summation of the chemical potential for each group as stated in eq. 2.3.

$$\mu_V = \mu_3^V + \mu_5^V \quad (2.3)$$

If the condition in eq. 2.2 is satisfied NWs will grow via VLS process as follows. The metal nanoparticles are formed on substrate. Since the liquid droplet formed from it has sticking coefficient larger than that of the solid substrate; semiconductor precursors at the growth temperature T, prefer to deposit on the liquid droplet than on the substrate. By further supplying semiconductor precursors to the droplet, the droplet is supersaturated with the vapour-phase nanowire source species. Consequently, the incoming fluxes of the NW source species are precipitated at the droplet/substrate interface forming NWs. The diameter of the resultant NWs depends on the droplet size and the growth process depends on the supersaturation, which is affected by the precursor's concentration and substrate temperature [21]. VLS mechanism is shown in Fig (2.2).

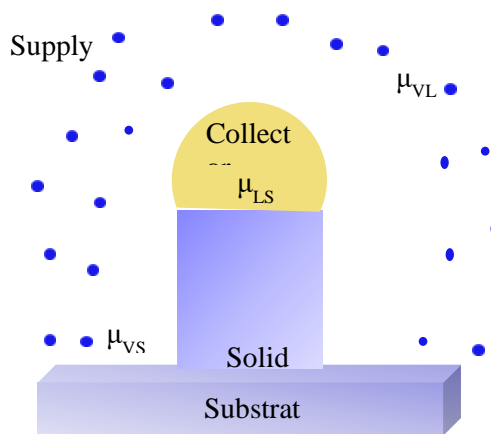


Figure 2.2: Schematic Illustration of the supersaturation relevant in a three-phase system modified from reference [7]

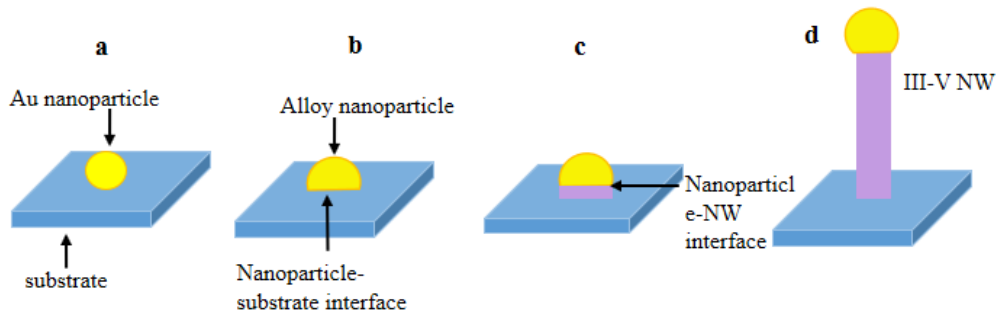


Figure 2.3: VLS mechanism for III-V NWs using foreign catalyst. Modified from Ref. [23]

## 2.2.1 The Vapor-Solid process

Vapour-solid mechanism operates when thermally evaporated semiconductor source species land on the substrate and are deposited on this surface in the form of nanowires. The semiconductor vapour temperature may be close to its melting point temperature. Preferential incorporation of reactants takes place at high-surface-energy sites leading to continuous growth of nanowires. It is argued that nanowire growth is driven by physio-chemical processes such as directed screw dislocation, planar defects (twin boundary and stacking fault), anisotropic surface energy of various facets, mediation of oxides, etc. As there is no metal catalyst involved in the growth, there are no droplets to act as favourable locations to collect the III-V precursors. VS process is not analogous to VLS process, as it involves no liquid intermediate phase.

## 2.3 Self-catalysed droplet epitaxy (DE) for InAs nanowires

In droplets MBE epitaxy, metal droplets are first formed. These droplets act as the collectors of materials from the incoming growth precursors. To be more specific, the supplied source elements act as seeds for crystallisation to initiate the NW growth

(growth details presented in chapter 5 section 5.2.2), group III materials on the substrate surface act as a collector to the top of the NWs when the shutter are opened for initiating of NWs growth. In this thesis, all InAs NWs were grown via As rich condition which assumes a VS mechanism. This means In flux play a crucial role in determining the NWs growth rate and the morphology of the resulting NWs [22].

## 2.4 Substrate orientation and NWs growth direction

InAs NWs are grown on Si (111) substrate. This crystallographic direction for growth is favoured because this crystallographic direction has lower surface energy that makes the atoms to precipitate on the substrate surface and cause the largest decrease in Gibbs free energy. The (111) growth direction also minimises the interfacial energy of the nanoparticle–nanowire interface. Therefore, NWs grown on Si (111) direction would grow up vertically on the substrate [23].

## 2.5 Carrier occupation and Fermi level

The probability of an electron to occupy a given energy state ( $E$ ) can be described by Fermi-Dirac distribution function:

$$F(E) = \frac{1}{1 + e^{(E - E_f)/kT}} \quad (2.4)$$

Where,  $F(E)$  is the probability that an energy state is occupied,  $E$  is the energy of the energy state,  $E_f$  is the Fermi level,  $k$  is the Boltzmann constant, and  $T$  is the absolute temperature in degree Kelvin [24]. For intrinsic semiconductor Fermi level is located approximately in the middle of the bandgap (Fig 2.4b). Doped semiconductors have different situation. In the case of n-type materials, large number of electrons occupies the conduction band shifting Fermi level  $E_f$  up close to or inside conduction band

(Fig2.4a). P-doping shifts the Fermi level down close to or inside the valence band. Consequently, large number of holes will exist in the bottom of valence band edge. If the semiconductor atoms are injected by both electrons and holes, electrons and holes, can occupy the conduction band and the valence band respectively at the same time. This leads to the separation of quasi Fermi levels of electrons  $E_{Fc}$  and holes  $E_{Fv}$  [25] .

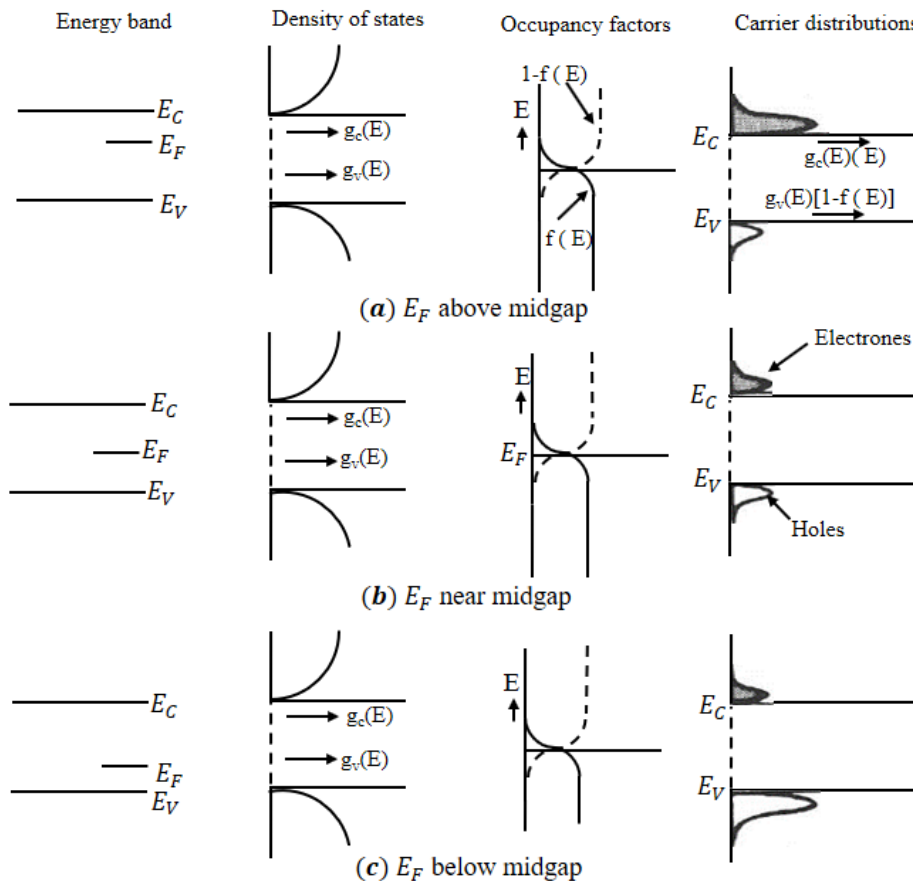


Figure 2.4: Carrier distributions of a) n-type semiconductor, b) intrinsic semiconductor, c) p-type semiconductor. Where  $g_c(E)$ ,  $g_v(E)$  are the density of states in the conduction band and valence band respectively.  $f(E)$  is the filled  $-$ state occupancy factor,  $[1-f(E)]$  is the empty  $-$ state occupancy factor modified from Ref [26]

## 2.6 Direct and indirect bandgap semiconductor

If a transition between conduction and valence band happens without the change of momentum. This transition is called the direct transition and the semiconductors are called direct bandgap semiconductors. A few examples of these semiconductors are GaAs, InAs and InP, see Fig (2.5a). In direct bandgap semiconductors, the transition of electrons from the

conduction band to the valence band can result in an emission of photons with energy equal to energy band gap  $E_g$ . Unlike indirect bandgap semiconductors (Fig (2.5b)) which have the conduction band minima and valence band maxima different locations (different momenta). For these semiconductors, electron transitions from the conduction band to the valence band at the bandgap energy must be accompanied by phonon emission or absorption in order to account for the change in momentum [26, 27].

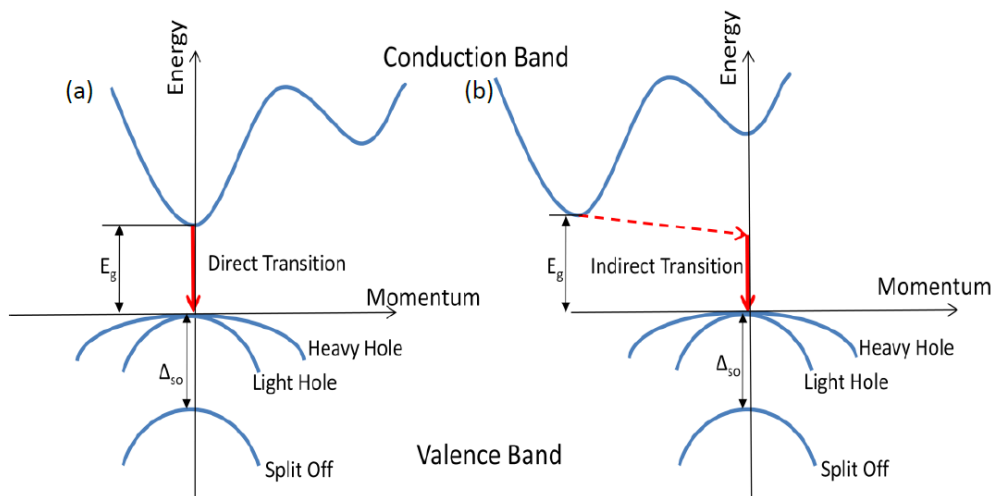


Figure. 2.5 the electron energy versus momentum plot at the bottom of conduction band and the top of valence band for case (a) direct semiconductors and case (b) indirect semiconductors.

## 2.7 Bandgap engineering:

If electrons from the conduction band and holes from the valence band recombine directly, a semiconductor emits light. The energy of the emitted radiation can be tailored by altering the bandgap of a material to produce a specific wavelength. This is known as bandgap engineering [28]. In nanocrystals, many parameters can be tuned so they can modulate their electronic bandgap, including size, shape, and composition of the bands. For binary compounds, the bandgap can be calculated using eq. (2.5).

$$E_g = xE_{\text{InSb}} + (1 - x)E_{\text{InAs}} - Cx(1 - x), \quad (2.5)$$

Where  $x$  is the Sb composition,  $E_{\text{InAs}}$  and  $E_{\text{InSb}}$  are the bandgaps for InAs and InSb respectively, and  $C$  is the bowing parameter. The bowing parameter is a factor included that accounts for the deviation of each ternary compound from a linear interpolation between the two binary compounds. For InAsSb the bowing parameter is within the range of 0.67– 0.69 eV and is thought to be temperature dependent [29].

## 2.8 Temperature dependence of the bandgap

The temperature dependence of the bandgap arises from increasing the lattice constant with increasing temperature. This increase in lattice spacing leads to reduction in the energy that required to exciting electron into the conduction band, which in turn leads to narrowing the bandgap of the material. This change in bandgap can be described using Varshni equation, which is given by follows:

$$E_g(T) = E_{g0} - \frac{\alpha T^2}{\beta + T} \quad (2.6)$$

Where,  $E_{g0}$  is the bandgap energy at 0 K,  $\alpha$  and  $\beta$  are empirical parameters.  $\alpha$  is 0.5meV/K and  $\beta$  is of the order of Debye temperature [28].

## 2.9 Energy band alignment

When two different semiconductors are joined to form a heterostructure, different types of band alignments result. The band alignment depends on the differences in electron affinities and band gaps of the two semiconductors. These heterostructures can be categorized into three types; type I, type II and type III heterostructures. The details of these heterostructures will be explained in next section.

## 2.9.1 Type I band alignment

In type I alignment of heterostructure, the conduction band  $E_c$  of narrower gap material (A) is lower than that of wider gap material (B) as shown in Fig 2.6. In this type of band alignment, both electrons and holes are confined in the narrower gap material. Examples of heterojunction that giving type I alignment are AlAs/GaAs, (AlAs, AlSb)/ GaSb, (AlSb,GaSb)/InSb and (GaAs,GaSb,InSb)/AlSb [30].

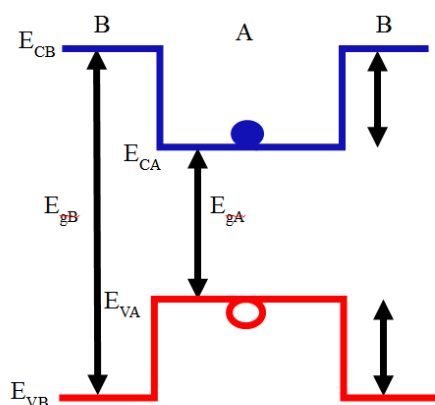


Figure 2.6: Illustration of type I band alignment

## 2.9.2 Type II Bandgap alignment

Type II band alignment confines one type of carriers in different materials. This leads to carriers' separation, which causes indirect radiative recombination. Depending on the nature of band-offset, type II alignment may be divided into two categories; type II-a and type II-b1. In type II-a, the electrons are confined in the narrow band gap material whilst the holes are confined in the wider gap material. This is evident from the following figure for type II-b (see Fig 2.7). Example of type II-a, (AlAs,GaAs,InAs)/AlSb. For type II-b, (AlSb, GaSb)/GaAs.

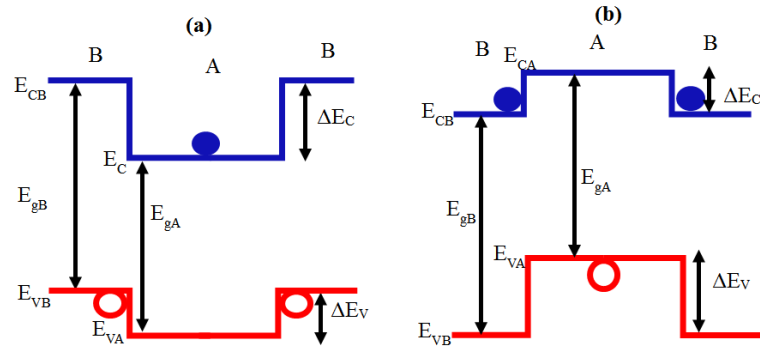


Figure 2.7 Energy band alignments for (a) type II-a and (b) type II-b. Diagram indicates the location of carriers and sign designation of the conduction and valence band offsets [12].

### 2.9.3 Type III bandgap alignment (broken gap)

In this type of band alignment, the conduction band of the narrow gap material is lower than the valence band of wider material. It produces type III-a band alignment such as InAs/GaSb and (InAs,GaSb)/InSb. In type III-b, the conduction band of wider gap semiconductor is lower than the valence band of the narrower gap material. A good example of it, is (InSb,GaSb)/InAs. , shown in Fig (2.8)

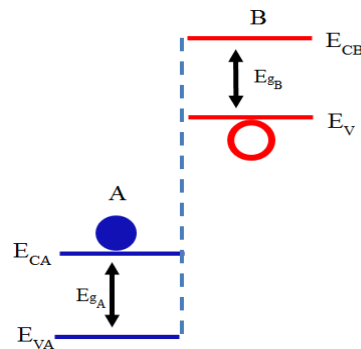


Figure 2.8: Type III energy band alignments

## 2.10 Recombination Mechanisms

When electron in the conduction band combines with holes in the valence band, they could emit a photon and/or phonon, depending on whether they recombine radiatively or non-radiatively. There are different types of radiative processes including band-to-band recombination (BtB), band to donor/acceptor recombination (BDA), donor to

acceptor recombination (DA) and exciton recombination. The non-radiative recombination includes Auger recombination, Shockley-Read-Hall Recombination and surface recombination.

### 2.10.1 Band-to-Band recombination

Band to band recombination occurs when an electron from the conduction band directly combines with a hole in the valence band and releases a photon (Fig 2.9a). The emitted photon has energy equal to the band gap and it is equal to the difference between energy of conduction band edge  $E_C$  and the valence band edge  $E_V$ . This process is dominant in direct gap semiconductor materials.

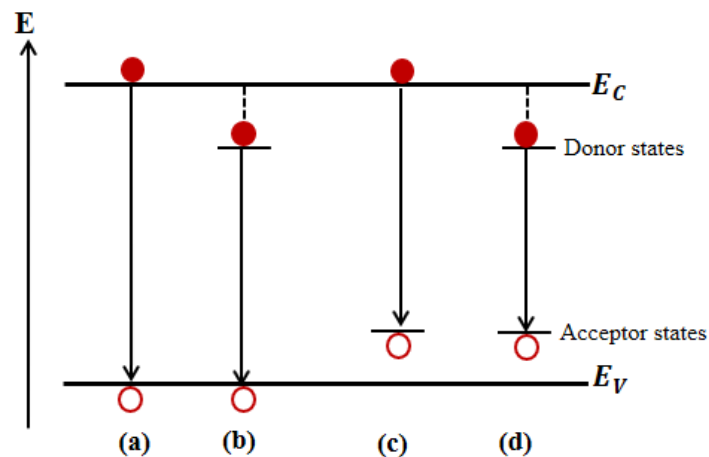


Figure 2.9: Radiative recombination mechanisms; (a) band-to-band recombination, (b) donor state to valence band recombination, (c) conduction band to acceptor state recombination, (d) donor to acceptor recombination. Solid circles represent electrons whilst hollow circles represent holes. Dashed lines correspond to phonon emission whilst solid lines represent photon emission.  $E_C$  and  $E_V$  are the energies of the conduction and valence bands respectively.

### 2.10.2 Free to bound recombination

Another radiative process, which occurs between electrons in the donors' state and holes on the valence band (Fig 2.9b) or between electrons in the conduction band and holes in the acceptor states (Fig 2.9c), due to transitions caused by defects in a semiconductor.

They occur at low temperatures as the donor/ acceptor level excite to conduction/valence band as temperature increases, favoring BtB emission. The resultant photon has a longer wavelength than the emission from band to band recombination.

### **2.10.3 Donor to acceptor pair recombination**

In the presence of sufficient impurities in both levels (hole level and electron level) of semiconductor, a radiative emission can result by the recombination between donor and acceptor states (Fig 2.9d). The donor-acceptor recombination can only be clearly seen at low temperatures.

### **2.10.4 Exciton recombination**

Electron – hole pair is observed in pure bulk materials at low temperature under conditions in which thermal energy is lower than the binding energy of the exciton. Another condition for exciton formation is low carrier concentration. Since the high carrier concentration, could screen the interaction between holes and electrons. There are two types of exciton; free exciton which produces photons with energy less than the bandgap and bound exciton which can be found near a defect or impurity sites.

## **2.11 Non-radiative recombination**

In some cases when electron and hole recombine (especially in narrow bandgap materials) there would be no photon could be emitted. Instead, a phonon can be produced causing non-radiative emission. This type of emission is undesirable. It degrades device performance. There three types of such an emission including; Auger

recombination, surface recombination, and Shockley-Read-Hall Recombination. Their details will be described in below.

### 2.2.1 Auger recombination

Auger recombination occurs when the recombination energy is supplied to a third charge carrier causing the latter to be excited to a higher energy level within the band. There are four types of Auger recombination, three of them involve two holes and one electron (ehh process) and are dominant in p-type materials. The fourth one occurs in the presence of two electrons and one hole (eeh process) and it is important in n-type materials. Auger recombination becomes severe for some special cases, for examples, at high temperature, at high doping concentration and in the materials with narrow band gap [31]. There are three types of Auger recombination illustrated in Fig (2.10).

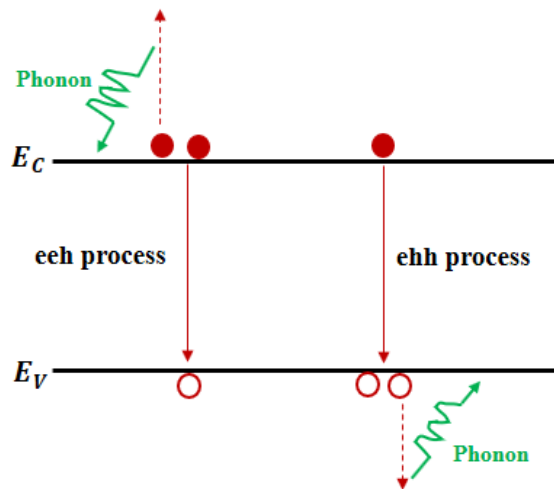


Figure 2.10: Auger recombination show both processes (eeh) and (ehh).

### 2.11.2 Surface recombination

Surface states can be defined as a number of localized energy states or generation-recombination centres that may be introduced at the surface region. Surface states are related to the dangling bonds that are formed in semiconductors due to the lack of

neighboring atoms. The dangling bonds trap impurities causing non-radiative emission. Surface state is common problem in nanowires due to large area to volume ratio. However, it can be suppressed by surface passivation [32].

### **2.11.3 Shockley-Read-Hall Recombination**

This type of recombination caused by native lattice defects in the crystal such as vacancies, impurities or dislocations in the crystals. They create deep level state within the energy gap leading to a transition either from the conduction band to a trap state or from a trap state to the valence band. Usually deep level transitions are non-radiative where the recombination occurs via a multi phonon process.

## **2.12 p-n junction**

PN junction is the basis for many devices such as diodes, transistors, LED, solar cells and photodetectors. PN junction is formed when p-type semiconductor has an interface with an n-type material. At the junction, there is a difference in carrier concentrations as these concentrations are different in the two adjacent regions. Therefore, electrons diffuse from n- type to p-type region leaving behind immobile positive ions, which create a layer of positive charge at the junction edge. Similarly, holes move across n region from p-type region causing a layer of immobile negative ions near the junction. The carriers' movement from n and p type creates current called diffusion current. The two layers of negative and positive ions form depletion region. The ions inside it try to combine with each other causing potential difference, which is called barrier potential or built-in potential. This potential acts as a barrier to the free electrons preventing them from any more diffusion unless they have energy enough to break this barrier potential. This energy can be supplied by applying an external electric field. Under appropriate

conditions, all these may occur naturally without applying any external electric field. As shown in Fig (2.11 a). When applying forward bias, the height of potential decreases, which promotes the diffusion of electrons across the junction. This bias leads to shrinkage in depletion region, leading to increase in current in the circuit as shown in Fig (2. 11b). Under reverse bias condition, the height of the potential barrier increases. Hence, electrons cannot jump to the p-side from the n -region instead causing expansion in depletion region and a low current.

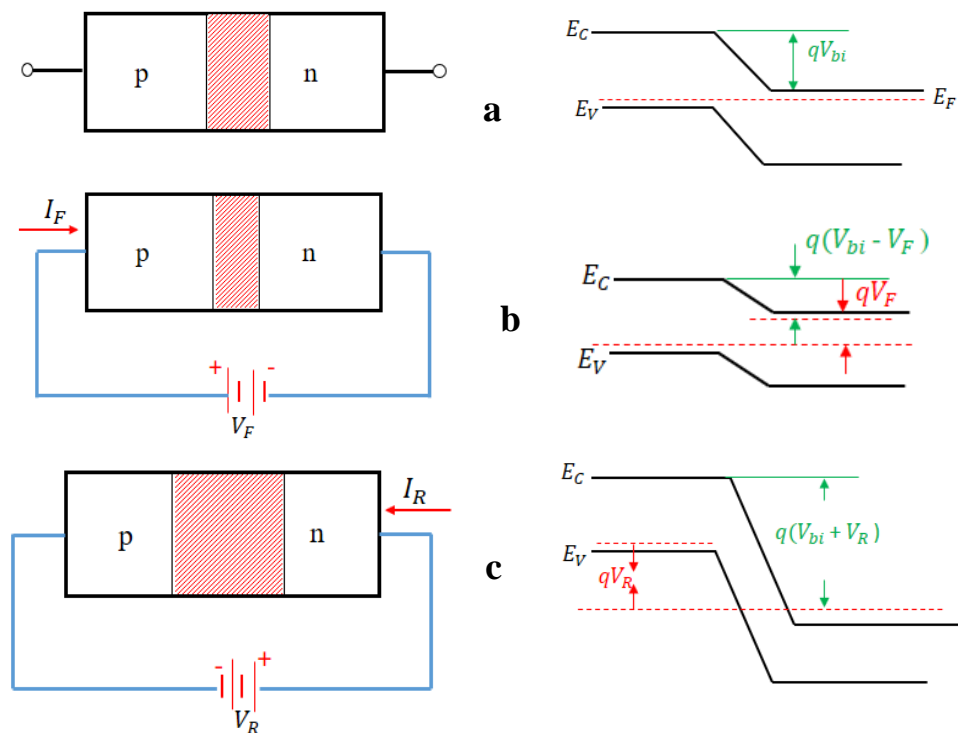


Figure 2.11: P-n junction in a) Thermal equilibrium. b) Forward bias. C) Reverse bias. Modified from Ref [14].

## 2.13 Photodetector and principle of operation

Photodetector is a device that convert incident optical signal into electric current. Photodetectors can be fabricated in many different ways. They can be p-n junction photodetectors, p-i-n diodes, metal-semiconductor diodes (or Schottky barriers) and heterojunction diodes. When photons strike the active region (depletion region) of the

device, the photogenerated e-h pairs. Because of strong electric field in the depletion region, it separates the generated e-h pairs. This occurs without applying any external electric field. By applying reverse bias, the photogenerated carriers are swept apart to the opposite terminal of the applied electric field (holes to the cathode and electrons to the anode). Consequently, these carriers will contribute to the photocurrent of the external circuit. The photodetector devices may be reversely biased to improve the response speed; the devices also have a small area to ensure a low junction capacitance. Several other types of photodetectors will be described in the next sections.

### **2.13.1 A p-i-n photodetector**

A p-i-n diode is a p-n junction with an extra-undoped layer sandwiched between p and n regions. The question that may be raised is; why i-layer is required?

In photodetector, it is important to have a thick active region so that it absorbs all the incident photons. To further widen the depletion region that acts as an active region of the photodetector, intrinsic layer (i) should be sandwiched between p and n side. Adding this layer will decrease the capacitance of the photodetector as shown in eq. (2.7):

$$C_j = \frac{A}{d} \quad (2.7)$$

Where  $C_j$  , is the junction capacitance, A is the area of depletion region and d is the distance between positive and negative charge in the depletion region. Reducing the capacitance leads to a high frequency response according to eq. (2.8). Consequently, the speed of the photodetector will increase. In addition, when capturing area of the light (which represents i-layer) becomes larger, the efficiency of the device becomes

higher due to better light absorption, which increases the responsivity of the photodetector increases. As shown in eq. (2.9) [33].

$$f = \frac{1}{2\pi RC} \quad (2.8)$$

Where  $f$  is the frequency,  $R$ , is the resistance and  $C$  is the capacitance.

### **2.13.2 Heterostructure photodetector**

Heterojunction device is formed by epitaxially depositing a semiconductor a large bandgap on a small bandgap semiconductor. The lattice mismatch between the two materials should be very small in order to obtain heterojunction without dislocations. The heterojunction can be fabricated in a way so that the material combinations can make the device parameters easily optimised. These device parameters include specific optical-signal wavelength quantum efficiency and response speed.

### **2.13.3 Metal-semiconductor photodiode:**

This kind of detectors is particularly useful in the ultraviolet and visible light regimes of the spectrum. It consists of semiconductor materials with thin layer of metal about (10 nm) coated with anti-reflection layer. In order to ensure that all or most of the incident radiation is absorbed by the semiconductor surface, it is important to choose an appropriate metal and the antireflection coating for specific wavelength. For example, Au-Si photodetector with 10 nm gold and 50 nm antireflection (zinc sulphide) coating, can transmit more than 95% of the incident light ( $\lambda=0.6328\mu\text{m}$ ) into the Si substrate.

## 2.14 Photodetector characterization parameters

When photodetector is designed there are main parameters of it should be measured to ensure that the device is working. These parameters are; Quantum efficiency ( $\eta$ ), responsivity(R), impulse response ( $t_r$ ) and noise equivalent power (NEP) or dark current. The details of each of these parameters are stated in the following.

### 2.14.1 Quantum efficiency EQE ( $\eta$ )

Quantum efficiency is the fractional number of incident photon flux, which generate e-h pairs contributing to the photocurrent [34].

$$\eta = \frac{I_p/q}{\varphi} \quad (2.9)$$

This is called external quantum efficiency EQE.

Where  $I_p$  ,is the photo current generated is the electron charge, $q$ , is the flux of incident photons which is given by:

$$\varphi = \frac{P_{opt}}{h\nu} \quad (2.10)$$

Where  $P_{opt}$ the incident optical power and  $h\nu$  is the photon energy. Making use of eq. (2.9) and (2.10), the quantum efficiency can be obtained as:

$$\eta = \frac{h\nu I_p}{qP_{opt}} \quad (2.11)$$

### 2.14.2 Internal quantum efficiency IQE ( $\eta_i$ )

Internal quantum efficiency is the ratio of generated e-h pairs, which contribute to the photocurrent per absorbed photon. This efficiency excludes the photons reflected from

or transmitted through the device. The EQE can be expressed in terms of IQE as follows [34]:

$$\eta = \eta_i(1 - R)(1 - e^{-\alpha d}) \quad (2.12)$$

Where  $\eta$  and  $\eta_i$  are the EQE and IQE respectively,  $R$  is the reflectance,  $\alpha$  is the absorption coefficient and  $d$  is the width of the absorption area (active region). It can be noticed according to (eq. 2.12) that the factors affecting the EQE are;  $\eta_i, R, \alpha$  and  $d$ . Therefore, to maximize the reflectivity should be zero and the absorption coefficient should be the highest for some specific wavelength and  $\eta_i$  should be 1.

### 2.14.3 Responsivity

The ratio of the electric power generated to the incident optical power gives the responsivity.

$$R_\lambda = \frac{I_p}{q} \quad (2.13)$$

By substituting eq. (2.11) into (2.13) responsivity will be given by

$$R_\lambda = \eta \cdot \frac{\lambda (\mu m)}{1.24} \quad (2.14)$$

It can be noticed that  $R$  depends on the quantum efficiency of the photodetector. Eq. (2.14) demonstrates that  $\eta$  must be increased to maximize  $R_\lambda$ .

### 2.14.4 Noise equivalent power (NEP)

It is the weakest detectable signal per square root bandwidth for a given detector. It is measured by  $W/\sqrt{HZ}$ . There are many factors cause the noise in detectors such as dark

current. Dark current is generated when the detector operates under electric field without light source, diffusion current due to Auger or radiative recombination in n or p- region, generation and recombination in depletion region and band-to-band current. Another source of noise is surface states, which trap the generated carriers causing non-radiative recombination.

## References

- [1] S. A. Dayeh, "Semiconductor nanowires for future electronics : growth, characterization, device fabrication, and integration," PhD thesis, University of California, San Diego., 2008.
- [2] P. Caroff, K. A. Dick, J. Johansson, M. E. Messing, K. Deppert, and L. Samuelson, "Controlled polytypic and twin- plane superlattices in III- V nanowires," *Nature Nanotechnology*, vol. 4, no. 1, pp. 50, 2008.
- [3] H. J. Joyce, J. Wong-Leung, Q. Gao, H. H. Tan, and C. Jagadish, "Phase perfection in zinc blende and wurtzite III- V nanowires using basic growth parameters," *Nano letters*, vol. 10, no. 3, pp. 908-915, 2010.
- [4] V. Dubrovskii, and N. Sibirev, "Growth thermodynamics of nanowires and its application to polytypism of zinc blende III-V nanowires," *Physical Review. B*, vol. 77, no. 3, pp. 035414-035422, 2008.
- [5] X. Duan, J. Wang, and C. M. Lieber, "Synthesis and optical properties of gallium arsenide nanowires," *Applied Physics Letters*, vol. 76, no. 9, pp. 1116-1118, 2000.
- [6] W. S. Shi, Y. F. Zheng, N. Wang, C. S. Lee, and S. T. Lee, "Oxide-assisted growth and optical characterization of gallium-arsenide nanowires," *Applied Physics Letters*, vol. 78, no. 21, pp. 3304-3306, 2001.
- [7] Morales, and Lieber, "A laser ablation method for the synthesis of crystalline semiconductor nanowires," *Science (New York, N.Y.)*, vol. 279, no. 5348, pp. 208, 1998.
- [8] D. P. Yu, Z. G. Bai, Y. Ding, Q. L. Hang, H. Z. Zhang, J. J. Wang, Y. H. Zou, W. Qian, G. C. Xiong, H. T. Zhou, and S. Q. Feng, "Nanoscale silicon wires synthesized using simple physical evaporation," *Applied Physics Letters*, vol. 72, no. 26, pp. 3458, 2004.
- [9] P. Yang, "The chemistry and physics of semiconductor nanowires," *MRS Bulletin*, vol. 30, no. 2, pp. 85-91, 2005.
- [10] Y. H. T. Y. F. Zhang, N. Wang, D. P. Yu, C. S. Lee, I. Bello, and S. T. Lee, "Silicon nanowires prepared by laser ablation at high temperature," *Applied Physics Letters*, vol. 72, no. 15, pp. 1835, 1998.
- [11] M. T. Björk, B. J. Ohlsson, T. Sass, A. I. Persson, C. Thelander, M. H. Magnusson, K. Deppert, L. R. Wallenberg, and L. Samuelson, "One-dimensional heterostructures in semiconductor nanowhiskers," *Applied Physics Letters*, vol. 80, no. 6, pp. 1058-1060, 2002.

- [12] M. Yazawa, M. Koguchi, A. Muto, and D. K. Hiruma, "Semiconductor nanowhiskers," *Advanced Materials*, vol. 5, no. 7-8, pp. 577-580, 1993.
- [13] K. A. Dick, K. Deppert, L. S. Karlsson, L. R. Wallenberg, L. Samuelson, and W. Seifert, "A New Understanding of Au-Assisted Growth of III–V Semiconductor Nanowires," *Advanced Functional Materials*, vol. 15, no. 10, pp. 1603-1610, 2005.
- [14] C. J. Novotny, and P. K. L. Yu, "Vertically aligned, catalyst-free InP nanowires grown by metalorganic chemical vapor deposition," *Applied Physics Letters*, vol. 87, no. 20, pp. 203111, 2005.
- [15] Z. H. Wu, X. Y. Mei, D. Kim, M. Blumin, and H. E. Ruda, "Growth of Au-catalyzed ordered GaAs nanowire arrays by molecular-beam epitaxy," *Applied Physics Letters*, vol. 81, no. 27, pp. 5177-5179, 2002.
- [16] Y. F. Chan, X. F. Duan, S. K. Chan, I. K. Sou, X. X. Zhang, and N. Wang, "ZnSe nanowires epitaxially grown on GaP(111) substrates by molecular-beam epitaxy," *Applied Physics Letters*, vol. 83, no. 13, pp. 2665-2667, 2003.
- [17] L. Schubert, P. Werner, N. D. Zakharov, G. Gerth, F. M. Kolb, L. Long, U. Gösele, and T. Y. Tan, "Silicon nanowhiskers grown on  $\langle 111 \rangle$  Si substrates by molecular-beam epitaxy," *Applied Physics Letters*, vol. 84, no. 24, pp. 4968-4970, 2004.
- [18] R. S. W. a. W. C. Ellis, "Vapor-Liquid-Solid mechanism of single crystal growth," *Applied Physics Letters*, vol. 4, no. 5, pp. 89, 1964.
- [19] A. Fontcuberta i Morral, S. A. Dayeg, and C. Jagadish, *Semiconductor nanowires. I, Growth and theory*, 2015.
- [20] K. A. Dick, "A review of nanowire growth promoted by alloys and non-alloying elements with emphasis on Au-assisted III–V nanowires," *Progress in Crystal Growth and Characterization of Materials*, vol. 54, no. 3, pp. 138-173, 2008.
- [21] H. J. Fan, P. Werner, and M. Zacharias, "Semiconductor Nanowires: From Self-Organization to Patterned Growth," vol. 2, no. 6, pp. 700-717, 2006.
- [22] E. Dimakis, J. Lähnemann, U. Jahn, S. Breuer, M. Hilse, L. Geelhaar, and H. Riechert, "Self- assisted nucleation and vapor- solid growth of InAs nanowires on bare Si( 111)," *Crystal Growth and Design*, vol. 11, no. 9, pp. 4001-4008, 2011.
- [23] H. J. Joyce, "Growth and Characterisation of III-V Semiconductor Nanowires for optoelectronic device applications," Australian National University, 2009.

- [24] R. F. Pierret, *Semiconductor fundamentals*, 2nd ed. ed., Reading, Mass.: Reading, Mass. , Addison-Wesley Pub. Co., 1988.
- [25] A. Y. a. P. Yeh, *Photonics: optical electronics in morden communications*, 6th ed., Oxford University Press, 2007.
- [26] G. Ghione, *Semiconductor devices for high-speed optoelectronics*, Cambridge ; New York: Cambridge University Press, 2009.
- [27] M. Fukuda, *Optical semiconductor devices*, John Wiley & Sons, 1999.
- [28] K. O'shea, "A study of GaInNAsSb/GaAs quantum wells for use in telecommunications applications," Lancaster university, 2015.
- [29] I. Vurgaftman, J. R. Meyer, and L. R. Ram-Mohan, "Band parameters for III–V compound semiconductors and their alloys," *Journal of Applied Physics*, vol. 89, no. 11, pp. 5815-5875, 2001.
- [30] M. E. Pistol, and C. E. Pryor, "Band structure of segmented semiconductor nanowires," *Physical Review B*, vol. 80, no. 3, pp. 035316, 2009.
- [31] K. F. Brennan, *The physics of semiconductors:with applications to optoelectronic devices*, Cambridge University Press, 1999.
- [32] S. M. Sze, *Semiconductor devices: physics and technology*, John Wiley & Sons, 2008.
- [33] C. Kittel, P. McEuen, and P. McEuen, *Introduction to solid state physics*, Wiley New York, 1996.
- [34] R. LaPierre, M. Robson, K. Azizur-Rahman, and P. Kuyanov, "A review of III–V nanowire infrared photodetectors and sensors," *Journal of Physics D: Applied Physics*, vol. 50, no. 12, pp. 123001, 2017.

# Chapter 3

## Literature Review

This chapter presents an overview of infrared photodetectors operating in the spectral range of 2-12 $\mu\text{m}$ . The second part reviews the published papers of photodetector of bulk InAsSb and NWs. The third section reviews the published work of InAs and InAsSb NWs. Core-shell NWs reviewed in the last sections.

### 3.1 History of IR photodetector:

Infra-red photodetectors range from short wave infrared (SWIR) 1-2.5  $\mu\text{m}$  to long wave (LWIR) 8-12  $\mu\text{m}$  are of a particular interest. There are two groups of materials used in IR technology: firstly, II-VI, compound which was used during the last four decades specifically HgCdTe. The second are compound materials, in particular III-V (e.g, InGaAs, InAs and InSb). For applications that require an operation in the LWIR band as well as two-colour MWIR/LWIR bands, HgCdTe will most probably not be the optimal solution. There are many challenges in using HgCdTe material in photodiode application, some of them are the difficulties in growing due to solidus–liquidus separation (leading to marked segregation between CdTe and HgTe) and the high vapour pressure of Hg [1], toxicity, high growth and processing cost and surface instability [2].

For these reasons alternative technologies over the past 40 years were developed. One of these technologies is InAs/Ga<sub>1-x</sub>In<sub>x</sub>Sb superlattices (SLs) which have been also employed for IR detector applications in the 8–14 $\mu\text{m}$  region. In 1987, D. L. Smith & C. Mailhot [1], presented type II superlattice photodetectors made of InAs-Ga<sub>x</sub>In<sub>x</sub>Sb ~ x -0.4 on GaSb substrate. This structure provided small band gaps (by adding indium to

GaSb layers which created thinner layers combination) with improved optical absorption. The absorption coefficient was  $2000\text{cm}^{-1}$ . Another method to obtain a small band gap was proposed in 1995 by E. R. Heller et al. & F. Szmulowicz et al., using strain balanced superlattices. This study implied that the layer width of InAs ( $L_{\text{InAs}}$ ) and GaSb ( $L_{\text{GaSb}}$ ) did not need to be equal to the maximum absorption coefficients for a given cut off wavelength when obtained from a structure with  $L_{\text{InAs}} \neq L_{\text{GaSb}}$  [3]. It was found that the superlattice had advantages over bulk HgCdTe; including high responsivity, lower leakage currents, and greater uniformity [3, 4]. Type II band alignment and internal strain reduces the conduction band minimum of InAs and increases the heavy hole concentration in GaInSb. This lead to optical absorption comparable to that of HgCdTe.

The main challenge in SLs technology is in the growth and fabrication of photodiodes. It is difficult to grow thick SLs structures without degrading material quality since good quality thick SLs can provide high quantum efficiency[2]. Another serious problem in superlattice technology is surface passivation. Surface leakage is caused by the discontinuity in the periodic crystal structure which is caused by mesa delineation.

Quantum well infrared photodetectors were well established as technology and commercially available in focal plane array (FPAs). QWIPs have many advantages in LWIR photon-rich systems such as, gas sensors, medical imaging and surveillance applications [5]. Among the different types of quantum well IR photodetector (QWIPs) technologies, GaAs/AlGaAs, multiple quantum well detectors is the most mature [6] and has developed very quickly in the last decade. A. Fiore et al. presented strained InGaAs/AlGaAs multi-quantum well midinfrared photodetector at  $4.5\ \mu\text{m}$ . The device showed a low dark current of a few pA and a responsivity of  $12\text{mA/W}$  at temperature up to 95 K [7].s In 1998, D. H. Zhang and W. Shi [8] found the same results by using

compressively strained InGaAs/ AlGaAs QWIP with deferent Be doping concentration in the wells in a detector. The cut off wavelength was 7.9  $\mu\text{m}$  for a doping density of  $10^{18} \text{ cm}^{-3}$  and 7.25  $\mu\text{m}$  for  $2 \times 10^{17} \text{ cm}^{-3}$ . It was found that the responsivity at positive biases had much higher values than that at a negative bias, and that they are even higher than that of the sample with lower Be doping in the wells. The asymmetry of the responsivity is attributed to the inhomogeneity of the well-barrier junctions in the sample while the greater responsivity values at positive biases are due to the enhanced carrier population from higher doping.

Despite their advantages, there are many issues with QWIPs, e.g., low quantum efficiency, high dark current, and lack of normal incidence absorption. Quantum dot Infrared photodetectors (QDIPs) were used as similar technology to QWIPs and were supposed to solve some issues that were found in QWIPs. Some of the advantages of QDIPs over QWIPs are their ability to absorb the normally incident light due to three-dimensional confinement because of reduced dependence of the QDs' density of states, their operation is temperature insensitive, and finally having a long carrier life time, 10-100 times longer than QWIPs creating a low dark current. Intensive research was devoted to improving QDIPs performance, including lowering the dark current and increasing the operation temperature and [9-11]enhancing carrier lifetime [10] [12-16]. Further reduction in dark current was gained by using AlGaAs layers as current blocking layers [17]. Due to zero-dimensional quantum confinement [5, 17] , QD IPs have issues related to quantum dot (QD) formation, such as variability in size and shape of the dots, control of strain and material composition, and influence of wetting layers [18]. Therefore, III-V nanowires have been applied in photodetectors to overcome the limitations of existing detectors. One of the big issues that can be avoided using nanowires is that of lattice-mismatch since nanowires can be grown with a high

mismatch of 11% by growing InAs NWs on Si substrate. Another advantage of using NWs is, enhancing light absorption. NWs can act as effective waveguides that are able to concentrate and absorb light over micron lengths [19-30]. Interaction between NWs and incident electromagnetic waves occur through three optical phenomena; radial mode resonance or leaky mode, Fabry-Perot (F-P) or longitudinal modes and near field evanescent wave coupling [31]. The first mode results when the incident light couple strongly with NWs at a specific wavelength. Radial mode is called leaky mode because their field amplitude attenuate along the axis of NWs [32]. F-P mode gives rise to localised peaks in the electric field amplitude along the NW axis. Due to the longitudinal finite boundaries of NWs (NWs tip and base), this mode result in longitudinal standing waves along the NW length through constructive interference of the guided wave. Final mode (near-field mode) occurs due to the wave coupling between neighboring NWs. If the evanescent waves of enamoured NWs overlap and the latter enhances the same leaky mode then power can transfer to the neighboring NW. Consequently, the field amplitude of the leaky mode in the original NW decreases while that of the neighboring one increases. This process result in near-field or amplitude coupling. These three phenomena are affected by the geometry of NWs and the number of the NW arrays. It was shown that NW arrays with larger diameter absorb more efficiently than that of smaller diameter NWs [27]. In addition, the absorptance becomes unity at short wavelengths and decreases at longer wavelength. As the diameter increases the region of high absorptance shifts towards higher wavelengths [33]. It was demonstrated that absorption in semiconductor NW arrays occur by first phenomena mentioned above (optical resonance modes). Similarly, this mode was observed in single NWs [28, 34, 35]. From all above, it can be concluded that NW act as a waveguide that concentrate and absorb light effectively in a very small material volume. In particular, the  $HE_{1n}$

modes showed strong absorptance greater than that of thin film of equivalent thickness. This makes NWs significant beneficial for more efficient photodetection. Photodetection in NWs is sensitive to the polarization of the incident radiation. The photocurrent depends on the the angle between the long axis of NW and the polarization of incident light. For ZnO NWs it was shown when the incident light is parallel to the NW axis the photocurrent reaches its maximum value but it reduced to minimum value in other directions of incident light [36]. Same behaviour has been noticed for InP NWs [37] and GaN NWs [38]. In 2009, Wei-Wei et al reported an InAs NW photodiode with a very low reverse dark current  $\sim 10^{-8}$  A. The device contained n-InAs NWs grown on p-Si (111) substrate by MOCVD. The device operated at room temperature, and its photocurrent at reverse bias was 1000 times higher than the dark current even at low incident power of  $2.86\text{mW/cm}^2$ . This means that the photodiode has a strong photoresponse to white light [39] indicating potential applications as a broad band photovoltaic cell or a visible-infrared dual-band photodetector.

### **3.2 InAsSb NWs photodetector**

Bulk InAsSb heterostructure photodetector emerged in 2000 by HH. Gao et al [40]. They grew  $\text{InAs}_{0.89}\text{Sb}_{0.11}$  heterojunctions on InAs substrate by liquid phase epitaxy (LPE). InAsSb buffer layer was also used and doped InAsSbP cladding layers. The latter provide carrier confinement and prevent the losing of electrons to InAs. At room temperature the responsivity of this structure was  $0.8\text{ A/W}$  and detectivity  $1.26 \times 10^9\text{ cm}\cdot\text{Hz}^{1/2}\cdot\text{W}^{-1}$  at  $4.6\text{ }\mu\text{m}$  wavelength.  $\text{InAs}_{0.89}\text{Sb}_{0.11}$  is not lattice match with InAs. In order to create lattice match structure, an InAsSb buffer layer with Sb composition of 6% is required. Buffer layer with Sb=6% will limit the strain and reduce the non-radiative recombination caused by Shockley-Read which in turn causes low quantum efficiency. A. Rakovska et al [41] grew lattice-matched structure of p-i-n  $\text{InAs}_{0.91}\text{Sb}_{0.09}$

to GaSb substrate by MBE. The photodetector operated at 3.39  $\mu\text{m}$  wavelength and 250K. P-AlGaSb barrier was used for confining electron and InAlAsSb was used as barrier for holes confining. Nevertheless, it failed to confine holes causing noise due to the diffusion currents.

In 2013, InAsSb NW photodetectors were demonstrated for first time by Johannes Svensson et al. InAsSb NWs were grown on InAs (111) B substrate with varying Sb compositions ( $x$ ) of 0.04-0.76 by MOVPE. This work proved that the spectral photocurrent was strongly dependent on the wire diameter. At a specific wavelength, the absorption was enhanced by more than one order of magnitude as compared to a thin planar film with the same  $x$  by adjusting the diameter of the nanowires. The NWs diameter was controlled by varying the effective ratio of V/III near the NWs. As increasing the latter factor lead to minimizing the density of NWs, consequently, it amplified the radial growth [42].

Zhe Liu et al. demonstrated InAs NW photodetectors with very high photoresponse and detectivity in the wide UV visible to infrared region (300 - 1100nm). Time dependent measurements at different wavelengths and under various light intensities illustrated a fast, reversible, and stable photoresponse of the device. InAs NWs which were grown by CVD [43] produced device detectivity as high as  $2.6 \times 10^{11} \text{J}$ . Mio et al [44] reported field effect transistor (FET) InAs NWs used for near infrared photodetection. The NWs were grown on GaAs (111) B substrates by MBE. The top gate was half wrapped with 10nm  $\text{HfO}_2$  to act as top gate dielectric. The device operated at room temperature. The work investigated the effect of passivation on the photoresponse. It was found that the photoresponsivity of Schottky-ohmic contacted photodetectors was  $5.3 \times 10^3 \text{ A/W}$ , which is  $\sim 300\%$  larger than that of an ohmic-ohmic contacted device  $\sim 1.9 \times 10^3 \text{ A/W}$ .

InAs NW phototransistors have showed high performance due to trapping mechanism of the self-assembled, near surface photogating layer (PGL), which causes a strong photogating effect on the NW channel. This PGL is free from the impact of external environment. The device had a high photoconducting gain of  $10^5$  and a fast response time of 12 ms at room temperature. However, Yuxiang Han reported [45] that, for InAs NW photodetectors its negative photoconductivity is sensitive to the environmental atmosphere, and is strongly dependent on wavelength and intensity of the incident light. It has been noticed that the current decreases under light illumination and the amount of the current drop increases by improving light intensity. The highest current decrease was obtained under the largest light intensity, which was  $9.37 \times 10^3 \text{ mW/cm}^2$ . The NWs were grown by MBE and they were characterized to be single crystal ZB or WZ. The linear relationship between  $I_{ds}$  and  $V_{ds}$  confirms that the contact is ohmic. The largest photocurrent was observed to be  $-1.97 \mu\text{A}$  at  $V_{ds}$  of 0.3V and  $V_{gs}=20 \text{ V}$ , and its value was about 96% of the dark current under the same conditions. The same group reported photodetectors which had both (NPC) and (PPC) using the same individual InAs NWs grown by MOCVD and covered with native oxide layer.

InAsSb NWs were applied in MIR photodetectors. Svensson et al [42] used InAs/InAsSb heterostructure NWs grown on InAs (111) B substrate. Their research demonstrated that the NWs diameter has a strong impact on the spectral photocurrent and its dependence on Sb composition. For thin NWs, (269-661nm) spectral response ( $x=0.27$ ) does not completely depend on composition with only a slight expansion in wavelength with increasing  $x$ . Raising the NWs diameter beyond 500nm revealed a peak in the spectral photocurrent. It was found that the highest 20% cut off wavelength of 5.7  $\mu\text{m}$  is obtained for a device with wires with 0.62 Sb and with a diameter of 717 nm. More recently, Thompson et al. [46] obtained a short wavelength at 20% cut-off of

2.3 $\mu\text{m}$  and with low leakage in the current density of 2 mA/cm<sup>2</sup> from p-i-n InAsSb NWs array photodetector. This photodetector was fabricated for shortwave infrared detection. However, NWs devices suffer from surface states due to high volume to surface ratio and challenging in growth and controlling morphology and geometry. This motivated the need of passivating NWs with a shell of a wider band gap. A typical method is to use core-shell NW geometry.

### **3.3 InAs and InAsSb nanowires**

InAs has attracted attention in the last few decades. Its outstanding properties include a small electron effective mass, a direct and narrow bandgap (0.35 eV.) and high electron mobility (around 30000 cm<sup>2</sup>/V. S at 300K). These make it a promising candidate for electronic and optoelectronic applications such as mid-infrared photodetection and high-speed electronics. Due to its small effective mass, InAs has large Bohr Bulk radius ( $a_B$ ) of 34nm [47] compared to III-V materials. This feature makes InAs important in quantum confinement studies. Adding Sb to form ternary alloy InAs<sub>1-x</sub>Sb<sub>x</sub>, further improve InAs properties and results in new exceptional features. The most important improvement is that the bandgap can be engineered to be anywhere between 0.35eV-1.42eV. Therefore, InAsSb materials have attracted a considerable amount of attention in the past few years in the fabrication of silicon-based infrared optoelectronics, in particular to make highly efficient, room-temperature photodetectors on silicon substrates. These photodetectors have various important applications operating in mid-wavelength infrared (MWIR, i.e. 3–5  $\mu\text{m}$ ) and in long-wavelength infrared (LWIR, i.e. 8–12  $\mu\text{m}$ ) making them good alternatives to HgCdTe based infrared LWIR detectors. InAsSb alloys possess unique properties such as their direct and wide bandgap energy, high thermal conductivity, small electron effective mass, long lifetime, and electron

mobility. Their unique 1D architecture, in particular, has advantages in device applications such as enhanced light absorption, long carrier diffusion length, improved carrier collection efficiency, and a great degree of freedom in combining materials with different lattice parameters and doping profiles. These features make InAsSb NWs an ideal and versatile candidate for a variety of device applications such as optoelectronics in the infrared [42, 46].

Au catalyst growth of InAs NWs has been the most widely used during few last decades. InAs NWs grown by chemical beam epitaxy (CBE) were reported by Jensen et al in 2004 [48]. InAs NWs were grown using Au particles positioned on InAs (111) B substrate by electron beam lithography (EBL). The study was able to determine the diffusion length of In species, which was found to be 10  $\mu\text{m}$  on the InAs NW (110) side surfaces. The effect of NWs diameter on the growth rate was studied and it was found that the growth rate decreases with increasing NWs diameter.

A. Dick investigated InAs grown by Au-assisted MOVPE [49]. They studied the dependence of morphology and growth rate on different growth parameters. These parameters included particle density and size, substrate material, In and As precursor flows and growth temperature. It was found that the growth rate decreases when the NW diameter is increased. Au-assisted molecular beam epitaxy (MBE) of InAs NWs was also investigated. The effect of substrate temperature on NW growth and morphology was discussed. It was found that NWs can only grow in a relatively narrow temperature window of 380-430  $^{\circ}\text{C}$ .

InAs/InAsSb axial nanowires were reported by Borg et al [50], where the NWs were grown by MOVPE with different Sb concentration ( $x=0.08-0.77$ ). They found that the incorporation of Sb into the nanowires is significantly higher than that of an epilayer under the same growth conditions. The same structure was grown by Ercolani et al [51]

using a gold catalyst on InAs (111) substrate by CBE. There was a significant increase in the diameter of the InAsSb segment which correlated to the nucleation and step-flow on the lateral facets. Meanwhile M.Pea [52] demonstrated that lateral growth can be suppressed by increasing the growth temperature of InAsSb and reducing the length of InAs segment. This suppression can be explained as a result of the re-evaporation of material from the InAsSb sidewalls. They boosted the growth temperature which increased the diffusion length. In 2014, Sourribes [53] reported the growth of catalyst free InAsSb nanowires by MBE with  $0 \leq x \leq 0.15$ . The report demonstrated that the effect of Sb composition on the defects density was a sharp drop in the density of the stacking fault when the Sb content was increased. This drop led to an increase in the field effect mobility which became more than 3 times greater at room temperature for Sb, equal to 0.15. In 2014, Na Du et al [54] presented self-catalyst MOVPE InAsSb NWs with x range from 0-0.43. They demonstrated that Sb composition has a significant effect on the morphology and the crystal quality of the NWs. In addition, it was found that there was an opposite trend of axial and radial growth rate change resulting from increasing the group V flow rate ratio. In 2015, the same researchers [55] obtained InAsSb NWs under different growth parameters, including the V/III ratio, temperature and Sb flow rate fraction FRF. Two types of growth mechanism may be dominant depending on the growth parameters. The NWs grow via VLS at low V/III ratio and relatively high Sb FRF where NWs grow with pure crystal phase. High V/III ratio & low Sb-FRF make VS mode dominant, in which NWs exhibit unified growth direction and uniform composition distribution. In 2016, the same group of researchers [56] grew planar InAsSb NWs by MOCVD growth technique on differently oriented Si substrate, i.e, (-100), (110) and (-1-1-1). Under the same growth conditions, NWs were grown in-plane on all of the substrates. NWs grew laterally along different directions and were

distributed evenly in each direction over a large area. For the Si (-100) substrate, the NWs grew along four cross directions while for the other two angles NWs grew along six specific plane isomorphic positions. For Si (-1-1-1) the angles between each direction were  $60^\circ$  but for Si (110), the angles between each two directions were  $54.7^\circ$  or  $70.5^\circ$ . Zhang & Anybe grew InAsSb on Si (111) substrate [57] and graphite [58]. The crystal structure of NWs was controlled by tuning the Sb composition from % -1%. A small amount of Sb led to quasi-pure WZ while its further increase led to quasi-pure ZB. Farrell et al [59] reported self-catalyst InAsSb NWs grown by self-catalysed selective area MOCVD.

## **3.5 Core-shell NWs**

### **3.5.1. InAs/GaSb core-shell nanowires:**

InAs/GaSb heterojunction has the most exotic line-up since it exhibits a type III broken gap alignment. At the interface, the bottom of conduction band of InAs lines up below the bottom of the valence band of GaSb, with a break in the gap of about 150 meV [60]. This results in the movement of electrons from GaSb valence band to InAs conduction band while free holes will appear in GaSb region. Therefore, InAs/GaSb bandgap alignment has a metallic structure and the existence of current in such wires will be due to both electron and holes [61]. For all above features, InAs/GaSb has been applied to several interesting devices. For instance, infrared optoelectronics, tunnel field effect transistors (TFETs) and tunnel diodes [62]. There is also a great interest in exploring the fundamental physics in such unique nano-heterostructures such as quantum transport, electron-hole interaction, and topological insulating behaviour in NW geometry [63].

In 1997, InAs/GaSb was firstly applied in MQW diode lasers with an active region consisting of thin InAs layers inserted into a GaSb matrix. The structures were grown on (100) n-GaSb substrates by MBE. The laser has very low threshold current and works at room temperature. These enhanced properties of the laser were due to the hole attracted by electrons that were localized in the InAs QW. This process results in quantization of hole states in barrier layer near the interfaces [64]. The first single NWs device has been presented in 2007 by A. Deyh et al [65]. InAs/GaSb axial NWs were grown by MOVPE on InAs(111)B substrate. The NWs were mechanically transferred to a Si/SiO<sub>2</sub> wafer in order to fabricate inverter device. The device exhibited excellent performance operating at 0.5 V., which is an essential requirement for low power electronics. Tunnel field-effect transistor of InAs/GaSb heterostructure NWs were presented by B.Borg et al. [66] in 2010. NWs were grown by MOVPE on InAs (111) B substrate with a thin barrier GaInAs inserts. Field effect transistors were fabricated from this structure. Three terminal transistors showed normal p-n diode properties at zero or positive  $V_G$ . While at a low bias of  $V_G = -0.5$ , it exhibited a linear current dependence indicating band-to-band tunnelling. The study revealed that it is possible to improve the on-state performance of the device by increasing the hole concentration in the GaSb segment which was not intentionally doped in this study. Another advantage of InAs/GaSb heterostructure is to allow tunnelling in the device at lower bias and gate-voltage while to decrease the resistance of the tunnel junction at the same time. GaSb/InAsSb core-shell NWs were grown by the same group [67], by MOVPE on GaAs (111) B. This work investigated three types of samples. Sample A is bare GaSb NW. Samples B-F had shorter growth time (0.5, 1, 2, 4 and 8 mins, respectively) and InAs shell around GaSb core. The study investigated the electrical properties of the NWs with changing GaSb shell thickness from 15nm down to less than 3nm. NWs with

the thickest shells exhibited typical electric characteristics of n-type semiconductors, indicating the contribution of shell transport features. Ambipolar behaviour was observed in the samples with intermediate thicknesses (5-7nm). Thinnest shells showed p-type semiconductor characteristics [68]. The Same group studied temperature dependent electrical properties of GaSb/InAsSb core-shell NWFET [69]. Four probes set up were applied in order to distinguish between the extrinsic (contact-related) and intrinsic (NW-related). Temperature dependent conductance measurements showed acceleration in the mobility of core-shell NWs by lowering the temperature from 295 to 4.2K opposite to bare GaSb NWs. InAs shell also improved the on-state which was found to be four times higher than bare wires when temperature is reduced from RT down to 4K. L.Namazi et al. [62] investigated the selective growth of GaSb shell on chosen surface of InAs core. In this study, the radial growth has been intentionally suppressed on the WZ surfaces of the core, while enhancing it on the ZB structures because of their high surface energy comparing to WZ structure. In addition, it investigated the dependence of shell morphology and thickness on the growth conditions, i.e.; growth time, temperature, V/III ratio, and total precursor flow rate. The results showed that the radial growth of the shell on ZB segment is independent of the growth temperature as its growth on WZ segment dropped by increasing T. The opposite situation occurs with the V/III effect as GaSb growth on the ZB drops by augmenting the composition ratio, while no considerable growth has been observed on the WZ section. MBE growth of InAs/GaSb core-shell NW was firstly reported in 2014 by T.Rieger et al. [70] on InAs (111)B. The report investigated the effect of the shell growth temperature on the NWs morphology. It has been found that low shell growth temperature (360°C) results in uniform diameter and smooth facets. Lowering the Tg less than 360 °C leads to a roughness of the shell. NWs tapering were observed while

growth temperature is higher than 490 C°. InAs/GaSb core-shells has been grown by CBE on Si (111) by M.Rocci et al [71]. The NWs were 2µm long with 60 nm diameter and a shell thickness of 30 nm.

### **3.5.2. InAs/AlSb core-shell NWs**

No published work has been reported yet about InAs/AlSb core-shell NWs. However, there are many reports of InAs/AlSb heterostructures and quantum well. S. Koester et al. [72] fabricated the split-gate ballistic constrictions on InAs/AlSb QW. The QWs were grown by MBE on GaAs (100) substrate [73]. The quantized conductance is observed in InAs/AlSb ballistic with a channel length of 1µm. The device showed improved performance and had a negligible parasitic gate leakage. The same group of research demonstrated a high-speed InAs/AlSb based heterostructure field effect transistor, which exhibited greatly improved charge control properties and enhanced high-frequency performance [74]. B. Brar and H. Kroemer [75] modified HSFET to incorporate an epitaxial P-type GaSb back gate. This p-type layer allowed collecting and removing the impact-generated hole escaping into the substrate. J.P Heida et al. [76], M.J Yangk et al [77], developed a nanofabrication scheme for electrons in InAs QWs. The work employed a p-type cap layer to create an insulating sample. The success of the structure is attributed to its ability to alter  $E_f^S$  which results in creating a conduction channel ~40nm beneath the etched surface. In this scheme the electron mean free path is expected to be insensitive to the wire width and the material quality will not be degraded by the additional lateral confinement. V.Aleshkin et al. [78] examined the samples fabricated from nominally undoped InAs/AlSb heterostructures grown by MBE on semi-insulating GaAs (001) with a metamorphic GaSb buffer layer. They investigated the dependence of effective G factor on the QW width. G.Moschetti et al. [79] studied the anisotropic transport behavior of InAs/AlSb heterostructures grown on

InP(001) substrate. Hall measurements demonstrated an enhanced anisotropy in  $\mu_n$  when cooled from room temperature to 2K.

## References

- [1] A. Rogalski, "HgCdTe infrared detector material: history, status and outlook," *Reports on Progress in Physics*, vol. 68, no. 10, pp. 2267-2336, 2005.
- [2] A. Rogalski, "Recent progress in infrared detector technologies," *Infrared Physics and Technology*, vol. 54, no. 3, pp. 136-154, 2011.
- [3] Y. Aron, and Y. Gronau, "Polarization in the LWIR: a method to improve target acquisition," *Infrared Technology and Applications* vol. 5783, pp. 653-662, 2005.
- [4] D. L. Smith, and C. Mailhot, "Proposal for strained type II superlattice infrared detectors," *Journal of Applied Physics*, vol. 62, no. 6, pp. 2545-2548, 1987.
- [5] A. V. Barve, S. J. Lee, S. K. Noh, and S. Krishna, "Review of current progress in quantum dot infrared photodetectors," *Laser & Photonics Reviews*, vol. 4, no. 6, pp. 738-750, 2010.
- [6] A. Rogalski, "Infrared detectors: an overview," *Infrared Physics and Technology*, vol. 43, no. 3, pp. 187-210, 2002.
- [7] A. Fiore, E. Rosencher, P. Bois, J. Nagle, and N. Laurent, "Strained InGaAs/AlGaAs quantum well infrared detectors at 4.5  $\mu\text{m}$ ," *Applied physics letters*, vol. 64, no. 4, pp. 478-480, 1994.
- [8] D. Zhang, and W. Shi, "Dark current and infrared absorption of p-doped InGaAs/AlGaAs strained quantum wells," *Applied physics letters*, vol. 73, no. 8, pp. 1095-1097, 1998.
- [9] E.-T. Kim, A. Madhukar, Z. Ye, and J. C. Campbell, "High detectivity InAs quantum dot infrared photodetectors," *Applied Physics Letters*, vol. 84, no. 17, pp. 3277-3279, 2004.
- [10] P. Bhattacharya, X. H. Su, S. Chakrabarti, G. Ariyawansa, and A. G. U. Perera, "Characteristics of a tunneling quantum-dot infrared photodetector operating at room temperature," *Applied Physics Letters*, vol. 86, no. 19, 2005.
- [11] S. Chakrabarti, A. D. Stiff-Roberts, X. H. Su, P. Bhattacharya, G. Ariyawansa, and A. G. U. Perera, "High-performance mid-infrared quantum dot infrared photodetectors," *Journal of Physics D: Applied Physics*, vol. 38, no. 13, pp. 2135-2141, 2005.

- [12] E.-T. Kim, Z. Chen, and A. Madhukar, "Tailoring detection bands of InAs quantum-dot infrared photodetectors using  $\text{In}_x\text{Ga}_{1-x}\text{As}$  strain-relieving quantum wells," *Applied Physics Letters*, vol. 79, no. 20, pp. 3341-3343, 2001.
- [13] Z. Chen, O. Baklenov, E. T. Kim, I. Mukhametzhanov, J. Tie, A. Madhukar, Z. Ye, and J. C. Campbell, "Normal incidence InAs/ $\text{Al}_x\text{Ga}_{1-x}\text{As}$  quantum dot infrared photodetectors with undoped active region," *Journal of Applied Physics*, vol. 89, no. 8, pp. 4558-4563, 2001.
- [14] K. Stewart, M. Buda, J. Wong-Leung, L. Fu, C. Jagadish, A. Stiff-Roberts, and P. Bhattacharya, "Influence of rapid thermal annealing on a 30 stack InAs/GaAs quantum dot infrared photodetector," *Journal of Applied Physics*, vol. 94, no. 8, pp. 5283-5289, 2003.
- [15] E. C. Le Ru, P. Howe, T. Jones, and R. Murray, "Strain-engineered InAs/GaAs quantum dots for long-wavelength emission," *Physical Review B*, vol. 67, no. 16, pp. 165303, 2003.
- [16] L. Fu, H. H. Tan, I. McKerracher, J. Wong-Leung, C. Jagadish, N. Vukmirović, and P. Harrison, "Effects of rapid thermal annealing on device characteristics of In Ga As / Ga As quantum dot infrared photodetectors," *Journal of Applied Physics*, vol. 99, no. 11, pp. 114517, 2006.
- [17] S. Chakrabarti, A. D. Stiff-Roberts, P. Bhattacharya, S. Gunapala, S. Bandara, S. B. Rafol, and S. W. Kennerly, "High-temperature operation of InAs-GaAs quantum-dot infrared photodetectors with large responsivity and detectivity," *Photonics Technology Letters, IEEE*, vol. 16, no. 5, pp. 1361-1363, 2004.
- [18] R. LaPierre, M. Robson, K. Azizur-Rahman, and P. Kuyanov, "A review of III-V nanowire infrared photodetectors and sensors," *Journal of Physics D: Applied Physics*, vol. 50, no. 12, pp. 123001, 2017
- [19] N. Anttu, and H. Xu, "Coupling of light into nanowire arrays and subsequent absorption," *Journal of nanoscience and nanotechnology*, vol. 10, no. 11, pp. 7183-7187, 2010.
- [20] N. Anttu, A. Abrand, D. Asoli, M. Heurlin, I. Åberg, L. Samuelson, and M. Borgström, "Absorption of light in InP nanowire arrays," *Nano Research*, vol. 7, no. 6, pp. 816-823, 2014.
- [21] P. Kailuweit, M. Peters, J. Leene, K. Mergenthaler, F. Dimroth, and A. W. Bett, "Numerical simulations of absorption properties of InP nanowires for solar cell applications," *Progress in photovoltaics: research and applications*, vol. 20, no. 8, pp. 945-953, 2012.
- [22] N. Anttu, and H. Xu, "Efficient light management in vertical nanowire arrays for photovoltaics," *Optics express*, vol. 21, no. 103, pp. A558-A575, 2013.

- [23] J. Kupec, R. L. Stoop, and B. Witzigmann, "Light absorption and emission in nanowire array solar cells," *Optics Express*, vol. 18, no. 26, pp. 27589-27605, 2010.
- [24] H. Guo, L. Wen, X. Li, Z. Zhao, and Y. Wang, "Analysis of optical absorption in GaAs nanowire arrays," *Nanoscale research letters*, vol. 6, no. 1, pp. 617, 2011.
- [25] N. Dhindsa, A. Chia, J. Boulanger, I. Khodadad, R. LaPierre, and S. S. Saini, "Highly ordered vertical GaAs nanowire arrays with dry etching and their optical properties," *Nanotechnology*, vol. 25, no. 30, pp. 305303, 2014.
- [26] Y. Hu, R. R. LaPierre, M. Li, K. Chen, and J.-J. He, "Optical characteristics of GaAs nanowire solar cells," *Journal of Applied Physics*, vol. 112, no. 10, pp. 104311, 2012.
- [27] P. M. Wu, N. Anttu, H. Xu, L. Samuelson, and M.-E. Pistol, "Colorful InAs nanowire arrays: from strong to weak absorption with geometrical tuning," *Nano letters*, vol. 12, no. 4, pp. 1990-1995, 2012.
- [28] L. Cao, J. S. White, J.-S. Park, J. A. Schuller, B. M. Clemens, and M. L. Brongersma, "Engineering light absorption in semiconductor nanowire devices," *Nature materials*, vol. 8, no. 8, pp. 643, 2009.
- [29] B. Wang, and P. W. Leu, "Tunable and selective resonant absorption in vertical nanowires," *Optics Letters*, vol. 37, no. 18, pp. 3756-3758, 2012.
- [30] Y. Zeng, Q. Ye, and W. Shen, "Design principles for single standing nanowire solar cells: going beyond the planar efficiency limits," *Scientific reports*, vol. 4, pp. 4915, 2014.
- [31] K. Azizur-Rahman, and R. LaPierre, "Wavelength-selective absorptance in GaAs, InP and InAs nanowire arrays," *Nanotechnology*, vol. 26, no. 29, pp. 295202, 2015.
- [32] J. Bures, "Guides Optics: Optical Fibers and All-fiber Components," WILEY-VCH Verlag, Weinheim, Germany, 2009.
- [33] J. Zhang, N. Dhindsa, A. Chia, J. Boulanger, I. Khodadad, S. Saini, and R. LaPierre, "Multi-spectral optical absorption in substrate-free nanowire arrays," *Applied Physics Letters*, vol. 105, no. 12, pp. 123113, 2014/09/22, 2014.
- [34] M. Heiss, and A. F. i. Morral, "Fundamental limits in the external quantum efficiency of single nanowire solar cells," *Applied Physics Letters*, vol. 99, no. 26, pp. 263102, 2011.

- [35] X. Li, and Y. Zhan, "Enhanced external quantum efficiency in rectangular single nanowire solar cells," *Applied Physics Letters*, vol. 102, no. 2, pp. 021101, 2013.
- [36] Z. Fan, P.-c. Chang, J. G. Lu, E. C. Walter, R. M. Penner, C.-h. Lin, and H. P. Lee, "Photoluminescence and polarized photodetection of single ZnO nanowires," *Applied physics letters*, vol. 85, no. 25, pp. 6128-6130, 2004.
- [37] J. Wang, M. S. Gudiksen, X. Duan, Y. Cui, and C. M. Lieber, "Highly polarized photoluminescence and photodetection from single indium phosphide nanowires," *Science*, vol. 293, no. 5534, pp. 1455-1457, 2001.
- [38] S. Han, W. Jin, D. Zhang, T. Tang, C. Li, X. Liu, Z. Liu, B. Lei, and C. Zhou, "Photoconduction studies on GaN nanowire transistors under UV and polarized UV illumination," *Chemical Physics Letters*, vol. 389, no. 1-3, pp. 176-180, 2004.
- [39] W. Wei, X.-Y. Bao, C. Soci, Y. Ding, Z.-L. Wang, and D. Wang, "Direct heteroepitaxy of vertical InAs nanowires on Si substrates for broad band photovoltaics and photodetection," *Nano letters*, vol. 9, no. 8, pp. 2926, 2009.
- [40] H. H. Gao, A. Krier, and V. V. Sherstnev, "Room-temperature InAs<sub>0.89</sub>Sb<sub>0.11</sub> photodetectors for CO detection at 4.6  $\mu\text{m}$ ," *Applied Physics Letters*, vol. 77, no. 6, pp. 872-874, 2000.
- [41] A. Rakovska, V. Berger, X. Marcadet, B. Vinter, K. Bouzehouane, and D. Kaplan, "Optical characterization and room temperature lifetime measurements of high quality MBE-grown InAsSb on GaSb," *Semiconductor science and technology*, vol. 15, no. 1, pp. 34, 2000.
- [42] N. A. J. Svensson, N. Vainorius, B. M. Borg., and a. L.-E. Wernersson, "Diameter-Dependent Photocurrent in InAsSb Nanowire Infrared Photodetectors," *Nano Letter*, vol. 13, no. 4, pp. 1380-1385, 2013.
- [43] Z. Liu, T. Luo, B. Liang, G. Chen, G. Yu, X. Xie, D. Chen, and G. Shen, "High-detectivity InAs nanowire photodetectors with spectral response from ultraviolet to near-infrared," *Nano Research*, vol. 6, no. 11, pp. 775-783, 2013.
- [44] J. Miao, W. Hu, N. Guo, Z. Lu, X. Zou, L. Liao, S. Shi, P. Chen, Z. Fan, J. C. Ho, T.-X. Li, X. S. Chen, and W. Lu, "Single InAs nanowire room-temperature near-infrared photodetectors," *ACS nano*, vol. 8, no. 4, pp. 3628, 2014.
- [45] Y. Han, X. Zheng, M. Fu, D. Pan, X. Li, Y. Guo, J. Zhao, and Q. Chen, "Negative photoconductivity of InAs nanowires," *Physics Chemistry Chemical Physics*, vol. 18, no. 2, pp. 818-826, 2015.
- [46] M. D. Thompson, A. Alhodaib, A. P. Craig, A. Robson, A. Aziz, A. Krier, J. Svensson, L.-E. Wernersson, A. M. Sanchez, and A. R. J. Marshall, "Low

Leakage-Current InAsSb Nanowire Photodetectors on Silicon,” *Nano letters*, vol. 16, no. 1, pp. 182, 2016.

- [47] A. L. Efros, and M. Rosen, “The electronic structure of semiconductor nanocrystals,” *Annual Review of Materials Science*, vol. 30, no. 1, pp. 475-521, 2000.
- [48] L. E. Jensen, M. T. Björk, S. Jeppesen, A. I. Persson, B. J. Ohlsson, and L. Samuelson, “Role of surface diffusion in chemical beam epitaxy of InAs nanowires,” *Nano Letters*, vol. 4, no. 10, pp. 1961-1964, 2004.
- [49] K. A. Dick, K. Deppert, L. Samuelson, and W. Seifert, “Optimization of Au-assisted InAs nanowires grown by MOVPE,” *Journal of Crystal Growth*, vol. 297, no. 2, pp. 326-333, 2006.
- [50] B. M. Borg, K. A. Dick, J. Eymery, and L.-E. Wernersson, “Enhanced Sb incorporation in InAsSb nanowires grown by metalorganic vapor phase epitaxy,” *Applied Physics Letters*, vol. 98, no. 11, pp. 113104, 2011.
- [51] D. Ercolani, M. Gemmi, L. Nasi, F. Rossi, M. Pea, A. Li, G. Salviati, F. Beltram, and L. Sorba, “Growth of InAs/InAsSb heterostructured nanowires,” *Nanotechnology*, vol. 23, no. 11, pp. 115606, 2012.
- [52] M. Pea, D. Ercolani, A. Li, M. Gemmi, F. Rossi, F. Beltram, and L. Sorba, “Suppression of lateral growth in InAs/InAsSb heterostructured nanowires,” *Journal of Crystal Growth*, vol. 366, pp. 8-14, 2013.
- [53] M. Sourribes, I. Isakov, M. Panfilova, H. Liu, and P. A. Warburton, “Mobility Enhancement by Sb-mediated Minimisation of Stacking Fault Density in InAs Nanowires Grown on Silicon,” *Nano Letters*, vol. 14, no. 3, pp. 1643-1650, 2014.
- [54] W. Du, X. Yang, X. Wang, H. Pan, H. M. Ji, S. Luo, T. Yang, and Z. Wang, “The self-seeded growth of InAsSb nanowires on silicon by metal-organic vapor phase epitaxy,” *Journal Of Crystal Growth*, vol. 396, pp. 33-37, 2014.
- [55] W. Du, X. Yang, H. Pan, X. Wang, H. Ji, S. Luo, X. Ji, Z. Wang, and T. Yang, “Two different growth mechanisms for Au-free InAsSb nanowires growth on Si substrate,” *Crystal Growth & Design*, vol. 15, no. 5, pp. 2413-2418, 2015.
- [56] W. Du, X. Yang, H. Pan, X. Ji, H. Ji, S. Luo, X. Zhang, Z. Wang, and T. Yang, “Controlled-direction growth of planar InAsSb nanowires on Si substrates without foreign catalysts,” *Nano letters*, vol. 16, no. 2, pp. 877-882, 2016.
- [57] Q. Z. E. A. Anyebe, A. M. Sanche, S. Lawso, A. J. Robson, L. Ponomaren, A. Zhukov and O. Kolosov, “Self-catalysed growth of InAs nanowires on bare Si

substrates by droplet epitaxy,” *physica status solidi (RRL) - Rapid Research Letter*, vol. 8, no. 7, pp. 658–662, 2014.

- [58] Q. D. Zhuang, E. A. Anyebe, A. M. Sanchez, M. K. Rajpalke, T. D. Veal, A. Zhukov, B. J. Robinson, F. Anderson, O. Kolosov, and V. Fal’ko, “Graphitic platform for self-catalysed InAs nanowires growth by molecular beam epitaxy,” *Nanoscale research letters*, vol. 9, no. 1, pp. 321, 2014.
- [59] A. C. Farrell, W.-J. Lee, P. Senanayake, M. A. Haddad, S. V. Prikhodko, and D. L. Huffaker, “High-Quality InAsSb Nanowires Grown by Catalyst-Free Selective-Area Metal-Organic Chemical Vapor Deposition,” *Nano letters*, vol. 15, no. 10, pp. 6614, 2015.
- [60] H. Kroemer, “The 6.1 Å family (InAs, GaSb, AlSb) and its heterostructures: a selective review,” *Physica E: Low-dimensional Systems and Nanostructures*, vol. 20, no. 3, pp. 196-203, 2004.
- [61] M. E. Pistol, and C. E. Pryor, “Band structure of core-shell semiconductor nanowires,” *Physical Review B*, vol. 78, no. 11, 2008.
- [62] L. Namazi, M. Nilsson, S. Lehmann, C. Thelander, and K. A. Dick, “Selective GaSb radial growth on crystal phase engineered InAs nanowires,” *Nanoscale*, vol. 7, no. 23, pp. 10472-10481, 2015.
- [63] I. Knez, R.-R. Du, and G. Sullivan, “Evidence for helical edge modes in inverted InAs/GaSb quantum wells,” *Physical review letters*, vol. 107, no. 13, pp. 136603, 2011.
- [64] A. N. Baranov, N. Bertru, Y. Cuminal, G. Boissier, C. Alibert, and A. Joullié, “Observation of room-temperature laser emission from type III InAs/GaSb multiple quantum well structures,” *Applied Physics Letters*, vol. 71, no. 6, pp. 735-737, 1997.
- [65] A. W. Dey, J. Svensson, B. M. Borg, M. Ek, and L.-E. Wernersson, “Single InAs/GaSb nanowire low-power CMOS inverter,” *Nano letters*, vol. 12, no. 11, pp. 5593, 2012.
- [66] B. M. Borg, K. A. Dick, B. Ganjipour, M.-E. Pistol, L.-E. Wernersson, and C. Thelander, “InAs/GaSb heterostructure nanowires for tunnel field-effect transistors,” *Nano letters*, vol. 10, no. 10, pp. 4080, 2010.
- [67] M. Ek, B. M. Borg, A. W. Dey, B. Ganjipour, C. Thelander, L. E. Wernersson, and K. A. Dick, “Formation of the axial heterojunction in GaSb/InAs(Sb) nanowires with high crystal quality,” *Crystal Growth and Design*, vol. 11, no. 10, pp. 4588-4593, 2011.

- [68] B. Ganjipour, M. Ek, B. Mattias Borg, K. A. Dick, M.-E. Pistol, L.-E. Wernersson, and C. Thelander, "Carrier control and transport modulation in GaSb/InAsSb core/shell nanowires," *Applied Physics Letters*, vol. 101, no. 10, 2012.
- [69] B. Ganjipour, S. Sepehri, A. W. Dey, O. Tizno, B. Mattias Borg, K. A. Dick, L. Samuelson, L.-E. Wernersson, and C. Thelander, "Electrical properties of GaSb/InAsSb core/ shell nanowires," vol. 25, no. 42, pp. 425201, 2014.
- [70] T. Rieger, D. Grtzmacher, and M. I. Lepsa, "Misfit dislocation free InAs/GaSb coreshell nanowires grown by molecular beam epitaxy," *Nanoscale*, vol. 7, no. 1, pp. 356-364, 2014.
- [71] M. Rocci, F. Rossella, U. P. Gomes, V. Zannier, F. Rossi, D. Ercolani, L. Sorba, F. Beltram, and S. Roddaro, "Tunable Esaki Effect in Catalyst-Free InAs/GaSb Core-Shell Nanowires," *Nano letters*, vol. 16, no. 12, pp. 7950, 2016.
- [72] S. J. Koester, C. R. Bolognesi, E. L. Hu, H. Kroemer, and M. J. Rooks, "Quantized conductance in an InAs/AlSb split-gate ballistic constriction with 1.0  $\mu\text{m}$  channel length," *Physical Review B*, vol. 49, no. 12, pp. 8514-8517, 1994.
- [73] S. J. Koester, C. R. Bolognesi, M. J. Rooks, E. L. Hu, and H. Kroemer, "Quantized conductance of ballistic constrictions in InAs/AlSb quantum wells," *Applied Physics Letters*, vol. 62, no. 12, pp. 1373-1375, 1993.
- [74] C. R. Bolognesi, E. J. Caine, and H. Kroemer, "Improved charge control and frequency performance in InAs/ AlSb- based heterostructure field- effect transistors," *Electron Device Letters, IEEE*, vol. 15, no. 1, pp. 16-18, 1994.
- [75] B. Brar, and H. Kroemer, "Influence of impact ionization on the drain conductance in InAs-AlSb quantum well heterostructure field-effect transistors," *Electron Device Letters, IEEE*, vol. 16, no. 12, pp. 548-550, 1995.
- [76] J. P. Heida, B. van Wees, J. Kuipers, T. M. Klapwijk, and G. Borghs, "Spin-orbit interaction in a two-dimensional electron gas in a InAs/AlSb quantum well with gate-controlled electron density," *Physical Review B*, vol. 57, no. 19, pp. 11911-11914, 1998.
- [77] M. J. Yang, K. A. Cheng, C. H. Yang, and J. C. Culbertson, "A nano fabrication scheme for InAs/AlSb heterostructures," *Applied Physics Letters*, vol. 80, no. 7, pp. 1201-1203, 2002.
- [78] V. Aleshkin, V. Gavrilenko, A. Ikonnikov, S. Krishtopenko, Y. Sadofyev, and K. Spirin, "Exchange enhancement of the g factor in InAs/AlSb heterostructures," *Semiconductors*, vol. 42, no. 7, pp. 828-833, 2008.

- [79] G. Moschetti, H. Zhao, P. A. Nilsson, S. Wang, A. Kalabukhov, G. Dambrine, S. Bollaert, L. Desplanque, X. Wallart, and J. Grahn, “Anisotropic transport properties in InAs/AlSb heterostructures,” *Applied Physics Letters*, vol. 97, no. 24, pp. 243510, 2010.

# Chapter 4

## Experimental techniques

### 4.1 Molecular Beam Epitaxy

Molecular beam epitaxy (MBE) was invented in the early 1970s as a means of growing epitaxial layers of compound semiconductors. Since that time, it has been used for growing III-V compound semiconductors [1]. MBE is an ultra-high vacuum (UHV) conditions ( $10^{-9} - 10^{-11}$  Torr) based technique used for the production of high quality epitaxial materials and quantum structures. Nowadays, it is a sophisticated tool used in the development of electronic and optoelectronic devices. It offers a high degree of control for a number of important parameters; very high purity of the epilayers, atomically abrupt interfaces between different epilayers, ability to control each layer composition, ability to grow strained layers and good control of the doping level of each layer independently.

#### 4.1.1 MBE apparatus

The constituent elements of a semiconductor in MBE are in the form of molecular beams, which are formed from thermally evaporated elemental sources. These molecular beams are deposited onto a heated substrate to form a thin epitaxial layer. There are a couple of factors, which are critical in MBE. The first one is that the material sources should be extremely pure, and that the whole process should be performed in an ultra-high vacuum environment in order to obtain high-purity layers. Another important feature is that growth rates are typically a few  $\text{\AA}$  per second and the beams

can be shuttered in a fraction of a second, allowing atomically abrupt transition from one material to another. The MBE system used in Lancaster University is a VG V80H solid source MBE, which generally consists of three main vacuum chambers as shown in Fig (4.1). The first is the preparation chamber, which is used for series of processes including storage and outgassing samples (where gases are desorbed out of the substrates). The second is a load-lock chamber where substrates are transferred into and out of the system, which can be independently vented and pumped quickly. The last is a growth chamber where the samples are loaded for the growth.

The substrate acts as a seed crystal, motivating the depositing film to take on a lattice structure and orientation identical to that of the substrate. If the growing film has the same material and crystal structure as the substrate then the process is called homoepitaxy, otherwise it is referred to as heteroepitaxy [2]

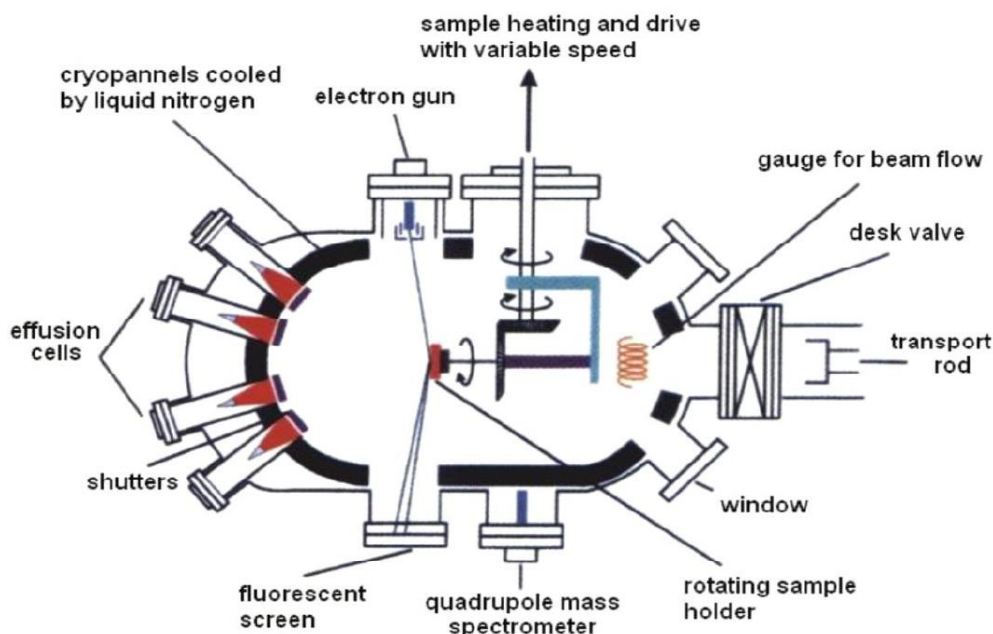


Figure 4.1: Schematic of the essential components of an MBE growth chamber showing the essential components including the effusion cells, shutters, and the RHEED system [9].

Samples are loaded onto the holder of the growth chamber where they can be heated and rotated, to allow the substrate to face the material source, and allow deposition onto the surface of the sample during growth [3]. The chamber pressure can be read by the ion gauge, which is mounted on the side opposite the sample or be placed facing the material sources to measure the beam equivalent pressure (BEP) of the material sources. The MBE system is illustrated in Fig (4.1).

### **4.1.2 Reflection high energy electron diffraction**

#### **(RHEED)**

This technique allows for in-situ monitoring of the surface structure of the growing layer during growth. As well as this, it is used for the calibration of growth rates and it tells us about the desorption of native oxide of the sample. The RHEED pattern results from striking a beam of high-energy electrons (10-40 keV) which are produced by a gun. The latter is operated at voltage of 12.5-15 volt and current of 2.25 A. The electronic beam strikes the surface with a shallow angle ( $0.5^{\circ}$ - $3^{\circ}$ ), therefore, the diffracted electrons only provide details about the surface morphology. The diffraction pattern can be observed via a fluorescent screen on the opposite side of the growth chamber. The RHEED pattern appearance provides information about surface morphology. If the surface is rough the pattern appears spotty, while a streaky pattern indicates to smooth surface.

RHEED oscillation intensity can be employed for measuring the growth rate. The RHEED shows bright spots when full monolayer completes and the oscillation will be in its maximum intensity (Fig4.2a). When the second monolayer starts, there will be atoms and islands, which reduces the intensity, making the pattern dim until the layer is fully covered, the intensity then maximizes and the pattern will be bright again. By

counting the number of oscillation per second, the growth rate can be deduced using the following relation:

$$\text{Growth rate} = \frac{N_{osc} \cdot \frac{a_0}{2}}{t} \quad (4.1)$$

Where  $N_{osc}$  is the number of oscillations,  $a_0$  is the lattice constant in  $\mu\text{m}$ , and  $t$  is the total time in seconds.

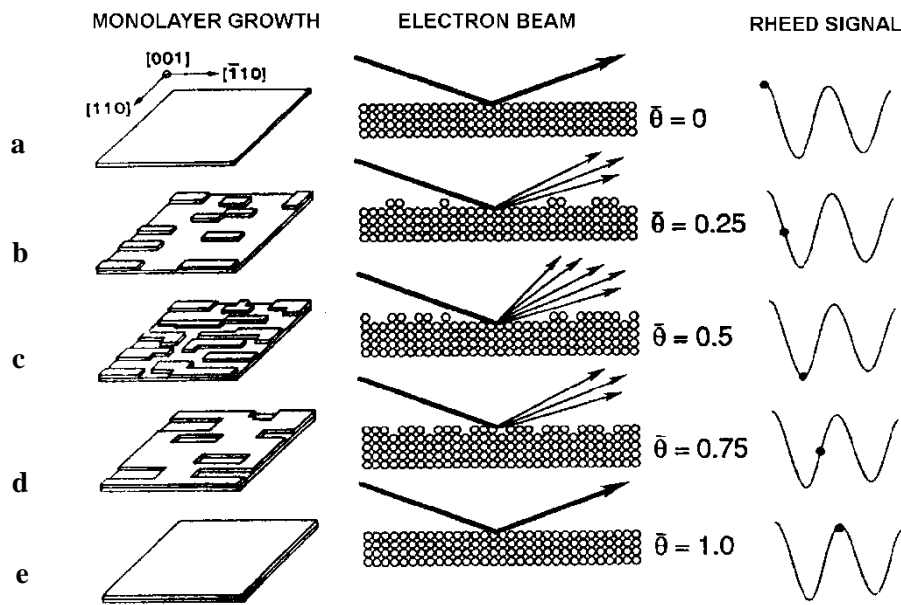


Figure (4.2): RHEED oscillations; beam and the RHEED intensity are shown as a function of the surface morphology [1].

## 4.2. X-Ray diffraction (XRD)

X-Ray is non-destructive technique, which is used to study the composition of the grown materials and determine the crystal structure and phase. The wavelength of X-rays, ranges from 0.1 to 100  $\text{\AA}$  and is in the range of interatomic distances or unit cell sizes [4]. The crystal lattice acts as a diffraction grating for incoming X-ray radiation. The latter interferes with each other either constructively or destructively, depending on the inter-planar spacing  $d$ , Fig (4.3), and the wavelength of the incident radiation ( $\lambda$ ). Constructive interference produces diffraction peaks with a particular angular

relationship between the incident beam, the crystal structure and the specimen orientation, which is known as the x-ray diffraction pattern. Bragg's law deduced a relationship that gives the condition of the constructive interference. This condition implies that the incident waves reflected by identical planes with a separation distance  $d_{hkl}$  are in phase if the path difference between them is equal to an integral number of wavelengths see Fig (4.3).

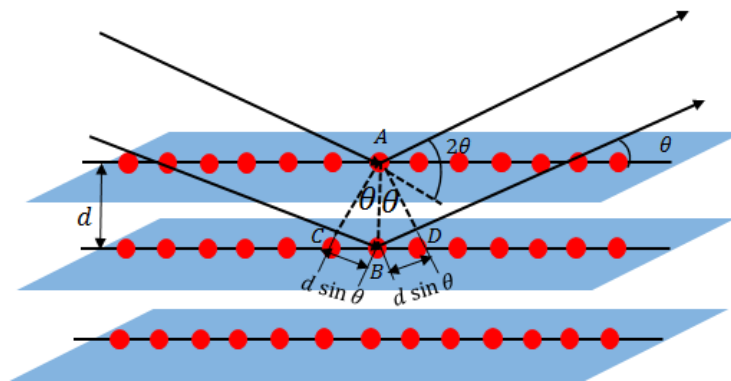


Figure (4.3): Schematic of X-ray diffraction

$$2d_{hkl} \times \sin \theta_{hkl} = n\lambda \quad (4.2)$$

Where:  $d_{hkl}$  is the inter-planar distance,  $n$  is the order of reflection,  $\theta_{hkl}$  is the diffraction angle.

The path difference between the waves scattered by atoms from  $(hkl)$  lattice planes of spacing  $d_{hkl}$  is given by:

$$(CB + BD) = (d_{hkl} \sin \theta + d_{hkl} \sin \theta) = 2d_{hkl} \sin \theta \quad (4.3)$$

Equation (4.2) is the condition of constructive interference. That means to obtain a constructive interference, the path difference between the incidents and reflected rays should be equal to an integer number of their wavelength.

XRD is mainly used in the following applications for nanostructures:

1. Studying crystal structure (finding lattice parameters of the crystals).
2. Identification/quantification of crystalline orientations.
3. Determining the composition of the nanowires.

For this study, a Rigaku smart lab 9kw X-ray diffractometer (Fig 4.4) was employed using the Cu  $K\alpha_1$  radiation line ( $1.53\text{\AA}$ ). XRD measurements were first calibrated by diffraction from a Si (111) substrate.

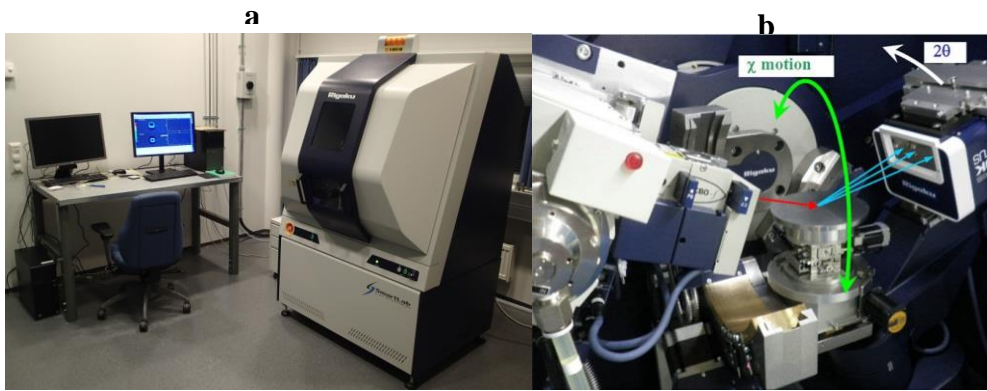


Figure (4.4): a) X-ray Rigaku smart lab. b) X-ray diffractometer

#### 4.2.1. Determination lattice parameters:

The Lattice constant of the crystals belonging to the material of the grown nanowire can be calculated from x-ray diffraction pattern. Firstly, the  $d$  spacing is calculated from observed diffraction angles by applying Bragg's law eq. (4.2) and then the lattice constant can be found from the relation between  $a$  and  $d$  for each crystal structure. For example, the lattice constant for FCC crystal structure is given by following:

$$d_{hkl} = \frac{a}{\sqrt{h^2+k^2+l^2}} \quad (4.4)$$

For hexagonal structure ( $d$ ) becomes:

$$\frac{1}{d^2_{hkl}} = \frac{4}{3} \left( \frac{h^2 + hk + k^2}{a^2} \right) + \frac{l^2}{c^2} \quad (4.5)$$

Where  $h, k, l$  are Miller indices, and  $a$ , and  $c$  are lattice constant in the  $x$  and  $z$  direction, respectively.

#### 4.2.2. Determining the composition of the nanowires

Vegard's law is an empirical rule which assumes that at constant temperature, there is a linear dependence between the lattice constant of the alloy and the concentrations of the constituent materials [5]. Tuning the band gap of materials can be achieved by using alloys. In ternary alloys e.g,  $A_xB_{1-x}C$ , the properties of A and B in the compound ranging from AC to BC for  $x=1$  and  $x=0$ , respectively [6]. According to Vegard's law, any change in the materials composition  $x$  of the alloy changes the lattice constant accordingly. Materials composition in the alloy can be calculated from Vegard's law from the following equation:

$$a^{A_xB_{1-x}C} = xa^{AC} + (1 - x)a^{BC} \quad (4.6a)$$

Where  $a^{A_xB_{1-x}C}$  is the lattice constant of the alloy,  $a^{AC}$  is the lattice constant of first and third material in the ternary alloy,  $a^{BC}$  is the lattice constant of the second and third material in the alloy and  $x$  is the composition of material A. In III-V semiconductors. A represents group III material while B, C are materials that belong to group V. In our case the alloy is InAsSb NWs. In order to calculate Sb composition from x-ray diffraction, the lattice spacing ( $d$ ) should be calculated first using Bragg's law either eq. (4.4) or (4.5) depending on the value of  $2\theta$  which in turn can determine the NWs' crystal phase WZ or ZB. The lattice parameters ( $a$ ) were then evaluated from the calculated ( $d$ ). The Sb mole fractions were deduced by using Vegard's law eq. (4.6b) with an assumption of lattice constant of bulk InSb (111) ( $6.47\text{\AA}$ ):

$$x = \frac{a_{InAsSb} - a_{InAs}}{a_{InSb} - a_{InAs}} \quad (4.6b)$$

Where  $a_{InAsSb}$  is the lattice constant of InAsSb determined from x-ray pattern,  $a_{InAs}$  is the theoretical value of InAs lattice constant,  $a_{InSb}$  is the lattice constant for InSb, and  $x$  is the Sb composition.

The calculation of the lattice constant in the above is valid for fully relaxed NWs where there is no strain in the NWs. For strained structure, the value of  $x$  that was found from the above calculation will result in large errors [7] because the lattice constant of the alloy as a function of materials concentration  $x$  is far from linear relationship [5].

For simple strain which results in tetragonal distortion, the lattice constant can be determined by the (relaxed) lattice constant and elastic parameters of the materials composition. Tetragonal distortion is given as follow [8]:

$$\varepsilon^{\perp} = -\frac{2\nu}{1-\nu} \varepsilon^{\parallel} \quad (4.7)$$

Where  $\varepsilon^{\perp}$ ,  $\varepsilon^{\parallel}$  are the perpendicular and parallel epilayer strains respectively and  $\nu$  is the poisson's ratio which can be given as follows [9]:

$$\nu = -\frac{2C_{12}}{C_{11}} \quad (4.8)$$

Where,  $C_{11}$  and  $C_{12}$  are the elastic stiffness constants which equal to  $8.329 \times 10^{11}$  dyn.  
cm<sup>-2</sup> and  $4.526 \times 10^{11}$  dyn .cm<sup>-2</sup>, for InAs, respectively. The lattice constants in the perpendicular direction can be found by applying the following equations of  $\varepsilon^{\parallel}$  and  $\varepsilon^{\perp}$ :

$$\varepsilon^{\parallel} = a - a_0 / a_0 \quad (4.9)$$

$$\varepsilon^{\perp} = c - c_0 / c_0 \quad (4.10)$$

Where a,c are the lattice constant of InAsSb in the parallel and perpendicular directions, respectively. The lattice constant (a) calculated from XRD angle and  $a_0$  and  $c_0$  are the theoretical values of the above lattice constant of InAs ( $6.058 \text{ \AA}$ ) and  $4.27 \text{ \AA}$ . After finding  $\varepsilon^{\perp}$  from eq (4.7) the lattice constant (c) direction can be determined from substituting the value of  $\varepsilon^{\perp}$  in eq. (4.9).

### **4.3. Scanning Electron Microscopy (SEM):**

Scanning electron microscopy with energy-dispersed analysis of an X-ray (SEM/EDX) is one of the most powerful probes of the microanalysis technique. It is widely used in nanotechnology and materials science to characterize the size, elemental composition and phase structure of the nanostructure [10] [8, 10][8, 10][8, 10] SEM uses an electron beam instead of light since it has a higher magnification and resolution, allowing for structural visualisation down to nanometre to micrometre scale, which is invisible using optical microscopy. SEM can determine defects in microstructures and spatial values of physical properties by a micron scale resolution measurement [11]. It can also tell the wurtzite (WZ) or zinc blend (ZB) ratio of the materials which constitute the nanowires. Image formation results from the interactions between the specimen and signal produced from the electron beam. There are two types of these interactions: elastic and inelastic interactions [3].

Elastic Scattering is characterized by energy loss during the collision and by the wide-angle directional change of the scattered electron. The incident electrons that are

scattered elastically are called backscattered electrons (BSE), and produce a beneficial signal for imaging the samples.

Inelastic scattering results from different interactions between the incident electrons and the electrons and atoms of the specimen, transferring great energy to that atom from the primary beam electron. The excitation of the sample electrons within the ionization of specimen atoms leads to the generation of secondary electrons (SE), which have energies of less than 50eV and are utilized to image or analyse the sample. In addition, there are a number of other signal changes when an electron beam strikes a sample, including x-rays characterization, Auger electrons, and cathode photoluminescence as shown in Fig (4.5).

SEM used in this study is the JEOL JSM-7800F with ultrahigh resolution at ultra-low kV imaging. See Fig (4.6).

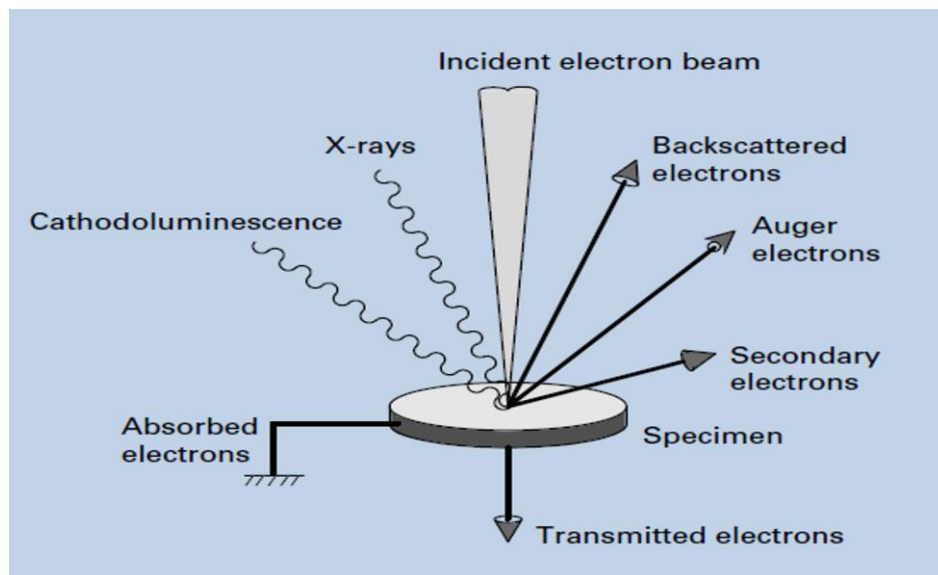


Figure 4.5: emission of various electrons and electromagnetic waves from the specimen [3]



Figure 4.6: SEM used in this study.

## 4.4 Transmission Electron Microscopy (TEM)

TEM is an indispensable and highly sophisticated tool for imaging nanostructures, providing structural information and chemical composition details through the interactions of high-energy electrons with electrons in the specimen [12].

Fig (4.6a) is a schematic diagram of TEM technique. The TEM system consists of five main components:

1. An electron gun which produces the electron beam, by accelerating large voltage ranging from 100-1000kV.
2. Condenser lenses, which control the intensity of the electron beam and convergence, angle through apertures which are fitted to the lenses.
3. Objective lenses, which are the most important part of the TEM as they produce two main modes: image plane mode where the specimen's image forms and back focal plane [13] at which produces diffraction patterns.

4. Intermediate and projector lenses, which work together or individually to give two or three -stage magnification of the image formed by the objective lenses.
5. A fluorescent screen for viewing the image, which is connected with digital camera for recording the image. These two parts made up the image recording system.

The process of imaging a sample can be described as follows: the gun emits an electron beam. The beam passes through the condenser lens system and falls on the sample at which the electrons transmitted and scattered. These electrons pass through the objective lens where the image and diffraction pattern of the specimen are formed. The intermediate lenses are adjusted in order to select either mode to be viewed on the florescent screen. The diffraction pattern is particularly important for determining the crystal phases, (ZB or WZ in the NWs studies). The diffraction pattern depends on the interplanar spacing of the crystalline sample, as well as the incidence angle of the electron beam on the crystal planes. Thus, each diffraction spot represents the interplanar spacing of a unique set of planes. There are different detectors which can collect the signal below the specimen. These detectors are; bright field (BF), annular dark field (ADF) and high annular dark field (HAADF). Each detector determines the mode of the field that will view the image depending on the angle that is collected by the detector from the incident signal. If the signal was collected with very small angle,  $\theta_1 < 10$  mrad, then the image would be bright field (BF). Annular dark-field (ADF) results from relatively larger collected angle, range  $10\text{mrad} < \theta_2 < 50\text{mrad}$ . The HAADF detector collects signals with angle higher than 50 mrad, see Fig (4.6b). TEM

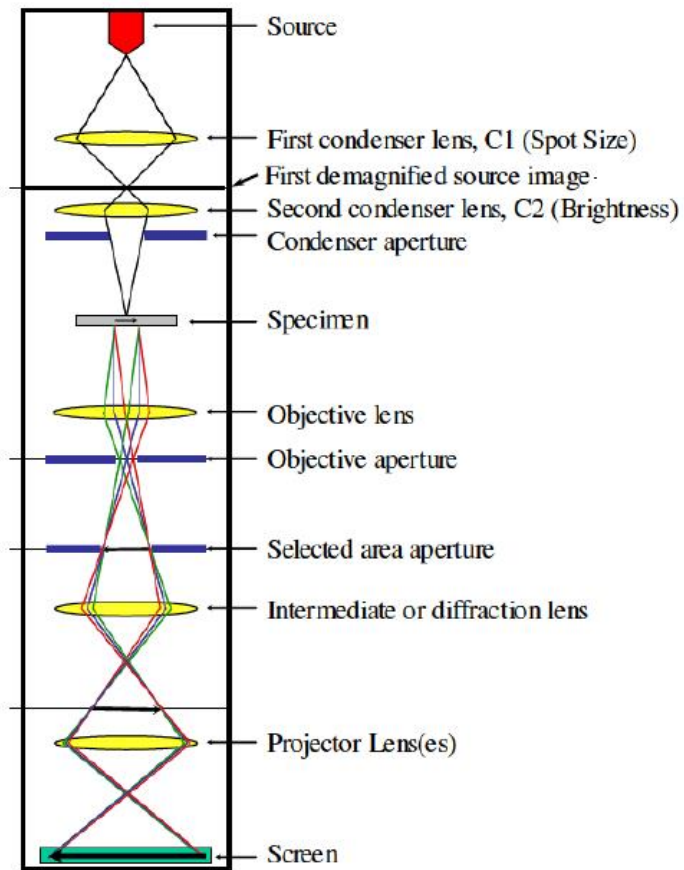


Figure 4.6: Schematic diagram of TEM system [11].

was performed by Dr. Ana Sanchez at the University of Warwick. Samples were examined using a JEOL 2100 TEM/STEM operated at 200 k. The specimens were prepared for TEM imaging. The analysis was carried out with the electron beam perpendicular to the growth direction [14].

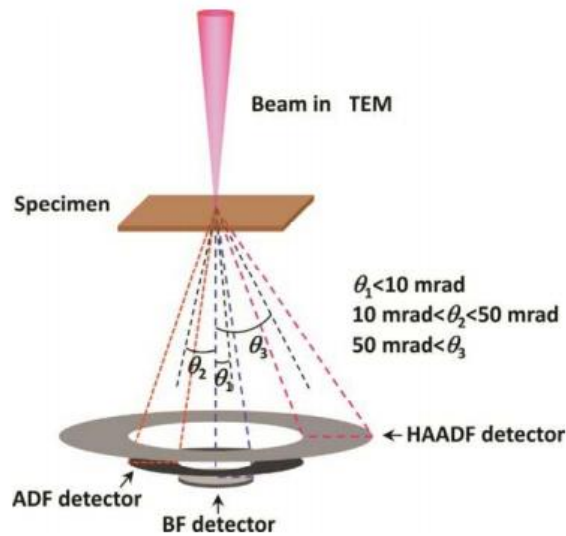


Figure (4.7): Detection of TEM images [10]

## 4.5 Atomic force microscopy (AFM)

An AFM is a mechanical imaging technique that measures the three-dimensional topography as well as imaging the sample surface. The basic principle of AFM instrument is that a sharp probe is mounted near to the end of a cantilever arm (a probe). The probe raster scans across the surface of a specimen and monitors the deflection of the arm as it meets the topographic features present on the sample surface [15]. The force of interaction between the probe and the sample is measured using a laser beam focused on the back of the cantilever. The laser light is reflected onto a position sensitive photodiode array and the position converted into an electrical signal, allowing a 3D map of the sample's surface to be pictured [16].

. There are many imaging modes available for the AFM; each mode provides a range of different information about the surface of the examined sample. These modes are; contact mode, tapping mode and non-contact mode.

In contact mode the probe remains in contact with the sample at all times. This mode has two variations: constant force and variable force. Constant force mode is used to keep the force of cantilever constant. When the z-height is altered as the arm deflected so that the probe returns to the original set point. The change in z-position is monitored and the extracted information used as a function of x, y position. Consequently, a topographical image of the sample surface is created. The variable force imaging is used only for relatively smooth surface because the feedback mechanisms are switched off to keep z-height constant and the deflection is monitored to produce topographic image. Variable force provides images with a sharper resolution than constant force mode. Contact mode is utilised when imaging of a hard and relatively flat surface is required due to its simplicity. However, there are several drawbacks result in using contact mode. First, damage to the probe or sample due to adhesive or frictional forces between the sample and the probe. Second, the resolution of the image may decrease because of the stick-slip movement of the probe tip over the surface. In addition, high forces of the interaction between the probe and the sample can cause deformation of the sample. In order to overcome the limitations of contact mode, tapping mode was developed. In non-contact mode the cantilever oscillates in similar way that it oscillates in tapping but at smaller amplitude. Oscillating frequencies allows Z-position of the cantilever to be adjusted so that keeping it out of contact with the surface [15].

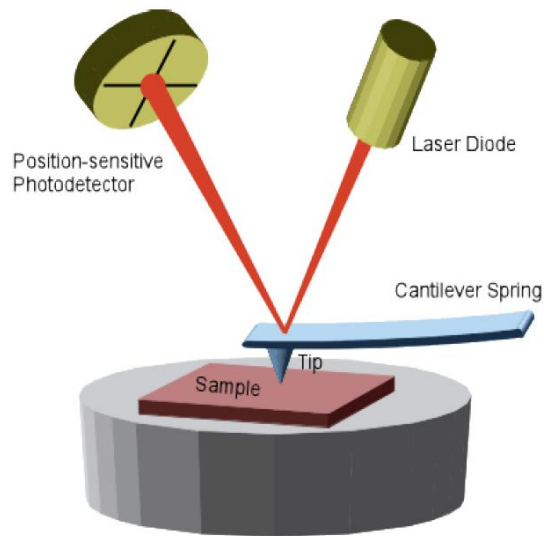


Figure 4.8: Schematic of AFM images [9]

The morphology of the indium droplets in this work was investigated by AFM using Digital Instruments multimode scanning probe microscope (MM-SPM) fitted to a nanoscope IIIa controller unit (Fig 4.8) operated in tapping mode.

## 4.6 Photoluminescence measurements

Photoluminescence spectroscopy is a non-destructive technique used for analysing optical characterization of semiconductors. The essential operating principle of PL spectroscopy is that, the laser photons with energies greater than the semi-conductor bandgap is incident on the sample and excite its electrons to the conduction band, leaving holes in the valence band. These photoexcited carriers diffuse, and either recombines non-radiatively by emitting phonons or transferring energy to other particles, or recombines radiatively to generate photons, known as luminescence.

In order to perform PL measurements, the samples were placed in a helium flow cryostat. A diode laser at wavelength of 660 nm was used for excitation of the samples, and the emission signal was detected using a liquid nitrogen cooled InSb

detector with a standard digital lock-in amplifier technique. Typical experimental set up used for PL is shown in Fig (4.9) [17].

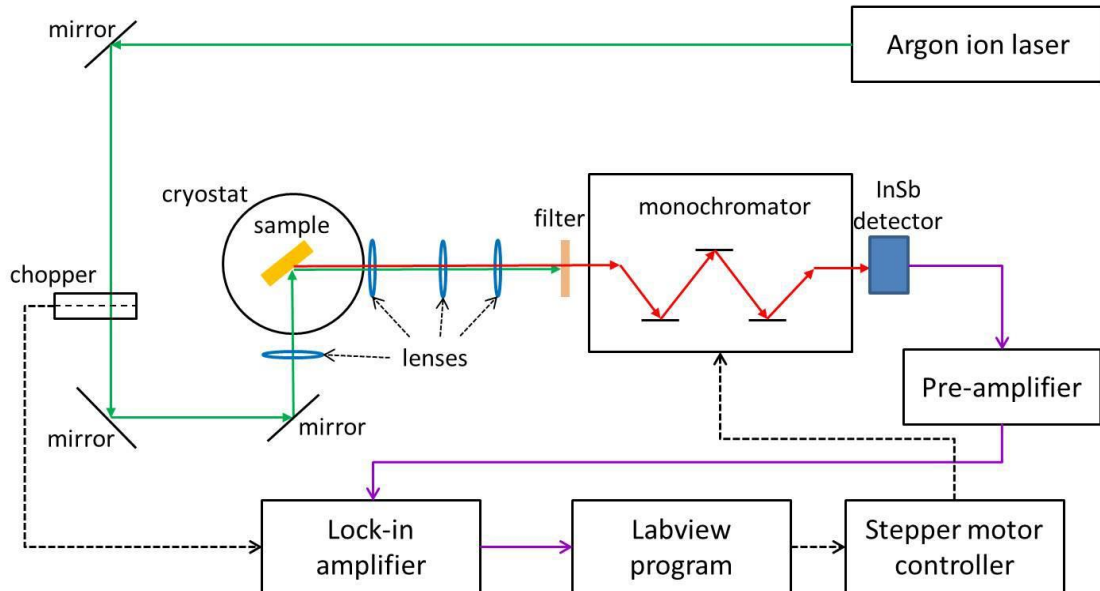


Figure 4.9: Schematic of the PL measurement set-up. Green lines: Ar laser optical path; red lines: PL emission optical path; purple lines: detected signal flow; dashed back lines: electronic control signal flow adopted from reference [13].

The laser light was chopped on its path by the chopper at a frequency of  $\sim 180$  Hz. After the laser reflects on the three beam steering mirrors and passes through a focusing lens, it strikes the sample surface with a spot size of about  $1 \text{ mm}^2$ . The highest intensity from the Ar laser was  $1.4 \text{ W}$ , by neglecting the losses in the optical path; it corresponded to up to  $14 \text{ W/cm}^2$  on the sample surface. The sample was mounted inside the cryostat, which can be cooled down to  $4 \text{ K}$  with liquid helium. The light that emitted from the sample, together with the laser light reflected by the sample surface, travels through three focusing lenses. Before entering into the monochromator, optical filter is placed in front of the laser in order to block its light out. There are two slits placed at the entrance and the exit of the monochromator to help improve the resolution. The smallest step of the monochromator corresponded to  $1 \text{ nm}$  in wavelength. The exit slit collects

the PL signal, which, is fed into the Stanford SR830 DSP lock-in amplifier after passing through the pre-amplifier. The chopper provided the lock-in reference signal. After the two amplifiers, the signal was sent to the LabVIEW program in the PC, which also controlled the grating position of the monochromator through the stepper motor control [17].

## **4.7 Current-Voltage measurements**

Current-voltage (I-V) characteristics of the devices were obtained on a home-build probe station with a Keithley B2900 A series precision Source Measure Unit (SMU) interfaced to a Labview program. The computer software allowed an increasing voltage to be passed across the device in small steps and, at the same time, the corresponding current was recorded. An upper current limit can be set to avoid damage to the device. Figure 4.10 shows the I-V measurement system that used in Physics department in Lancaster University. The SMU is connected to Labview and two probes, which contact the electrodes of the device under measurements. The device is placed on the holder of an optical microscope, which is connected to the PC via a camera. There is an LED light and laser connected to the optical microscope through a fibre to enable measuring the device under LED or Laser illumination.

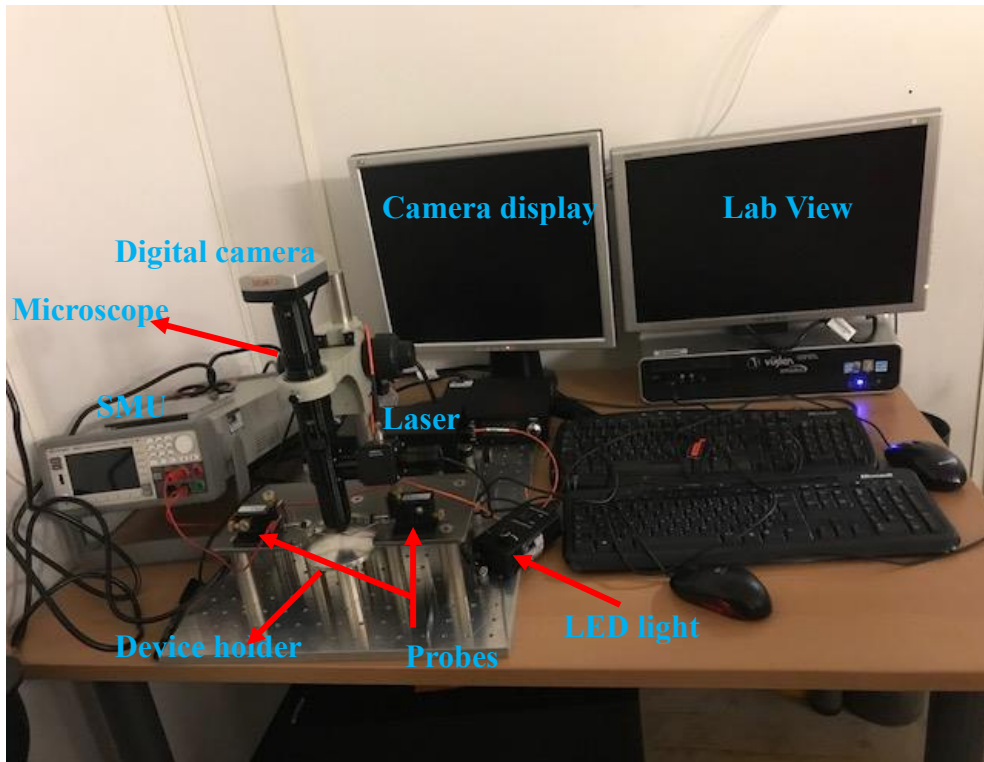


Figure (4.10) I-V measurement setting

## References

- [1] A. Cho, "Film deposition by molecular-beam techniques," *Journal of Vacuum Science and Technology*, vol. 8, no. 5, pp. S31-S38, 1971.
- [2] A. Cho, and J. Arthur, "Molecular beam epitaxy," *Progress in solid state chemistry*, vol. 10, pp. 157-191, 1975.
- [3] M. Henini, *Molecular beam epitaxy: from research to mass production*: Newnes, 2012.
- [4] B. Lavina, P. Dera, and R. T. Downs, "Modern X- ray diffraction methods in mineralogy and geosciences," *Reviews in Mineralogy and Geochemistry*, vol. 78, no. 1, pp. 1-31, 2014.
- [5] Denton, and Ashcroft, "Vegard's law," *Physical review. A, Atomic, molecular, and optical physics*, vol. 43, no. 6, pp. 3161, 1991.
- [6] T. Stankevic, "Structural investigations of nanowires using X-ray diffraction," University of Copenhagen, Faculty of Science, Niels Bohr Institute, 2015.
- [7] F. Morales, D. Gonzalez, J. Lozano, R. Garcia, S. Hauguth-Frank, V. Lebedev, V. Cimalla, and O. Ambacher, "Determination of the composition of In<sub>x</sub>Ga<sub>1-x</sub>N from strain measurements," *Acta Mater.*, 2009, pp. 5681-5692.
- [8] D. Z. B.F. Usher, S.C. Goh, T. Warminski and X.P. Huang, D. o. E. Engineering, and B. La Trobe University, VICTORIA 3083, "Poisson's ratio of GaAs," *IEEE*, 1999.
- [9] W. Z. Cai, *III-V semiconductor heterostructures : physics and devices 2003*, Trivandrum, India.: Trivandrum, India. : Research Signpost, 2003.
- [10] W. Zhou, and Z. L. Wang, *Scanning microscopy for nanotechnology: techniques and applications*: Springer science & business media, 2007.
- [11] P. Cohen, P. Pukite, J. Van Hove, and C. Lent, "Reflection high energy electron diffraction studies of epitaxial growth on semiconductor surfaces," *Journal of Vacuum Science & Technology A*, vol. 4, no. 3, pp. 1251-1258, 1986.
- [12] M. Raffel, C. E. Willert, F. Scarano, C. J. Kähler, S. T. Wereley, and J. Kompenhans, *Particle image velocimetry: a practical guide*: Springer, 2018.

- [13] H. J. Joyce, "Growth and characterisation of III-V Semiconductor nanowires for optoelectronic device applications," Australian National University, 2009.
- [14] E. Anyebe, "Growth of narrow band gap semiconductor nanowires on silicon and graphitic substrates by droplet epitaxy," Lancaster University, 2015.
- [15] W. R. Bowen, and N. Hilal, *Atomic Force Microscopy in Process Engineering: An Introduction to AFM for Improved Processes and Products*: Elsevier Science, 2009.
- [16] K. Shea, "A study of GaInNAsSb/GaAs quantum wells for use in telecommunications applications," Lancaster, 2015.
- [17] Q. Lu, "Mid-infrared antimonide based type II quantum dot lasers for use in gas sensing," Lancaster, 2015.

# Chapter 5

## Growth and structural analysis of Nanowires

### 5.1 Introduction

This chapter presents the growth procedure of growing InAs NWs, InAsSb NWs and core-shell NWs. All NWs were grown by self-catalysed droplet epitaxy by Molecular beam epitaxy. A new growth procedure was upgraded using 3-steps growth method. This new modified growth procedure provided a better quality of NWs in less time and cost than the conventional growth method. Due to large area to volume ratio, NWs suffer from severe surface states, which significantly degrade their electronic and optical properties. This drawback can be avoided by eliminating surface states which reduces unwanted ionized impurity scattering, scattering rough oxidized surfaces, electron – hole recombination and carrier depletion due to surface traps [1]. Two methods have been approached to passivate NWs; chemical passivation and structural passivation. Chemical passivation includes treating NWs with chemicals e.g coating the surface with polymers [2, 3]. Chemical passivation is a suitable method to improve ohmic contact. However, it is not the best approach for long term passivation as the effectiveness of the chemical passivation declines with time. Alternatively, structural passivation, e.g. covering the NWs core with a shell of material with a higher bandgap provides an ideal way to eliminate surface states impact. Core-shell NWs structure also

offers further advantages such as increasing the carrier mobility and conductance [4-6], driving the separation of charges [7] and enhancing the luminescence intensity [8].

In this thesis, we attempted to synthesis InAs, InAsSb NWs and core-shell NWs grown by MBE. The InAs core NW was wrapped with different shell materials to obtain different band gap alignment. SEM and HRTEM microscopy were intensively used to analysis the geometrical features and structural properties of the resulting materials. This chapter will discuss the growth and characterisation, including crystal structure and morphology of InAs NWs, InAsSb NWs and core-shell NWs. Section 5.2 provides growth optimization of InAs NWs. The new modified growth method was explained in section 5.2.4. InAsSb growth optimization presents in section 5.3. Two different core-shell structures were synthesised and discussed: section 5.4 discusses InAs/AlSb core-shell NWs while section 5.5 discusses about InAs/GaSb NWs.

## **5.2 Growth procedure of InAs nanowires by In-assisted droplet epitaxy**

### **5.2.1. Substrate preparation**

In this thesis, all the samples of NWs were grown on Si (111) substrates. In order to clean the substrates, the Silicon wafers were first soaked in acetone for a maximum of ~ 5 minutes, after that they were rinsed in methanol and isopropyl alcohol (IPA) to remove organic contaminants. After this cleaning, wet etching by hydrofluoric (HF) acid was taken place via a two-step procedure. Firstly, the wafers were soaked in 12% HF solution for (1-2) min to remove any native oxide then placed on sample holders and cleaned with HF solution for ~ 2 min to get rid of any deoxidized layer and the wafers immediately loaded into the MBE system to avoid re-oxidation. The Si

substrates were then thermally outgassed in an UHV environment at a temperature of 550 – 700 °C for 2-4 hours prior to growth initiation to eliminate adsorbed gaseous contaminants.

### **5.2.2 Epitaxial growth details**

A series of InAs NWs samples that presented in this thesis were grown on bare Si substrates by In-assisted droplet epitaxy (DE) growth technique. AFM image of In-droplets is shown in Fig (5.1). The droplet diameter, height, and density are,  $82.7 \pm 10.1$  nm,  $22.3 \pm 8.5$  nm and  $3.6 \times 10^9$  cm<sup>-2</sup> respectively.

The Indium droplets were deposited on the Si substrate at a substrate temperature of 220°C with an indium beam equivalent pressure (BEP) of  $2.2 \times 10^{-7}$  mbar for a nominal thickness of 2-5 ML. The temperature of the substrate was then ramped up to 430 - 500 °C followed by the opening of the In and As shutters simultaneously the ratio of As/In flux > 45 for NWs growth. The growth was terminated by closing both shutters simultaneously. All the InAs NWs were grown under similar conditions with growth time of 25min - 5 hours, except where otherwise mentioned. It has been found that the diameter of the droplets determined the lateral size of the resultant NWs [9-11]. The surface morphology of as-grown NWs (Figs 5.1b and 5.2) was investigated using a LEO 1530 Gemini FEG SEM working at 15 kV. The NWs length was  $1.9 \pm 1.1$  μm in length, diameter of  $62.5 \pm 3.0$  nm and density of  $1.0 \times 10^9$  cm<sup>-2</sup>.

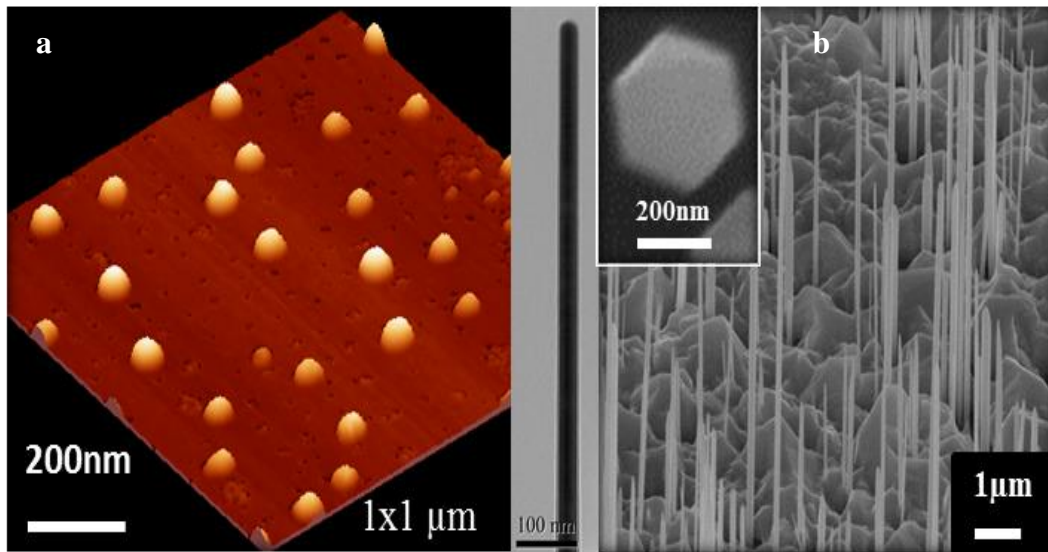


Figure 5.1: a) AFM image of In droplet. b) 45° SEM image of InAs NWs grown by In droplet catalyzed.

### 5.2.3 Morphological and structural characteristics

Figure (5.2) shows SEM images of InAs NWs. As can be seen the NWs are vertically aligned, they all show homogeneous diameter across the entire length without any tapering. The cross section of these NWs is hexagonal as shown in Fig (5.1b). Surface islands were observed in all samples. The reason behind growing these islands is that if the over layer has a higher surface free energy than underlying medium; the overlay will island rather than wet the surface. The NWs were grown at similar growth rate of (0.1 ML/sec), growth time of (1hour) and almost same growth temperature  $T_G$  of 450 °C. Each sample was grown at different As flux of  $6.2 \times 10^{-6}$ ,  $9.6 \times 10^{-6}$  and  $14 \times 10^{-6}$  mbar for samples 663,675 and 658, respectively. Previous work on InAs NWs grown by In-droplet epitaxy on bare Si substrate [12] found that there was a limited temperature window for InAs NWs grown by this method, which is 420-475 °C. In addition, the nucleation of NWs can only be realized at As rich condition, i.e BEP ratio of As/In > 50.

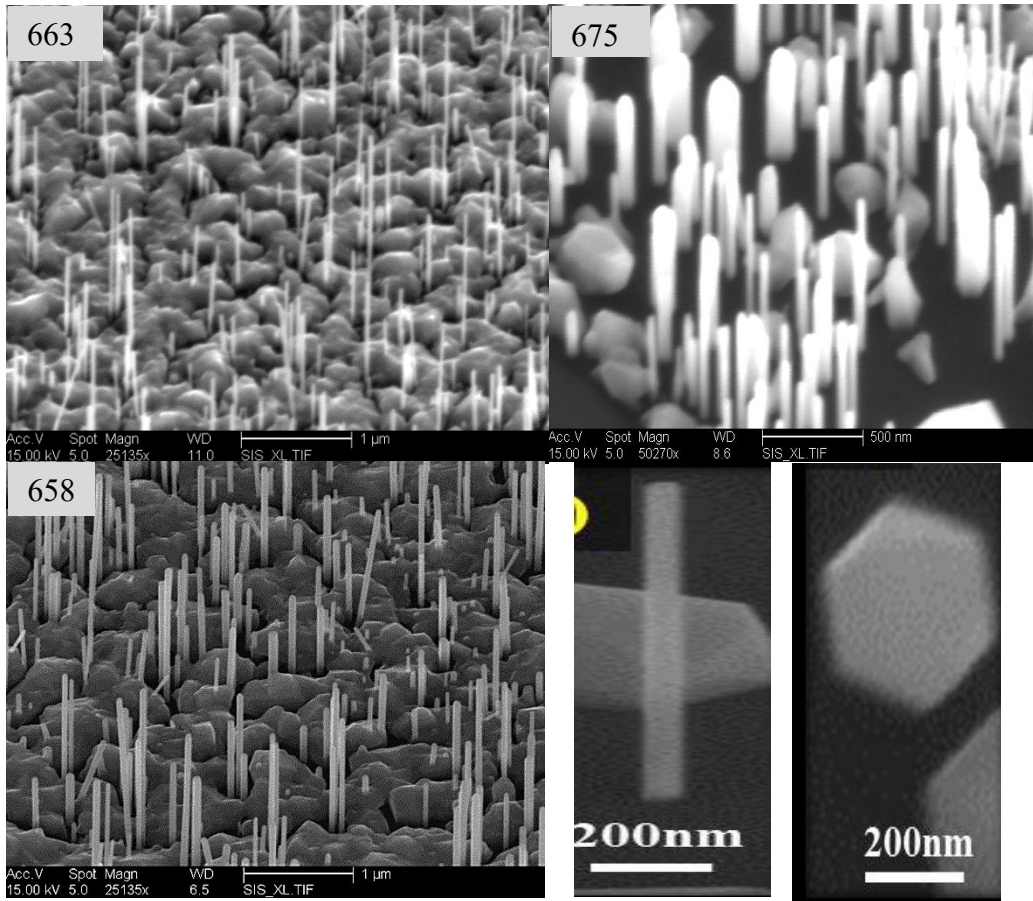


Figure 5.2: 45° tilted SEM images of three different samples of InAs NWs

## 5.2.4 Growth optimizing of InAs NWs

Relating to growth rate, it was found that the lowest growth rate ( $0.1\mu\text{m/hr}$ ) gives the highest number of distribution and the best quality of NWs in terms of geometry and morphology as shown in Fig 5.3.

Growing NWs under low growth rate results in slow growth process, time consuming and high cost. In order to minimise the above drawbacks, a new procedure of growth were modified. NWs initiated from the lowest growth rate ( $0.1\mu\text{m/hr}$ ) since it gives the best NWs geometry and density. After starting NWs growth, its growth rate ramped up

to the highest value i.e.  $0.3 \mu\text{m/hr}$ . This technique leads to NW with high density of  $8.60 \times 10^8 \text{ cm}^{-2}$ , long length of  $1.2 \pm 0.5 \mu\text{m}$ , thin diameter of  $62.8 \pm 14.9 \text{ nm}$  and relatively inexpensive. Fig 5.3d, e shows the resultant NWs. The NWs exhibit a perfect ZB single crystal structure which confirmed by X-ray pattern shown in Fig 5.4. All NWs angles at different orientations (111) and (222) are associated with ZB structure. P.Caroff et al [13] stated that at low growth temperature ( $410 \text{ }^\circ\text{C}$  in our case) the proportion of WZ in

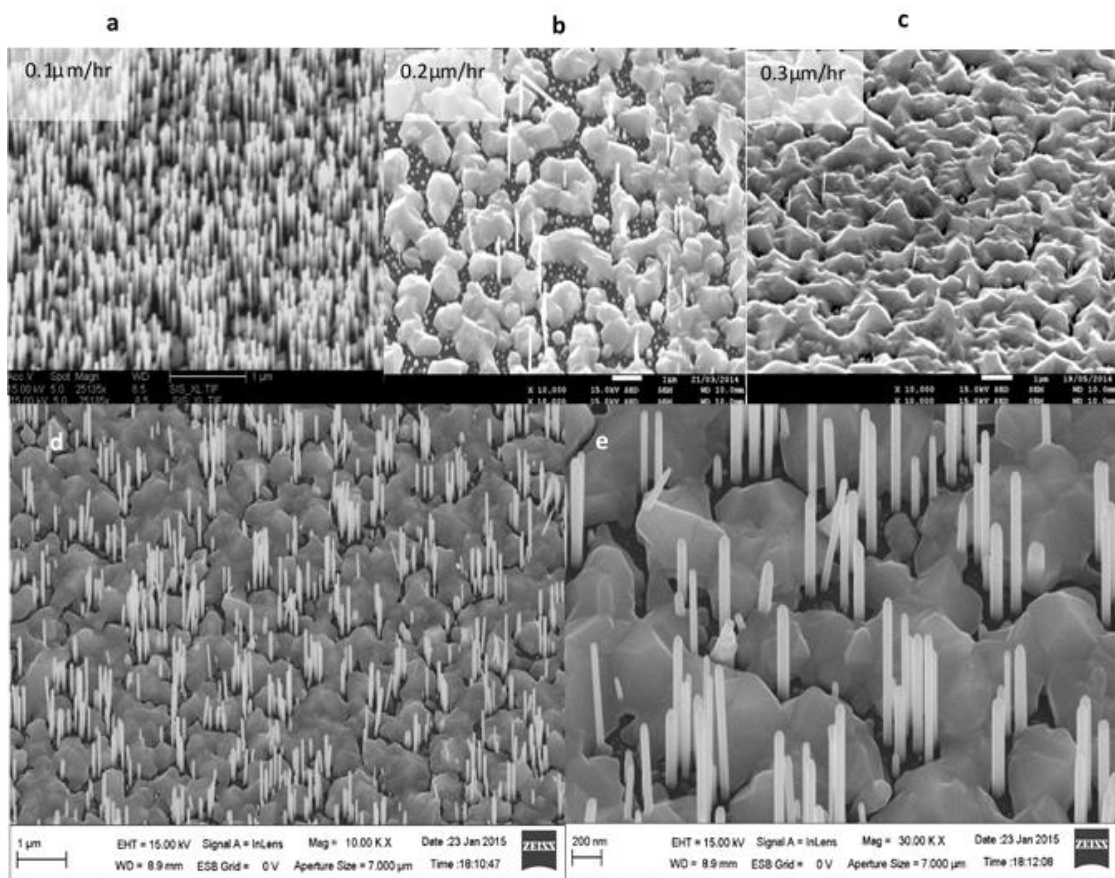


Figure 5.3: 45° tilted SEM images of InAs NWs grown by various growth rate (top panel) [11] and Grown by new method (bottom panel).

the NWs increases significantly regardless what their diameters are and allow for high-purity ZB growth at low to medium diameter (62.9 nm for the investigated NWs).

This supports our finding as well that InAs of sample 821 has a pure ZB structure. There are two random orientations of InAs, which are (220) and (311) which likely associated

with islands in the substrate but they do not belong to the NWs. Since NWs are single crystal, their XRD orientation should be repeated in periodic manner.

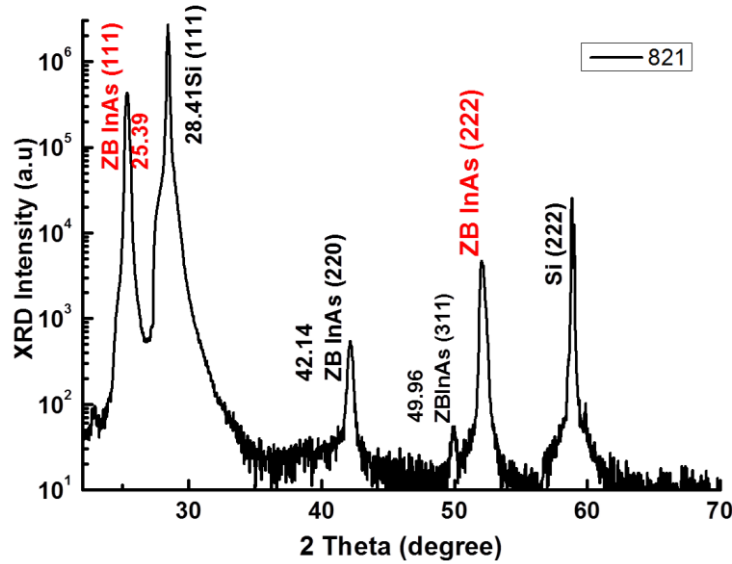


Figure 5.4: X-ray diffraction of InAs NWs

## 5.3 Growth of InAsSb NWs

### 5.3.1 Epitaxial growth details

InAsSb NWs were grown by droplet - assisted growth technique [14, 15]. The NWs are initiated from pre-deposited In droplets, which act as the seeding site to support the growth of the NWs. Due to strong surfactant effect of Sb, epitaxial growth of InAsSb NW is relatively challenging. In this thesis, series of samples were grown with Sb ranges from 3% - 19%. The Sb composition was controlled by Sb fraction flux ( $FF_{Sb}$ ) which is given by:  $FF_{Sb} = F_{Sb2} / (F_{Sb2} + F_{As4})$ , where  $F_{Sb2}$  and  $F_{As4}$  are the flux of Sb and As, respectively. This Sb composition is combined with V/III ratio in order to obtain Sb incorporation. Fig (5.5a) shows the effect of  $FF_{Sb}$  on the Sb incorporation at fixed V/III

it shows that Sb composition increases by increasing  $FF_{Sb}$ . While Fig (5.5b) demonstrates the effect of V/III flux ratio under fixed  $FF_{Sb}$ . It demonstrated that Sb

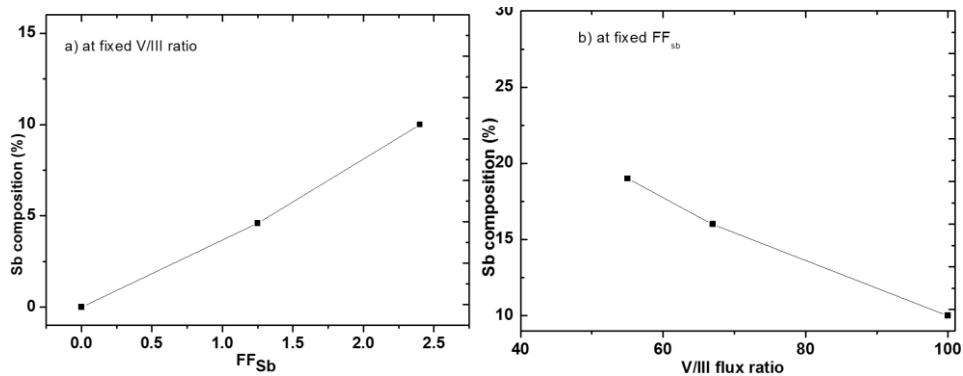


Figure 5.5: Sb composition as a function of  $FF_{Sb}$  under a fixed flux ratio of 100 (a) and a V/III flux ratio under a fixed  $FF_{Sb}$  of 2.4% (b).

composition increases by decreasing V/III flux ratio. Fig 5.6 demonstrates SEM images of the samples grown at a fixed ratio of V/III of 100 and different  $FF_{Sb}$ ; 2.4% and 4.6% (Fig 5.6a,b) and samples that grown under same  $FF_{Sb}$  (2.4%) with various V/III (67,55) Fig (5.6c,d). For high ratio of V/III of 100 with high  $FF_{Sb}$  4.6% this leads to the growth of thin film while reducing V/III ratio favors NWs growth and enhances Sb incorporation. V/III ratio of 100, 67, and 55 with low  $FF_{Sb}$  2.4% will causes of Sb incorporation of 10%, 16% and 19%, respectively. V/III ratio can be controlled by growth rate. Decreasing V/III flux ratio can be obtained by increasing the growth rate. Meanwhile, the higher growth rate favors Sb incorporation. Increasing Sb ratio causes to grow short, thick NWs and a significant drop of NWs density as shown in Fig 5.6a, c. According to the above, it can be said that growth rate and V/III ratio are the most important factors that affect NWs growth and they should be tuned wisely in order to maintain a regime of NW growth.

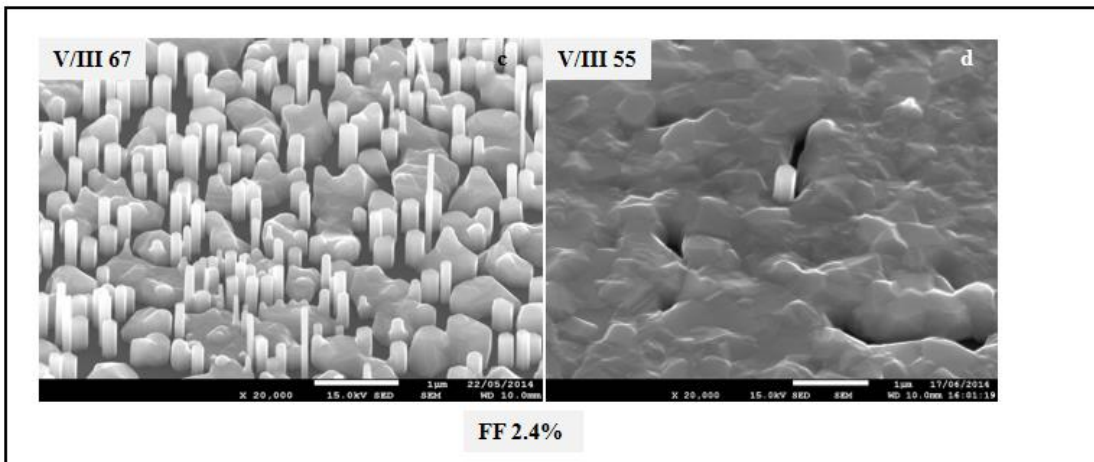
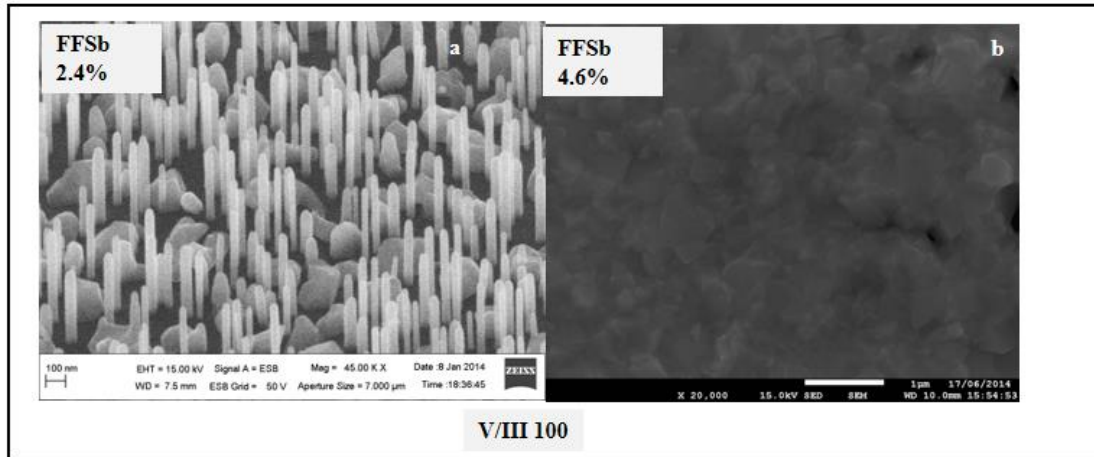


Figure 5.6: 45 tilted SEM images of InAsSb NWs grown under (a,b) a fixed V/III ratio of 100 with different  $FF_{Sb}$  and (c,d) at a fixed  $FF_{Sb}$  2.4% with different V/ III ratio.

## 5.4 Growth InAs/AlSb core-shell Nanowires

### 5.4.1 Epitaxial growth details

The core-shell NWs were grown on bare Si (111) substrate by MBE. Substrates were cleaned as described in section 5.2.1. Prior to the growth of the core NWs, indium droplets were deposited on the Si substrate as described in section (5.2.2). The substrate temperature was then ramped up for InAs NWs growth at pre-optimized growth

conditions, e.g. at a growth temperature in the range of 420-500 °C, As<sub>4</sub> beam equivalent pressure (BEP) of around 1-10×10<sup>-6</sup> mbar, and an InAs nominal growth rate of 0.1 μm/hr. The InAs NWs growth lasted for 2 hours and was followed by 1-hour deposition of AlSb shells at reduced growth temperature 400 °C and a low growth rate (0.15μm/hr) of AlSb. The growth stopped by closing Al and Sb shutters simultaneously. High-resolution X-ray diffraction (HRXRD) measurements were performed for inspecting crystallinity characteristics of the NWs. The NWs geometry was determined by FEI XL30 SFEG scanning electron microscope (SEM) from top view and tilted view (30°). High-resolution transmission electron microscope (HRTEM) images were taken in a JEOL-JEM 2100 microscope working at 200 kV to further investigating the crystalline properties of individual NWs. Focused ion beam (FIB) specimens were prepared using a JIB4500 for HRTEM measurements. Energy-dispersive X-ray spectroscopy (EDX) measurements were also carried out with an Oxford Instrument X-MAX 80 to determine the elemental composition and fluctuation.

#### **5.4.2 Morphological and structural characteristics**

The success of core-shell NW structure was confirmed by SEM measurements as illustrated in Fig 5.7 a, b for their top and tilted view respectively. It can be seen that the core-shell NWs exhibit a uniform diameter along entire length (e.g. non-tapering). The density of the NWs is  $13.3\pm 1.1\times 10^8\text{ cm}^{-2}$ , which is relatively high. Further statistical analysis over the whole sample surface area gives the average NWs length of  $2.1\pm 1.0\text{ }\mu\text{m}$ , the average NW diameter of  $75\pm 15\text{ nm}$  and core width  $\sim 35\text{ nm}$  (as depicted in Figure 5.7(d)-(e)). The SEM images also reveal a mixture of bent ( $\sim 80\%$ ) with shell thickness 11.8 nm and vertically oriented ( $\sim 20\%$ ) core-shell NWs with shell thickness 6.22 nm. This is very different from the bare InAs NWs, which are vertically oriented

[16],(see Figs 5.2&5.3). We believe this high percentage of bent NWs is associated with the asymmetric strain distribution around the NWs due to the non-uniform thickness of the AlSb shell layer around the core NW. This assumption is verified by high-resolution transmission electron microscopy (HRTEM) studies and energy- dispersive X-ray spectroscopy (EDX) analysis. The success of the deposition of AlSb shell layer on the core InAs NW is confirmed by X-ray diffraction scan (see Fig 5.8). The diffraction peak centered at  $51.41^\circ$  is associated with the diffraction from AlSb (222). It should be noted that several diffraction peaks also present in the scan implying the mixture of zinc-blende (ZB) and wurtzite (WZ) phases in the core InAs, which is consistent with previous report [14].

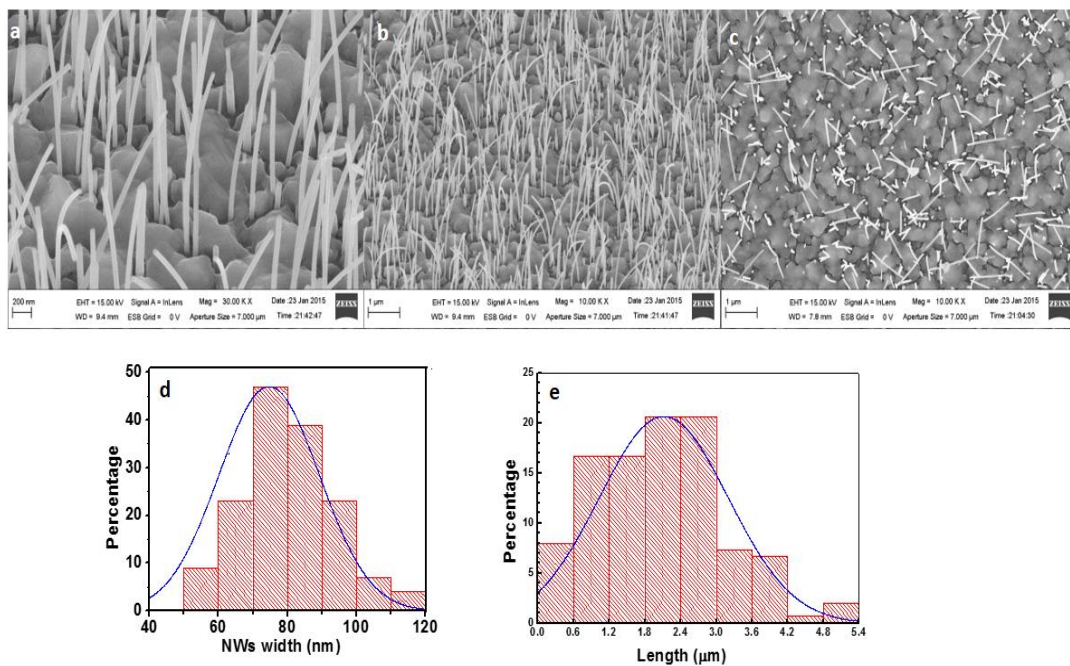


Figure 5.7: 30° tilted SEM images of InAs/AlSb core shell NWs a) 30° tilt at 30k magnification b) 30° tilt at 15k magnification. c) Top view at 0°. D) Histogram statistics of NWs diameter. e) Length.

Two additional peaks associated with (220) and (311) are also present, these are due to the bend of the NWs. More importantly, a diffraction peak centred at  $51.410$  is present. This verified the successful growth of AlSb (222) shell layer around the core InAs NWs.

(EDX) analysis. Figures 5.9 (a - c) and (e-f) show low-resolution TEM images of a  
 The realization of the core-shell NW heterostructure was further confirmed by scanning

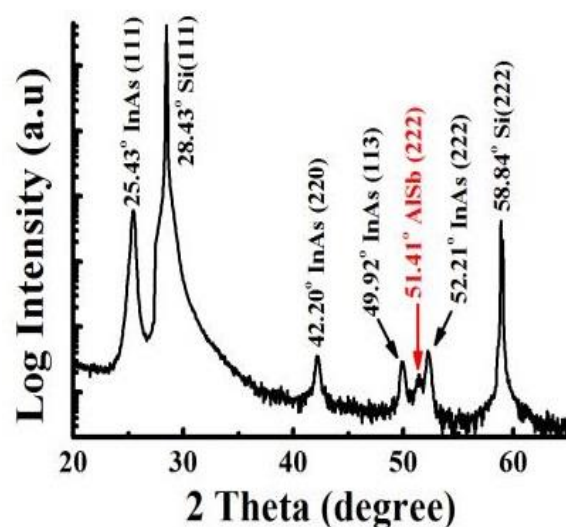


Figure 5.8: HRXRD diffraction patterns of InAs/AlSb NWs

transmission electron microscopy (STEM) and energy-dispersive X-ray spectroscopy typically bent and straight NW. Both NWs have an InAs core  $\sim 30 - 40$  nm diameter. The vertically oriented NWs have a uniform shell thickness ( $<10$  nm) as shown in Fig 5.9 (b,c). Conversely, the bent NW has an asymmetric shell (Figure 5.9 (f, g)), i.e. the AlSb shell thickness is uneven around the InAs core. This asymmetric shell thickness exerts a non-uniform stress on the core. In this InAs/AlSb core-shell structure, the core is in tensile strain of  $\sim 1.2\%$  with respect to the AlSb shell. Although this strain is small, it is still capable to bend the NWs due to the large NW length and the thin diameter. is in tensile strain of  $\sim 1.2\%$  with respect to the AlSb shell. Although this strain is small, it is still capable to bend the NWs due to the large NW length and the thin diameter. It should be noticed that no dislocations are seen in the AlSb shell, indicating that it is coherently strained to the core. This may reflect the difficulty of nucleating dislocations of appropriate Burgers vectors [17] to relieve interfacial strain in this NW geometry. Higher critical thickness has been theoretically predicted for NW geometry compared

with the corresponding thin film systems [1, 17, 18]. Because the total strain energy of the core-shell, system is lower than that of thin film with equivalent thickness of the

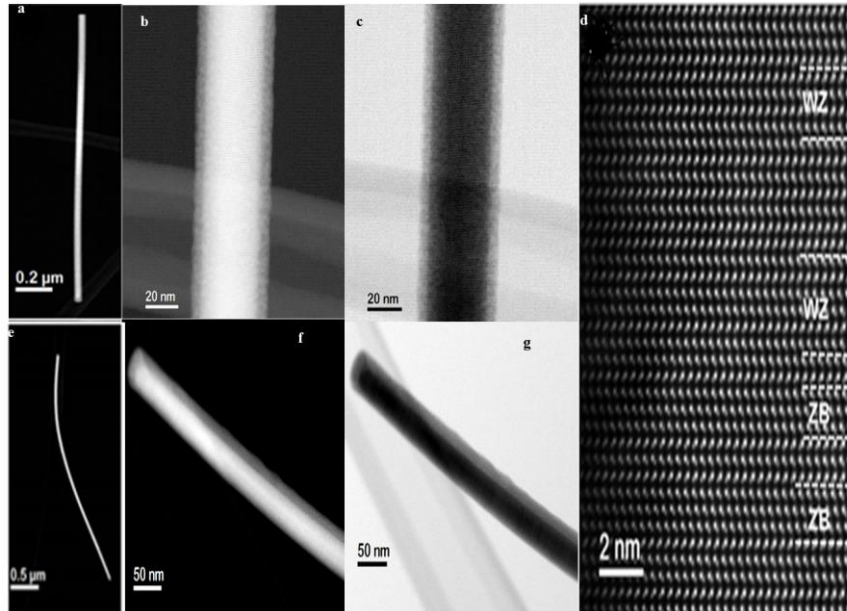


Figure 5.9: Low-magnification ADF-STEM images from a straight NW (a-c) and a bent NW (e-g) is a higher magnification STEM image of the straight NW showing core-shell structure with uniform shell thickness. (e-g) shows a bent NW with an asymmetric AlSb shell. High magnification annular dark-field image of the shell/core interface showing a mixture of WZ and ZB phases (d).

shell. This allows for higher value of critical thickness when growing core-shell structure. Additionally, the large area-to-volume ratio of NW geometry provides more flexible strain relaxation mechanisms, rather than the formation of interfacial dislocations. Different structures associated with strain relaxation in NWs have been reported including quantum dot [19], uneven thickness growth [20] and bending [21]. Although the origin of the uneven coating of the core NW remains unclear, one of the reasons could be associated with the accumulated strain induced from the deposition of the shell layer. Such strain in NW structures could lead to uneven deposition during the growth. Therefore, one of the advantages of using core/shell vs planar configurations is

that higher elastic strain is allowed, enabling higher coherent strains in the NW configuration detailed structural information of the core-shell NWs was obtained using annular dark field (ADF) and bright field (BF) STEM. Figure 5.9d shows a  $\langle 110 \rangle$  zone axis ADF-STEM image of the shell/core interface. The growth direction is vertical. Alternating WZ and ZB phases are clearly visible. The fraction of WZ phase was found to be  $\sim 50\%$ , calculated by analyzing multiple NWs (following the metrics proposed by Caroff et al [13], a segment must contain at least four monolayers of a given stacking sequence to be considered as a specific crystal phase). Many rotational twin-planes (TPs) were also observed. These observations are typical for InAs NWs [22-24]. Thus, electron microscopy analysis demonstrates high quality InAs/AlSb core-shell NWs accommodating strain without generation of dislocations. It should be noted that the core-shell structure in the NW is further confirmed by elemental analysis. An EDX composition profile across a straight NW, along a line perpendicular to the growth direction, is shown in Fig 5.10 (a). A core-shell structure is clearly visible in the line plot of composition (normalized to 100 at %). These data are consistent with the projection of a core-shell structure with abrupt interface as shown in Fig 5.11b. This schematic corresponds to the projected thickness (and hence X-ray signal) from a circular NW with a  $\sim 20$  nm radius core and a  $\sim 5$  nm-thick shell. Figs 5.10(b) and (c) show the top view ADF and BF TEM images of a quasi-straight NW respectively. The core-shell NW enclosed with six facets, which is quite different with InAs/GaSb case that multiple side facets dominate during the growth process [25]. It should be noted that oxygen is observed in the shell layer. The dark/bright contrast in the ADF and BF images implies the compositional changes in the shell of the NW due to the oxidation of AlSb shell layer. Corresponds to the projected thickness (and hence X-ray

signal) from a circular NW with a  $\sim 20$  nm radius core and a  $\sim 5$  nm-thick shell. Figs 5.10(b) and (c) show the top view ADF and BF TEM images of a quasi-straight NW

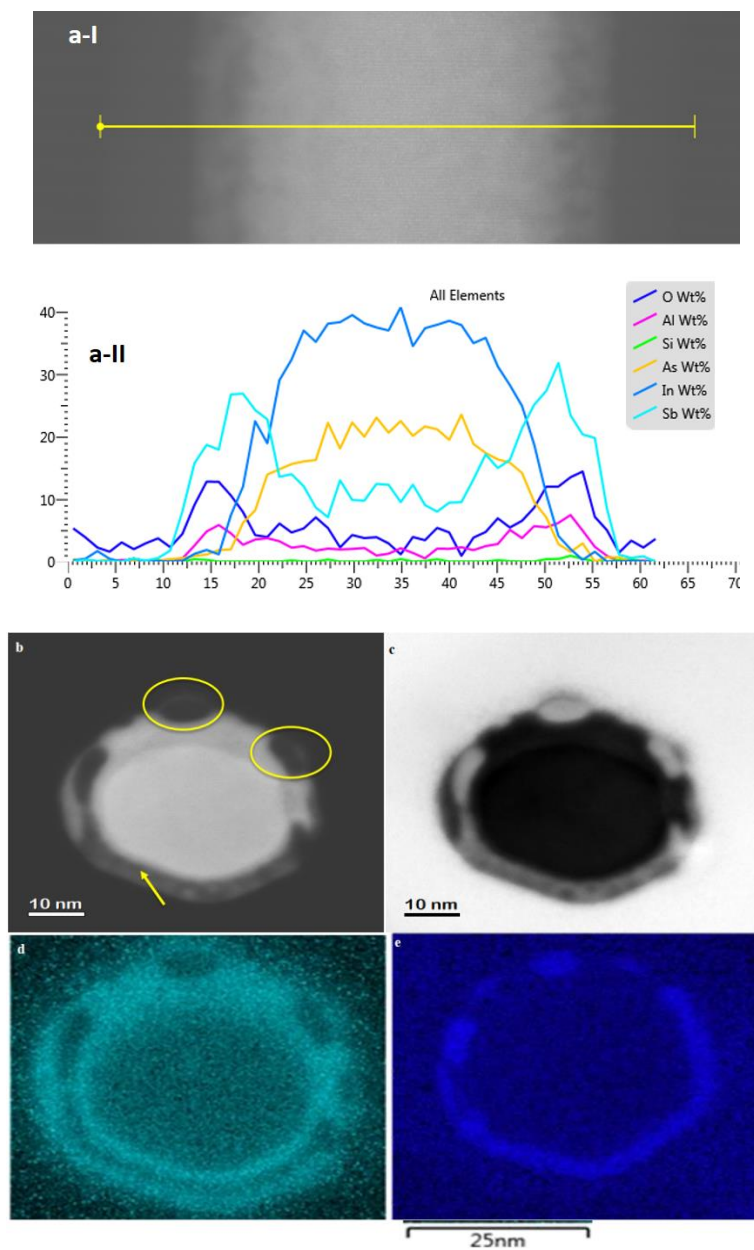


Figure 5.10 EDX composition profile of In, As, Al, Sb, and O element profile across a quasi-straight core-shell NW (a), (a-I) shows the measurement path across the NW. Top view ADF TEM image (b) and BF TEM image (c) of a quasi-straight core-shell NW. The yellow ellipses in (b) indicates the areas are rich in Al and O; the yellow arrow indicates the area consists of a region rich in Al and O between two Sb rich bands. The Sb (d) and Oxide distribution (e) profile across a core-shell NW.

respectively. The core-shell NW enclosed with six [26] facets, which is quite different with InAs/GaSb case that multiple side facets dominate during the growth process. It should be noted that oxygen is observed in the shell layer.

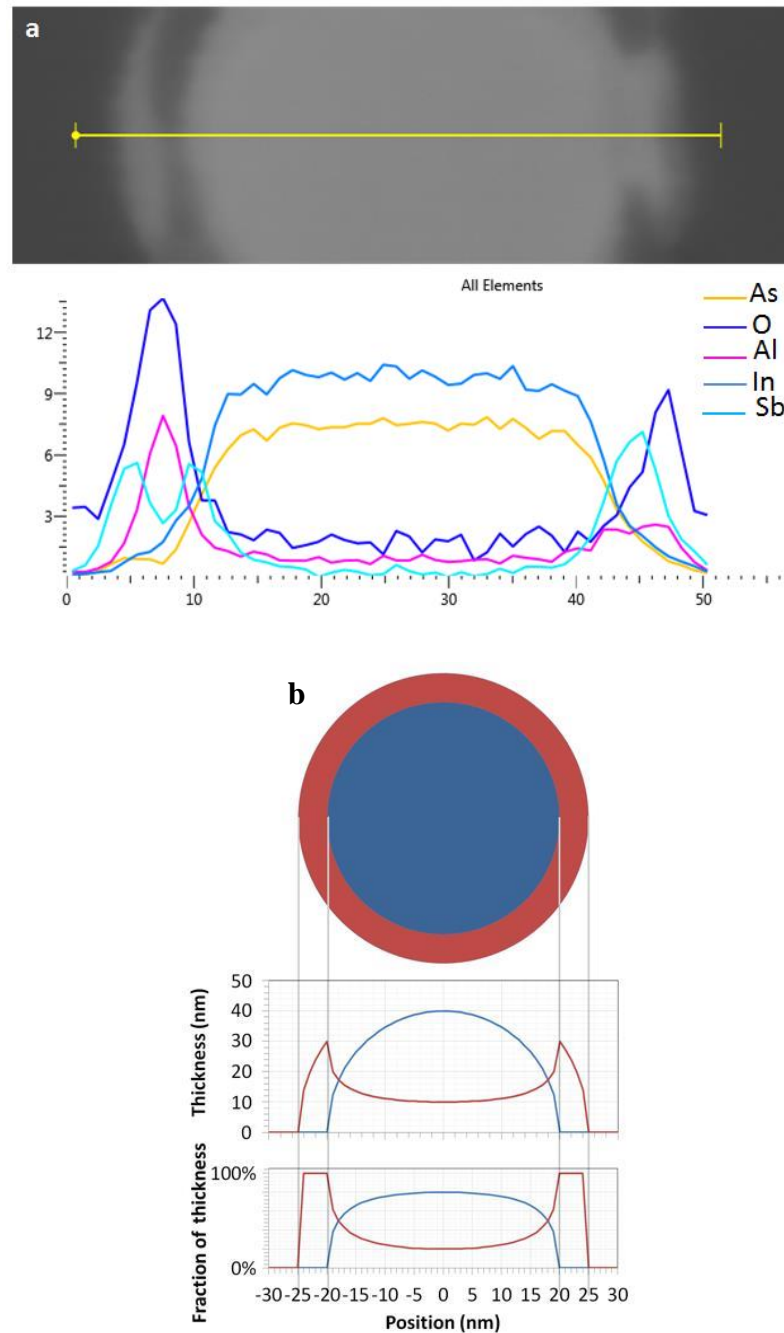


Figure 5.11 a) EDX profile clearly reveals this higher concentration of Al/O between two areas of higher concentration of Sb on the shell (left part). b) Projection schematic of a core-shell structure with abrupt interface.

The dark/bright contrast in the ADF and BF images implies the compositional changes in the shell of the NW due to the oxidation of AlSb shell layer.

These oxygen rich regions are very likely due to the high affinity of AlSb for oxygen that makes it highly susceptible to oxidation. It is worth noting that the oxidation of the shell layer is not uniform. Two types of oxidization areas can be observed. (i) Vertexes of the hexagonal prism rich in Al and O, indicated by the yellow ellipses in Figure 5.10(b); (ii) Al and O rich region between two rich Sb bands, indicated by the yellow arrow in Fig 5.10(b), Fig 5.10 d,e correspond to Sb and O elemental map distributions, respectively. O rich region around the vertexes are clearly observed (Fig 5.10d), and the O rich band sandwiched between two thin Sb rich bands (Fig 5.10e). The vertexes region has large area exposed to oxygen, it is understandable it is more readily to be oxidized; however, the reason for the formation of the Al and O rich band in the shell layer is unclear.

## **5.5 InAs/GaSb NWs**

### **5.5.1 Epitaxial growth details**

Sample of InAs/GaSb core-shell NWs was grown on Si (111) substrate. The NW has i-n structure. The pre-growth procedure is similar to that of InAs/AlSb NWs but the growth conditions are different, As<sub>4</sub> beam equivalent pressure (BEP) is  $3 \times 10^{-6}$  mbar, and an InAs nominal growth rate of 0.1  $\mu\text{m/h}$ . The InAs NWs growth lasted for 90 minutes at 460 °C and was followed by 1-hour deposition of GaSb shells at reduced growth temperature and a low growth rate.

## 5.5.2 Morphological and structural characteristics

SEM images of the samples as depicted in Fig (5.10) reveals that there are two different area in the sample; the first is of high density with coalescent NWs which feature with an average diameter of  $241.2 \pm 31.7$  nm, length of  $2.0 \pm 1.0$   $\mu\text{m}$  with a density of  $7.0 \times 10^8$   $\text{cm}^{-2}$  as shown in Fig (5.12a,b). The other region is of lower density of  $1.43 \text{cm}^{-2}$  with similar length and diameter (See Fig 5.12a). Although the NW always has a hexagonal cross section, it has a tapered top with a larger diameter than at the main part of NW, as shown in Fig 5.12. Meanwhile, the shell exhibits a so-called saw-tooth shape as indicated with red square in figure (5.12b).

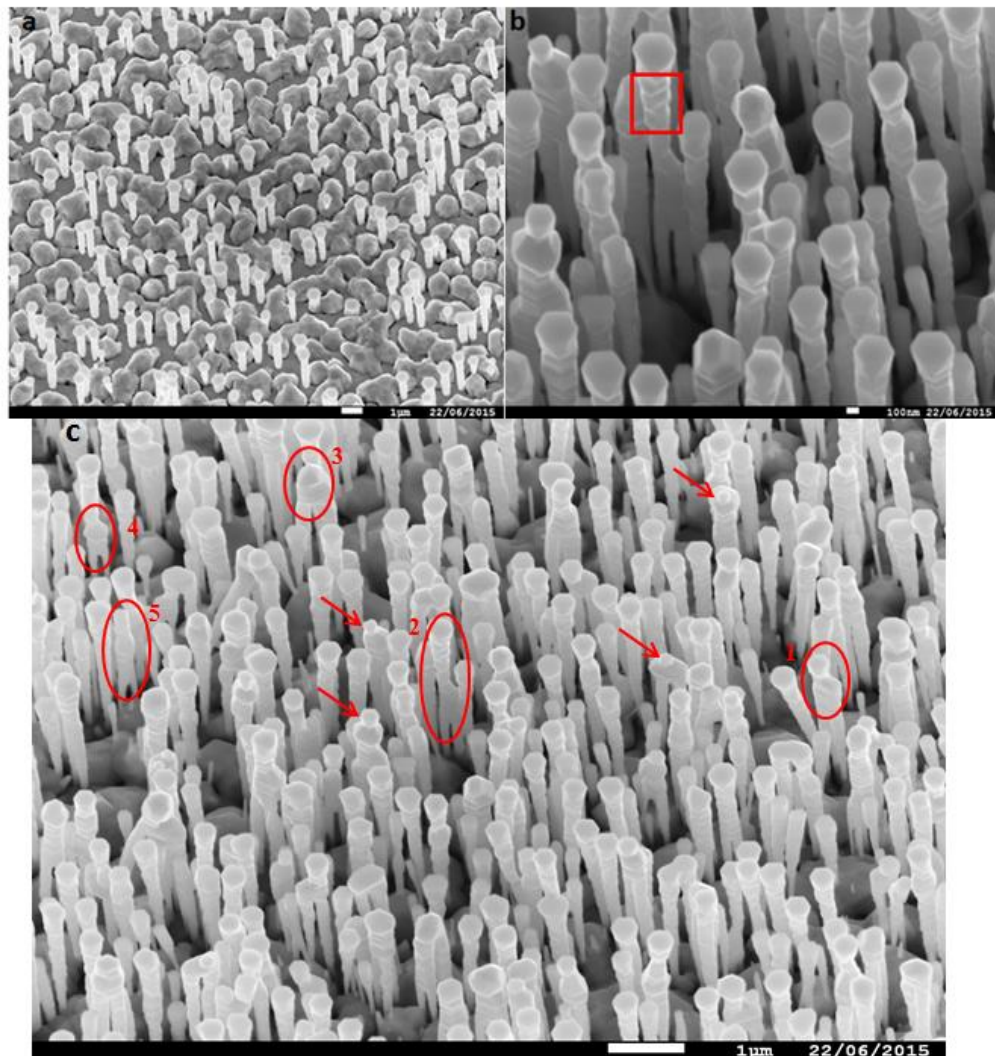


Figure 5.12:  $30^\circ$  tilted SEM image of InAs/GaSb core-shell NWs

This can be related with the 30-degree rotation of the phases between the core and the shell. This is associated to a transferring of crystal direction from  $\langle 111 \rangle_A$  to  $\langle 111 \rangle_B$  resulted from the twinning of  $\langle 111 \rangle_A$ . This twisting in direction occurs due to the fast growth rate in the  $\langle 111 \rangle_A$  direction in comparison with  $\langle 111 \rangle_B$  [27]. A. Dick et al [28] pointed out that when ZB exhibited at high growth temperature above 400 °C and relatively large diameter, the NW adopts periodically twinned morphology with segment bounded by (111) type facets. This finding is consistent with our growth conditions, i.e. 460 °C of growth temperature and a large  $D_{NW}$  of  $241.2 \pm 31.7$  nm. Based on above, we assume our NWs most likely have ZB structure. This is confirmed as well by x-ray diffraction depicted in Fig (5.13). It can be noticed that there is no obvious angle for InAs. This is might be due to considerably thick shell layer  $59.7 \pm 14.7$  which prevents x-ray from penetrating into the core. Both (111) and (222) directions are associated with pure ZB GaSb without any presence of WZ segment.

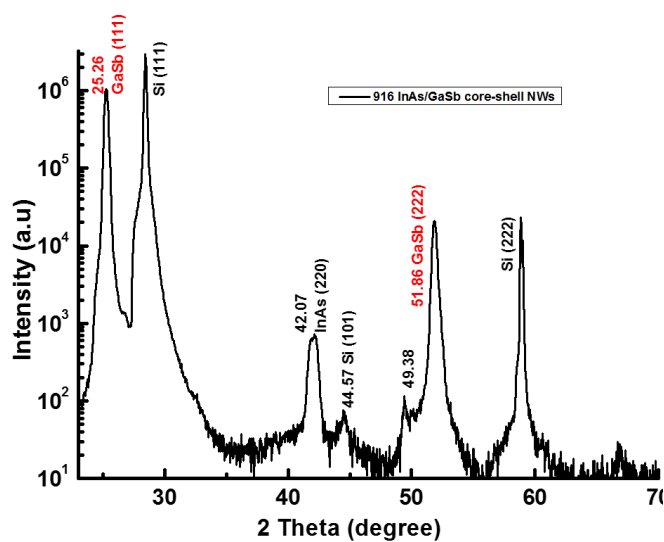


Figure 5.13: XRD of InAs/GaSb core-shell NWs indicating ZB structure.

This is well agreed with the theory saying that high-energy difference between WZ and ZB crystal structure of GaSb making it favor ZB structure [29]. The top of the NWs also features with a flat platform with diameter wider than the main part of the NW.

This could be correlated with increased growth rate on the top owing to the additional direct impinging atoms in comparison with the growth in the bottom part. Because low growth temperature was used for the growth of the shell, it decreases the diffusion ability of reactant atoms hence the direct impingement will be the dominant contribution to the growth of the shell [30]. Another reason of forming platform at the top of the NW is due to the radial growth of the shell. since relatively long growth time increased the NW diameter at the upper part. GaAs/GaSb core-shell NWs [30] , GaInSb diamond shape segment [31] , InSb nanotubes [32] based on radial overgrowth have also reported.

To confirm the construction of core-shell structure and composition, Transmission Electron Microscopy (TEM) and Energy Dispersive X-ray (EDX) were used to examine the NWs. Figs 5.14 and 5.15 show an EDX profile confirming the core-shell structure with InAs core and GaSb shell. The core diameter and the shell thickness were determined to be  $167.3 \pm 14.5$  nm and  $59.7 \pm 14.7$  nm, respectively. It is worth noting that no misfit dislocations were observed along the interface of core InAs and the GaSb shell. This is due to the very low lattice mismatch between them (0.6%). The bottom of the NWs is thinner than its top which is about 165.1 nm as shown in Fig 5.12a, b. This is because the shell at the upper part of the NW is thicker than that at the bottom. Figs (5.15a, b) confirm that there is a thin shell in the bottom of the NWs. This proves that the smaller diameter at the end of the NW is not because of the absence of shell as assumed in Ref [25]. The NWs also featured with merged structure. Some NWs merge from the middle part and have different lengths without affecting the seed particles on their tops as indicated in red circles and numbered 1 and 2 in Fig (5.12c). This is attributed to the In droplets, which make them grow separately but they merge during the growing of shell. However, other NWs have equivalent length but they meet from

the top part of the NWs. This behavior could be occurred during growth where In droplets merged then continued to be one NW [33] as shown in red circles 3, 4 and 5 in Fig5.12c. There are some NWs with unwrapped core at the top of the NWs as indicated in red arrows in Fig 5.12. More structure investigated is required in this regard.

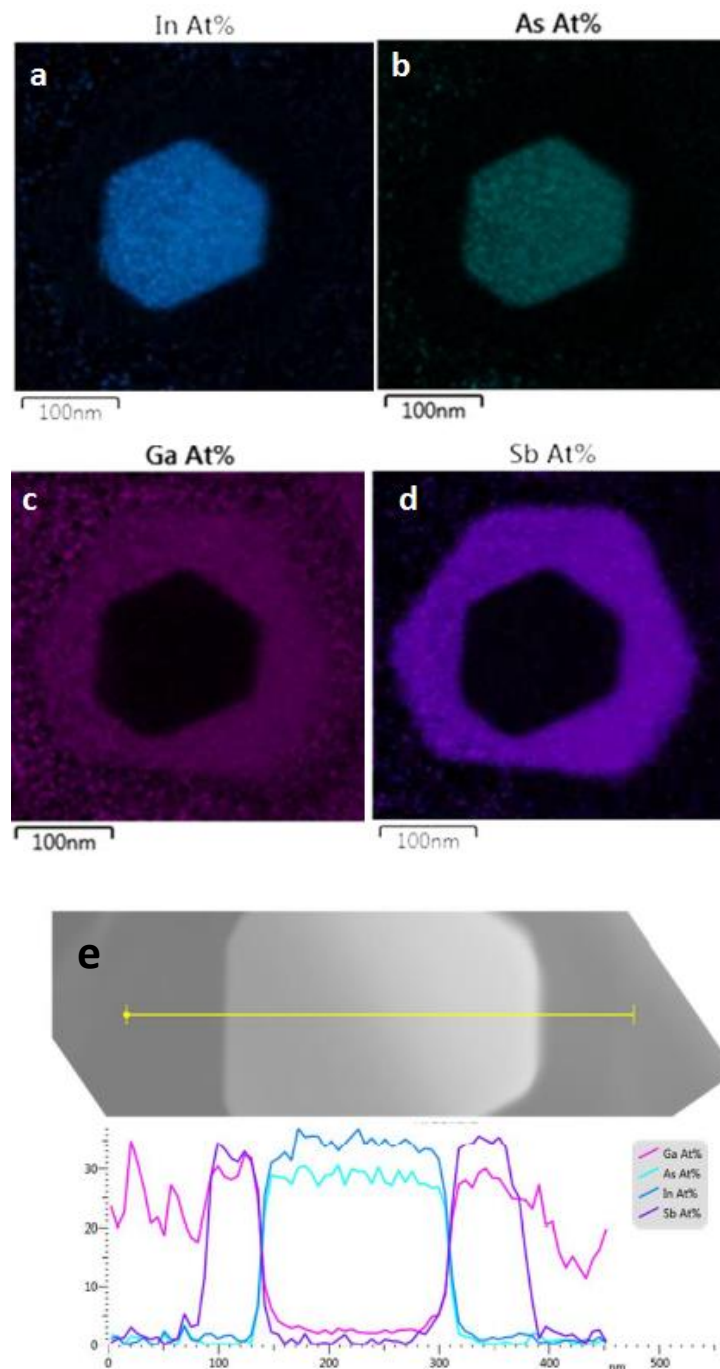


Figure (5.14) EDX profile of InAsSb/GaSb (a-d). Composition of core-shell NW (g). STEM-BF and ADF confirm the core-shell structure at the bottom of the NWs (f,g) and reveal that the shell in the bottom part is thinner than the top (h,i).

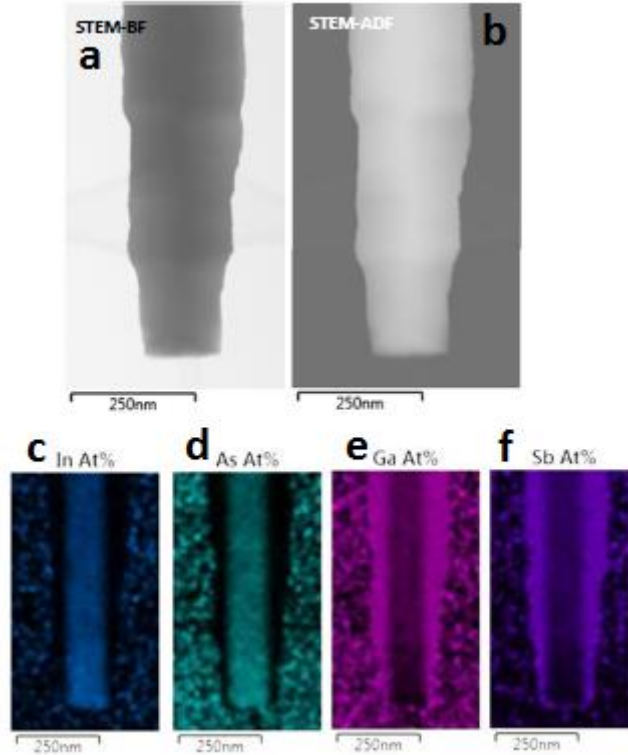


Figure (5.15) EDX profile of InAsSb/GaSb a,b)STEM-BF and ADF confirm the core-shell structure at the bottom of the NWs and reveal that the shell in the bottom part is thinner than the top.

## 5.6 Summary

We optimised the epitaxial growth for bare InAs NWs, InAsSb NWs and successfully obtained two different structures of core-shell NWs. The new growth method improved NWs properties in terms of crystal structure and optical properties which confirmed by X-ray diffraction. Two structure of core-shell NWs were grown; InAs/AlSb and InAs/GaSb. Both of these core-shell nanowires are dislocation-free with small chemical intermixing at the interfaces. The NWs of InAs/AlSb were long with relatively thin diameter for both core and shell. SEM revealed two type morphology of the NWs of this structure; vertically aligned and bent the reason of bent NWs was the asymmetric shell layer. The X-ray scans revealed a small angle of the thin shell sample has two morphologies; vertically aligned and bent. The reason of the bending was attributed to

the asymmetric shell. X-ray diffraction showed a small angle of AlSb shell. HRTEM confirmed the core-shell structure with presence of oxidation due to Al presence.

InAs/GaSb exhibited a very thick core and shell comparing to that of InAs/AlSb. It also showed zig-zag morphology or what is called (saw-tooth). This was associated with the growth direction rotation by 30-degree. The top of the NWs has platform with hexagonal cross-section with diameter wider than that of the long part under the top. The reason of wider top is due to high growth rate induced by direct impingement growth, which in turn causes increasing the radial growth at the top part more than that in the bottom of the NWs.

## References

- [1] C. M. Haapamaki, J. Baugh, and R. Lapierre, "Critical shell thickness for InAs-AlxIn1-xAs(P) core-shell nanowires," *Journal Of Applied Physics*, vol. 112, no. 12, pp.124305,2012.
- [2] C. K. Yong, K. Noori, Q. Gao, H. J. Joyce, H. H. Tan, C. Jagadish, F. Giustino, M. B. Johnston, and L. M. Herz, "Strong carrier lifetime enhancement in GaAs nanowires coated with semiconducting polymer," *Nano letters*, vol. 12, no. 12, pp. 6293, 2012.
- [3] X. Wang, Y. Hu, L. Song, W. Xing, H. Lu, P. Lv, and G. Jie, "Effect of antimony doped tin oxide on behaviors of waterborne polyurethane acrylate nanocomposite coatings," *Surface and Coatings Technology*, vol. 205, no. 7, pp. 1864-1869, 2010.
- [4] Y. Li, J. Xiang, F. Qian, S. Gradecak, Y. Wu, H. Yan, D. A. Blom, and C. M. Lieber, "Dopant-free GaN/ AlN/ AlGaIn radial nanowire heterostructures as high electron mobility transistors," *Nano letters*, vol. 6, no. 7, pp. 1468, 2006.
- [5] X. Meng, H. Peng, Y. Gai, and J. Li, "Influence of ZnS and MgO Shell on the Photoluminescence Properties of ZnO Core/ Shell Nanowires," *Journal of Physical Chemistry C*, vol. 114, no. 3, pp. 1467-1471, 2010.
- [6] X. Jiang, Q. Xiong, S. Nam, F. Qian, Y. Li, and C. M. Lieber, "InAs/ InP radial nanowire heterostructures as high electron mobility devices," *Nano letters*, vol. 7, no. 10, pp. 3214, 2007.
- [7] Z. Wang, Y. Fan, and M. Zhao, "Natural charge spatial separation and quantum confinement of ZnO/ GaN- core/ shell nanowires," *Journal of Applied Physics*, vol. 108, no. 12, pp.123707,2010.
- [8] F. Fabbri, F. Rossi, G. Attolini, G. Salviati, S. Iannotta, L. Aversa, R. Verucchi, M. Nardi, N. Fukata, B. Dierre, and T. Sekiguchi, "Enhancement of the core near-band-edge emission induced by an amorphous shell in coaxial one-dimensional nanostructure: the case of Si/SiO<sub>2</sub> core/shell self-organized nanowires," *Nanotechnology*, vol. 21, no. 34, pp. 345702, 2010.
- [9] E. A. Anyebe, Q. Zhuang, A. M. Sanchez, S. Lawson, A. J. Robson, L. Ponomarenko, A. Zhukov, and O. Kolosov, "Self-catalysed growth of InAs nanowires on bare Si substrates by droplet epitaxy," *physica status solidi (RRL) – Rapid Research Letters*, vol. 8, no. 7, pp. 658-662, 2014.
- [10] V. G. Dubrovskii, and N. V. Sibirev, "Growth rate of a crystal facet of arbitrary size and growth kinetics of vertical nanowires," *Physical Review E*, vol. 70, no. 3, pp. 031604, 2004.

- [11] Q. Zhuang, E. Anyebe, A. M. Sanches, S. Lawso, A. J. Robson, L. Ponomaren, A. Zhukov and O. Kolosov, “Self-catalysed growth of InAs nanowires on bare Si substrates by droplet epitaxy,” *physica status solidi (RRL) - Rapid Research Letter*, vol. 8, no. 7, pp. 658–662, 2014.
- [12] E. Anyebe, “Influence of growth parameters on In- droplet- assisted growth of InAs nanowires on silicon,” *Applied Nanoscience*, vol. 7, no. 7, pp. 365-370, 2017.
- [13] P. Caroff, K. A. Dick, J. Johansson, M. E. Messing, K. Deppert, and L. Samuelson, “Controlled polytypic and twin- plane superlattices in III– V nanowires,” *Nature Nanotechnology*, vol. 4, no. 1, pp. 50, 2008.
- [14] E. Anyebe, Q. D. Zhuang, R. Chen, H. Liu, Ana M. Sanchez, Mohana K. Rajpalke, and Z. M. W. Tim D. Veal, , Y. Z. Huang, and H. D. Sun, “Sb-Induced Phase Control of InAsSb Nanowires Grown by Molecular Beam Epitaxy,” *Nano Letters*, vol. 15, pp. 1109–1116, 2015.
- [15] E. Anyebe, M. Rajpalke, T. Veal, C. Jin, Z. Wang, and Q. Zhuang, “Surfactant effect of antimony addition to the morphology of self- catalyzed InAs<sub>1-x</sub>Sb<sub>x</sub> nanowires,” *Nano Research*, vol. 8, no. 4, pp. 1309-1319, 2015.
- [16] H. Li, H. Alradhi, Z. Jin, E. A. Anyebe, A. M. Sanchez, W. M. Linhart, R. Kudrawiec, H. Fang, Z. Wang, W. Hu, and Q. Zhuang, “Novel Type- II InAs/ AlSb Core – Shell Nanowires and Their Enhanced Negative Photocurrent for Efficient Photodetection,” *Advanced Functional Materials*, vol. 28, no. 8, pp. 1705382, 2018.
- [17] S. Raychaudhuri, and E. T. Yu, “Critical dimensions in coherently strained coaxial nanowire heterostructures,” *Journal of Applied Physics*, vol. 99, no. 11, pp. 114308 , 2006.
- [18] T. E. Trammell, X. Zhang, Y. Li, L.-Q. Chen, and E. C. Dickey, “Equilibrium strain- energy analysis of coherently strained core– shell nanowires,” *Journal of Crystal Growth*, vol. 310, no. 12, pp. 3084-3092, 2008.
- [19] M. Heiss, Y. Fontana, A. Gustafsson, G. Wüst, C. Magen, D. D. O’regan, J. W. Luo, B. Ketterer, S. Conesa-Boj, A. V. Kuhlmann, J. Houel, E. Russo-Averchi, J. R. Morante, M. Cantoni, N. Marzari, J. Arbiol, A. Zunger, R. J. Warburton, and A. F. I. Morral, “Self- assembled quantum dots in a nanowire system for quantum photonics,” *Nature Materials*, vol. 12, no. 5, pp. 439, 2013.
- [20] R. B. Lewis, L. Nicolai, H. Küpers, M. Ramsteiner, A. Trampert, and L. Geelhaar, “Anomalous Strain Relaxation in Core- Shell Nanowire Heterostructures via Simultaneous Coherent and Incoherent Growth,” *Nano letters*, vol. 17, no. 1, pp. 136, 2017.

- [21] J. Wallentin, D. Jacobsson, M. Osterhoff, M. T. Borgström, and T. Salditt, "Bending and Twisting Lattice Tilt in Strained Core-Shell Nanowires Revealed by Nanofocused X-ray Diffraction," *Nano Letters*, vol. 17, no. 7, pp. 4143-4150, 2017.
- [22] E. Dimakis, J. Lahnemann, U. Jahn, S. Breuer, M. Hilse, L. Geelhaar, and H. Riechert, "Self-Assisted Nucleation and Vapor-Solid Growth of InAs Nanowires on Bare Si(111)," *Crystal Growth and Design*, vol. 11, no. 9, pp. 4001-4008, 2011.
- [23] Y. Jing, X. Bao, W. Wei, C. Li, K. Sun, D. Aplin, Y. Ding, Z. Wang, Y. Bando, and D. L. Wang, "Catalyst-Free Heteroepitaxial MOCVD Growth of InAs Nanowires on Si Substrates," *J. Phys. Chem. C*, vol. 118, no. 3, pp. 1696-1705, 2014.
- [24] W. Wei, X.-Y. Bao, C. Soci, Y. Ding, Z.-L. Wang, and D. Wang, "Direct heteroepitaxy of vertical InAs nanowires on Si substrates for broad band photovoltaics and photodetection," *Nano letters*, vol. 9, no. 8, pp. 2926, 2009.
- [25] T. Rieger, D. Grtzmacher, and M. I. Lepsa, "Misfit dislocation free InAs/GaSb coreshell nanowires grown by molecular beam epitaxy," *Nanoscale*, vol. 7, no. 1, pp. 356-364, 2014.
- [26] X. Wang, Y. Hu, L. Song, W. Xing, H. Lu, P. Lv, and G. Jie, "Effect of antimony doped tin oxide on behaviors of waterborne polyurethane acrylate nanocomposite coatings," *Surface and Coatings Technology*, vol. 205, no. 7, pp. 1864-1869, 2010.
- [27] T. Burgess, S. Breuer, P. Caroff, J. Wong-Leung, Q. Gao, H. Hoe Tan, and C. Jagadish, "Twinning superlattice formation in GaAs nanowires," *ACS nano*, vol. 7, no. 9, pp. 8105, 2013.
- [28] F. Glas, M. Ramdani, G. Patriarche, and J. Harmand, "Predictive modeling of self-catalyzed III-V nanowire growth," *Physical Review B*, vol. 88, no. 19, 2013.
- [29] T. Akiyama, K. Sano, K. Nakamura, and T. Ito, "An empirical potential approach to wurtzite-zinc-blende polytypism in group iii-v semiconductor nanowires," *Japanese Journal of Applied Physics*, vol. 45, no. 3L, pp. 275, 2006.
- [30] S. Shi, Z. Zhang, Z. Lu, H. Shu, P. Chen, N. Li, J. Zou, and W. Lu, "Evolution of morphology and microstructure of GaAs/GaSb nanowire heterostructures," *Nanoscale Research Letters*, vol. 10, no. 1, pp. 1-8, 2015.
- [31] S. Gorji Ghalamestani, B. Ganjipour, C. Thelander, J. Johansson, K. A. Dick, M. Ek, and P. Caroff, "Demonstration of defect-free and composition tunable Ga<sub>x</sub>In<sub>1-x</sub>Sb nanowires," *Nano Letters*, vol. 12, no. 9, pp. 4914-4919, 2012.

- [32] S. R. Plissard, D. R. Slapak, M. A. Verheijen, M. Hocevar, G. W. G. Immink, I. van Weperen, S. Nadj-Perge, S. M. Frolov, L. P. Kouwenhoven, and E. P. A. M. Bakkers, "From InSb nanowires to nanocubes: looking for the sweet spot," *Nano letters*, vol. 12, no. 4, pp. 1794, , 2012.
- [33] B. Mandl, A. W. Dey, J. Stangl, M. Cantoro, L.-E. Wernersson, G. Bauer, L. Samuelson, K. Deppert, and C. Thelander, "Self-seeded, position-controlled InAs nanowire growth on Si: A growth parameter study," *Journal of Crystal Growth*, vol. 334, no. 1, pp. 51-56, 2011.

# Chapter 6

## Photoluminescence Studies of NWs

### 6.1 Introduction

Optical properties and carrier recombination mechanisms is crucial for examining the suitability specific structure and material for device applications. Photoluminescence (PL) is a useful tool that facilitates sample analysis related to optical properties. For example, it can shed light on radiative recombination efficiency, quenching of emission and defects in materials. To be more specific, photoluminescence is a convenient technique for nondestructive characterization of many basic optical properties of nanowires. These include characterization of energy bandgaps and provide perspective to impurities and deep-level defects [1].

Considering the advantages of PL studies stated above, we have carried out a systematically optical characterization of InAs nanowires. Materials were grown for target structure, composition; PL is one of the techniques we used to examine the optical properties, feedback to optimise it further. In the first section of this chapter, we present PL details of bare InAs NWs that were grown by both the conventional growth method and by the modified one. In the second section, we present the effect of Sb incorporation on the modification of the crystal phase of NWs; we describe how it improves the optical properties of these NWs. In the third section, we present the impact of doping of Si substrate on the photoluminescence of InAs NWs in the temperature range from 8 K to room temperature. In the final section, we discuss the PL characteristics of core-

shell NWs and compare them with those of the optimal bare InAs NWs to demonstrate the surface passivation by the shell layer.

## 6.2 Optical properties of bare InAs NWs

The optical properties of as-grown InAs are depicted in Fig 6.1. The PL measurements for InAs samples were processed by using a diode laser emitting at 980 nm for excitation. The signal was collected and dispersed by a monochromator and detected by a cooled HgCdTe photodetector through a lock-in amplifier. The power density of the excitation is around  $20\text{Wcm}^{-2}$  (a laser power of 200mW with a laser spot of around  $1\text{mm}^2$ ). In addition, an infrared modulated PL method based on a step scan Fourier transform infrared spectrometer (FTIR) was also used for detailed PL measurements such as temperature dependent and excitation-dependent scans[2].

Figure 6.1 shows low temperature (8K) PL spectra of two samples of bare InAs NWs (675 and 821) that grown by two different growth procedures with a reference of bulk InAs. The comparison of PL spectra of two samples of InAs NWs grown by conventional method sample 675 (red line) and the new developed growth technique, sample 821 [described in chapter five, section (5.2.4)], is shown in Fig 6.1a. Bulk InAs exhibits single peak at 0.412, which is associated with band-to-band (BtB) recombination. The emission intensity of sample 821 is improved dramatically by 5 times than that of sample 675. In addition, it shows a strong dominant peak (at  $\sim 0.413\text{eV}$ ). This peak is related to BtB similar to bulk InAs. This means that the quantum confinement has no significant contribution due to large diameter of the NWs ( $62.9\pm 15.0\text{nm}$ ) comparing to InAs Bohr radius ( $\sim 34\text{nm}$ ). The emission related to defects that was noticed in 675 (0.434 eV) is absent [3] in 821. Detailed analysis of each peak of the three samples (bulk InAs, 675 and 821) revealed that a spectral line width (full

width at half maximum, FWHM) of bulk InAs is 10 meV while it is 67 meV of sample 675 meV. That means it is 6 times wider than the peak width of bulk InAs. Interestingly, peak of sample 821 is 36 meV, which is closer to the bulk value. From all the above results, it can be said that InAs NWs show wide spectral line width comparing to the bulk InAs. M.H.Sun et al. reported weak, noisy and wide PL peaks in the range of (0.29-0.48 eV) from unpassivated InAs NWs, which correlated with the presence of surface states and poor crystalline quality. However, the relatively narrow FWHM of sample 821 can be related to the segments lengths changing, diameter of the NWs, and crystalline properties of the material, which revealed high optical quality. We believe this is because of the improved crystal structure. Thanks to the newly developed growth technique, defect free, single crystal NW lattice structure resulted for InAs nanowires.

PL curve of sample 675 that grown by conventional growth method is shown in Fig (6.1b). It is clear that InAs NWs show multipeak emission, which can be resolved into three peaks of emission: 0.434eV, 0.415eV and 0.389eV. The largest energy peak of 0.434 eV is attributed to the BtB transition formed by the WZ and ZB segment. The peak at 0.415 eV (indicating as number 1 in Fig 6.1b) is associated with WZ/ZB crystal phase mixture that exists in the NW. The mixture of WZ&ZB forms type II bandgap (see Fig 6.2), where electrons are confined in the ZB region while holes are localised in the WZ region [4]. The excited electrons transmit from the bottom of ZB conduction band to the top of the WZ valence band. As a result, radiative recombination occurred [5]. The third peak at ~ 0.389 eV is attributed to defect-related transition [6-9].

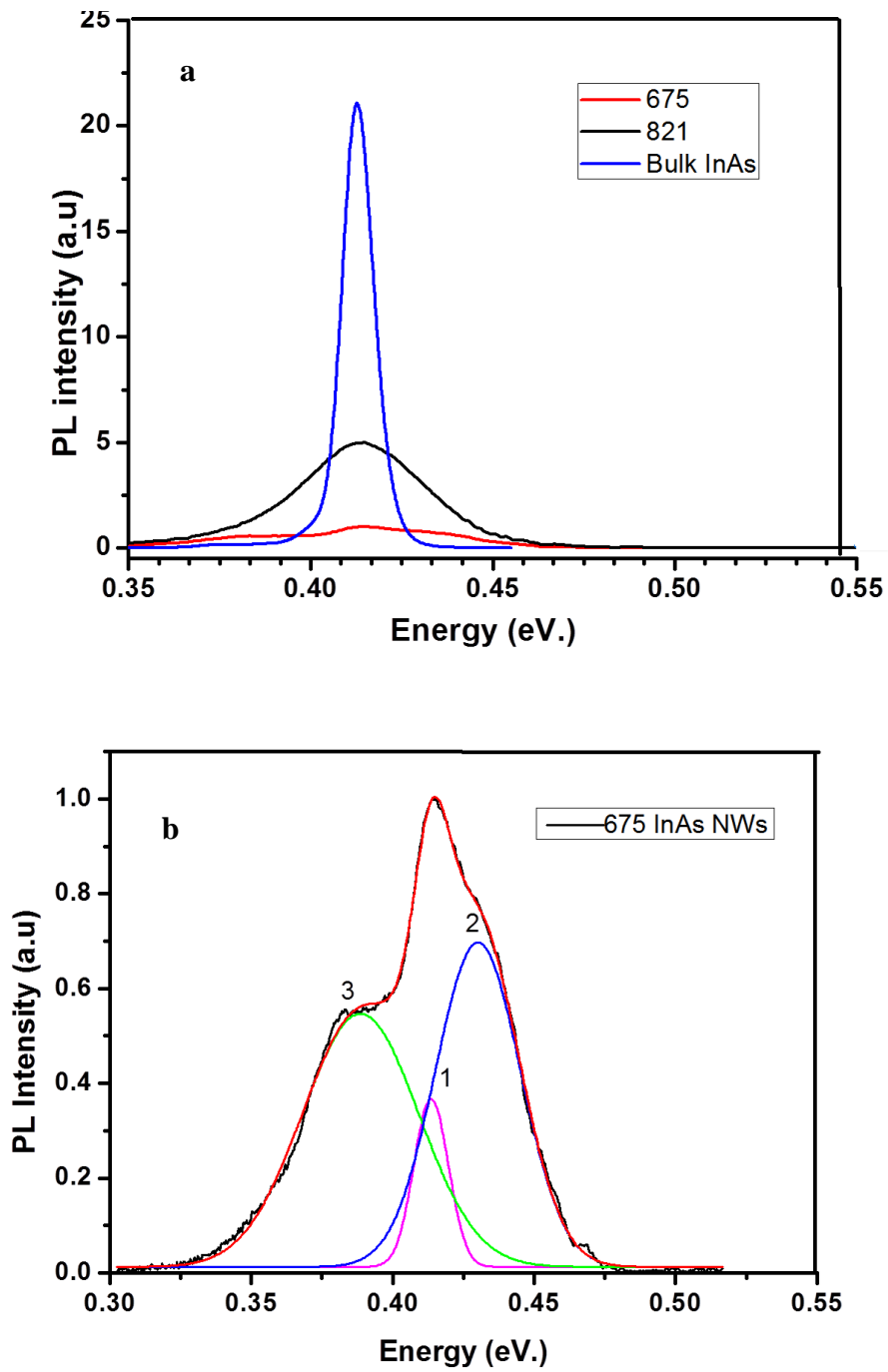


Figure 6.1: 8K PL of a) two samples of two samples of InAs NWs and bulk. b) Gaussian fitting PL of InAs NWs sample (675).

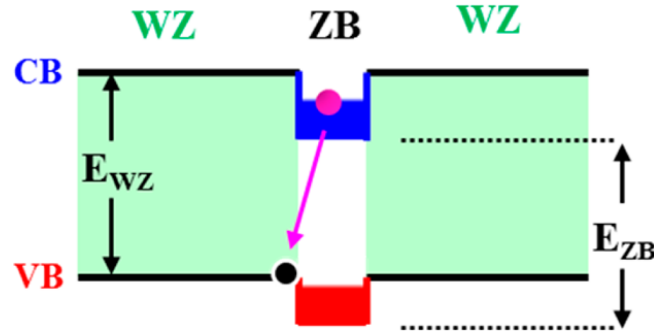


Figure 6.2: Schematic diagram of band alignment and recombination Processes for carriers transiting between valence band and conduction band in InAs NW containing mixture of WZ and ZB phases.

### 6.3 Low temperature (10 K) Photoluminescence of InAsSb nanowires:

InAsSb is known to have unique properties such as direct and widely tunable narrow bandgap energy (3-12  $\mu\text{m}$ ), high thermal conductivity, small electron effective mass, long carrier lifetime, and high electron mobility. Because of these, InAsSb NWs are ideal and versatile candidates for a variety of device applications in areas of optoelectronics. The InAsSb optical devices can operate in the infrared and terahertz spectral ranges.

Considering the importance of InAsSb nanowires articulated above, the PL measurements were performed on a series of as-grown InAsSb samples with an Sb content of up to 19%. Figure 6.3 depicts the evolution of the low-temperature (10 K) PL spectrum of InAsSb NWs with an increasing Sb composition. Based on the density of the NWs, we estimate that our PL measurement came from a contribution of around  $10^6$  NWs with a laser spot of  $1 \text{ mm}^2$ . Strong PL emission was observed for all the samples, and a long wavelength emission of up to  $5.1 \mu\text{m}$  was achieved. It should be noted that the detected PL emission of the samples is believed to originate from the NWs, although there were InAsSb clusters present on the Si surface. To verify that the emission was indeed from the NWs, we removed them using an ultrasonic bath, and

found that, no PL emission was detected from the samples. This implied that the emission took place from NWs. The failure in luminescence of the clusters is associated with their poor material quality, resulting from both the large lattice mismatch and antiphase domains.

In order to understand the optical properties of the samples, detailed analysis on the PL spectra was performed for each sample, apart from InAs sample (675 with 0% Sb) which has been discussed in the previous section (6.2).

Sample with 3% Sb has two peaks, (0.389 eV and 0.405 eV), see Fig 6.3b. The smaller energy peak (0.389eV.) which is present in the PL of sample 675, is still there. This is a defect related peak. Increasing Sb further 10%,16% and 19%, results in further reduction of the dominant emission peaked at 0.334, 0.304 and 0.242 eV respectively. Also the multi peak feature developed into single peak emission. It is noteworthy mentioning that the sample of 19% Sb composition gives wavelength of 5.1  $\mu\text{m}$ , which is the longest PL emission obtained up to date for InAsSb NWs. Regarding the peak linewidth, it has been noticed that PL peaks become wider with increasing Sb content. The details peak energy, FWHM for each sample are shown in table (6.1)

Table 6.1: Photoluminescence BtB related emission peak energy (measured at 10K) and the FWHM.

Sb composition %	PL Peak energy(eV.)	FWHM (meV.)
0	0.427	30
3	0.405	47.4
10	0.334	60
16	0.304	66.8
19	0.242	71.8

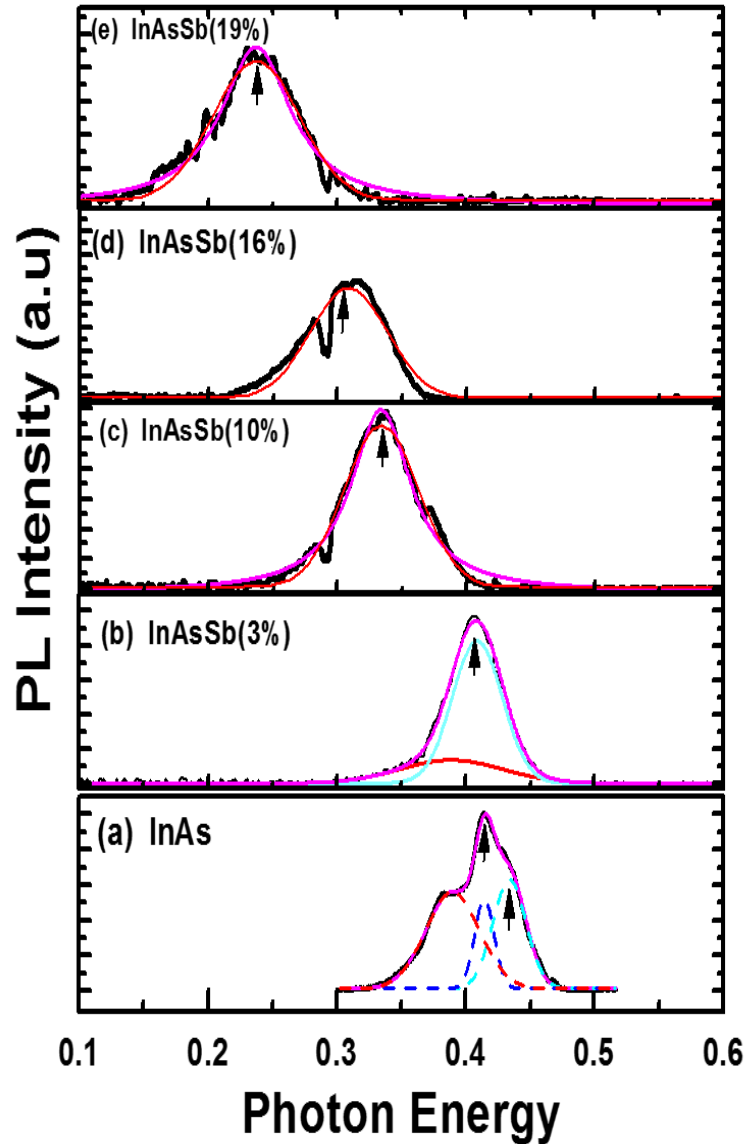


Figure 6.3: The evolution of 10 K PL of InAs NWs (a) and InAsSb NWs with and Sb composition of 3% (b), 10% (c), 16% (d) and 19% (e). The peaks in colours show the decomposed emissions.

Overall, there are several features can be seen in the NW PL spectra Fig 6.3. Firstly, by increasing the Sb content, the spectra turn from multi-peak emission in the InAs NW sample to single peak emission (at Sb content 10% and above). Secondly, the dominant peak of the samples shifts to lower energy with an increasing Sb content; and thirdly, the full width of half-maximum (FWHM) of the PL spectra tends to be broader for the samples with a higher amount of Sb incorporation. It can be seen that for the samples with Sb content of 10% and above, only a single peak is visible. The origin of these emissions is associated with band-to band (BtB) transition. However,

the samples with a lower Sb content reveal multi-peak emission (i.e. the InAs and InAs<sub>0.97</sub>Sb<sub>0.03</sub> NWs). The band gap energy of the InAsSb alloy as a function of Sb composition is expressed as [10]:

$$E_g = xE_{\text{InSb}} + (1 - x)E_{\text{InAs}} - Cx(1 - x), \quad \dots (6.1)$$

where  $x$  is the Sb composition,  $E_{\text{InAs}}$  and  $E_{\text{InSb}}$  are the bandgaps at a temperature of 10 K for InAs and InSb respectively, and  $C$  is the bowing parameter. It can be seen that the BtB related emission shows a strong red-shift with an increase in Sb composition, attributed to the bandgap shrinkage with the presence of Sb. This bandgap shrinkage is in agreement with the equation above using a bowing parameter of  $\sim 0.67$  eV [11], which is between the accepted values of 0.66 eV [12] and 0.682 eV [13]. However, for the InAsSb NWs with a high Sb composition of 19%, the PL-deduced bandgap energy is slightly lower than expected. We correlate this difference with the wider Sb fluctuation in the NWs with higher Sb incorporation; Such an Sb fluctuation within the segments could construct a slight type-II alignment, which in turn results in a transition energy that is lower than the bandgap energy of the corresponding bulk materials.

To evaluate the optical properties at a high Sb content, we also performed temperature-dependent PL for the sample InAs<sub>0.84</sub>Sb<sub>0.16</sub> NWs. Figure 6.4 shows the PL spectra measured at the evaluated temperature. Emission is visible up to 120 K. A clear red-shift is visible with increasing temperature. The peak energies  $E_p$  at different temperatures are depicted in Fig 6.9 with the corrected energy using  $k_B T / 2$  and the theoretical bandgap energy defined as:

$$E_g(T) = E_{g0} - \frac{\alpha T^2}{\beta + T} \quad \dots (6.2)$$

Where  $E_g(T)$  is the bandgap energy at 0 K, and  $\alpha$  and  $\beta$  are empirically parameters which can be considered to have linear function of  $x$ . Using 0.297 eV as  $E_{g0}$  for  $\text{InAs}_{0.84}\text{Sb}_{0.16}$ , and the experimentally determined values of  $\alpha$  and  $\beta$  for InAs and InSb [14], we found that the theoretical bandgap of  $\text{InAs}_{0.84}\text{Sb}_{0.16}$  follows  $E_g(T) = E_p - k_B T/2$ . It should be noted that the detection of emission is not possible at higher temperatures due to the weak signal.

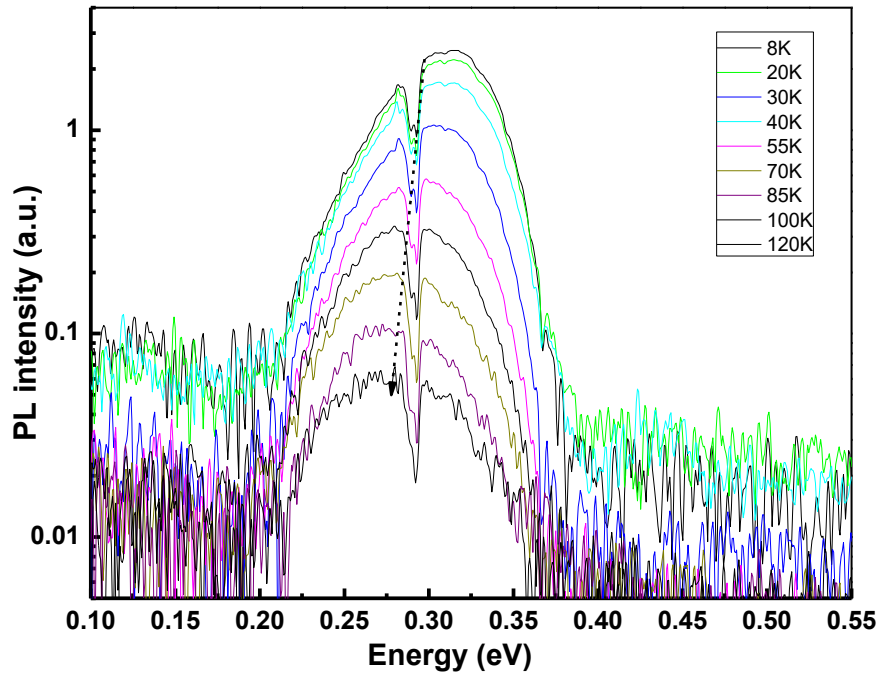


Figure 6.4: The photoluminescence of  $\text{InAs}_{0.84}\text{Sb}_{0.16}$  NWs measured at various temperatures

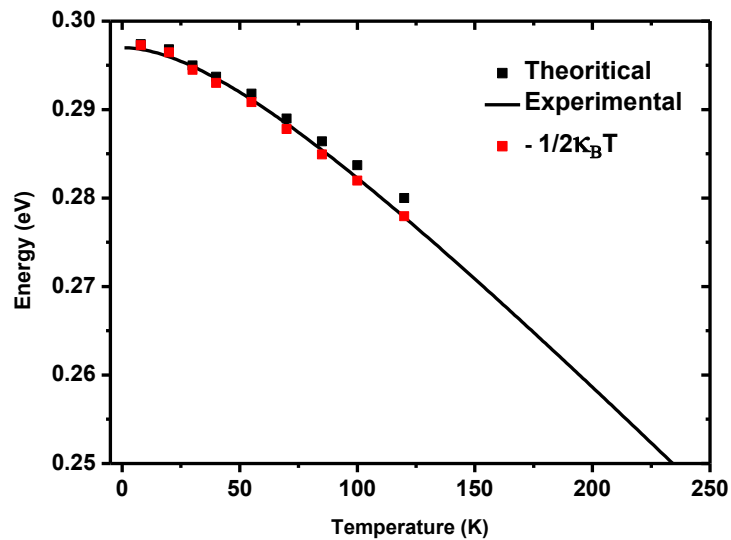


Figure 6.5: the peak energy  $E_p$ , the energy of  $E_g - k_B T/2$  and the theoretical bandgap energy

The efficient optical properties of our NWs are correlated with enhanced crystalline quality. These enhanced features belong to firstly, the contribution of Sb in the NWs and secondly to the novel droplet epitaxy growth. Q. Zhuang et al [3] proved that Sb incorporation could tune the crystal structure of InAsSb NWs via transition from polytypic into WZ dominant and to ZB dominant by increasing Sb from 4% -10%. They also confirmed that the stacking faults (SF) decrease by adding Sb even for as small as 2% of Sb composition up to 10%. SF decreased from 360/ $\mu\text{m}$  in the reference InAs sample to 200/ $\mu\text{m}$  ( $\text{InAs}_{0.98}\text{Sb}_{0.02}$ ), 100/ $\mu\text{m}$  ( $\text{InAs}_{0.96}\text{Sb}_{0.04}$ ), and finally 50/ $\mu\text{m}$  ( $\text{InAs}_{0.90}\text{Sb}_{0.10}$ ), which is consistent with report of M. Sourribes et al [15]. Secondly, improved crystal structure is attributed to the novel technique of droplet-assisted growth. It is noticeable that the PL intensity of InAsSb NWs of X=16% and 19% reduced comparing to the samples of less Sb. This means that Sb can not alter surface states or reduce it.

## **6.4 The effect of substrate doping type on 8-290K Photoluminescence of InAs NWs.**

It would be interesting to probe how the doping type of the substrate affects the behavior of the photoinduced carriers. Mid-infrared PL spectra were therefore obtained from InAs NWs. The spectra demonstrated significantly improved signal –to-noise ratio SNR in a wide temperature range of 8–290 K by using. An optimized step-scan Fourier transform infrared (FTIR) spectrometer-based modulated-PL method was used for this purpose [6, 16]. A continuous – wave laser with wavelength of 639nm, was modulated by a mechanical chopper for optical pumping and InSb detector cooled by liquid –nitrogen. The samples were mounted on the cold finger of a closed-cycle

compressor for an adjustable temperature range of 8-290 K. The laser spot is about 200 $\mu\text{m}$  in diameter. For power dependent measurements, temperature was set at 8K; the laser output power was set at 100mW for temperature dependent measurements. It was observed that the quality of the InAs NWs samples [17] and the SNR of the PL spectra are high enough to carry out a reliable quantitative PL analysis. Such an analysis revealed the origins of the PL transitions, an estimation of the non-radiative recombination rate, and the behavior of photo-induced carriers. The electron–phonon interactions were also clarified. The results showed the asymmetric nature of the ZB-on-WZ and WZ-on-ZB InAs interfaces in optical properties that deserves attention in material and device fabrication [18].

Two InAs NWs samples were grown directly on n- and p-type bare Si (111) respectively, by molecular-beam epitaxy (MBE) via an identical droplet-assisted method and are labelled hereafter as sample-N and sample-P for conciseness. Figure 6.6 shows SEM images of these samples. Both samples were grown with same growth condition and loaded together into the growth chambers. This means that they were grown under identical environment and conditions to ensure that the result is accurate enough when compare their optical properties.

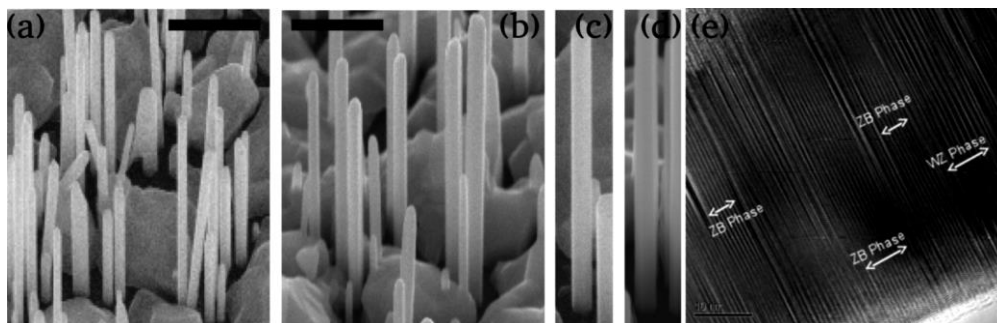


Figure 6.6 Local SEM images of sample-N (a) and sample-P (b) at a scale bar of 500 nm. Single NW manifests upright standing as in (c) and (d) for sample-N and sample-P. (e) TEM image of InAs NWs. The TEM scale bar is 10 nm.

Figure 6.7 shows temperature dependence infrared PL spectra of the sample-N and sample-P at temperatures of 8–290 K. Magnification is made for each of the spectra for intensity normalization. At 8 K, only one asymmetric PL peak shows up at about 0.415 eV for the two samples. This means the bandgap transition of the WZ InAs is not activated, as it should be at about 0.45 eV [19-21] As temperature rises up, the PL peak redshifts monotonously, which is consistent with the negative temperature coefficient of the bulk InAs bandgap [11]. At 290 K the PL intensity becomes weakened, and it reduces to about 1/70 and 1/307, respectively, of that at 8 K for the sample-N and sample-P, evidenced by the magnification. For quantitative analysis of the temperature effects, line shape fitting is performed on each of the PL spectra by a typical Lorentzian–Gaussian composite function [22-24] by which the energies, line widths, and intensities of the PL features are derived quantitatively. Representative fittings are depicted in Fig 6.8a for two temperatures of 8 and 290 K. At 8 K, a single Lorentzian–Gaussian composite function is insufficient, and a dominant feature (DF) at 0.415 eV and a low-energy feature (LEF) at around 0.401 eV are required for well reproducing the line shape. At 290 K, the fitting reveals the DF at about 0.380 eV and a high-energy feature (HEF) around 0.425 eV. The HEF is revealed by plotting the PL spectra as in Fig 6.4b in logarithmic intensity, which is obvious beyond the high energy exponential tail introduced by carriers Fermi-edge distribution [25].

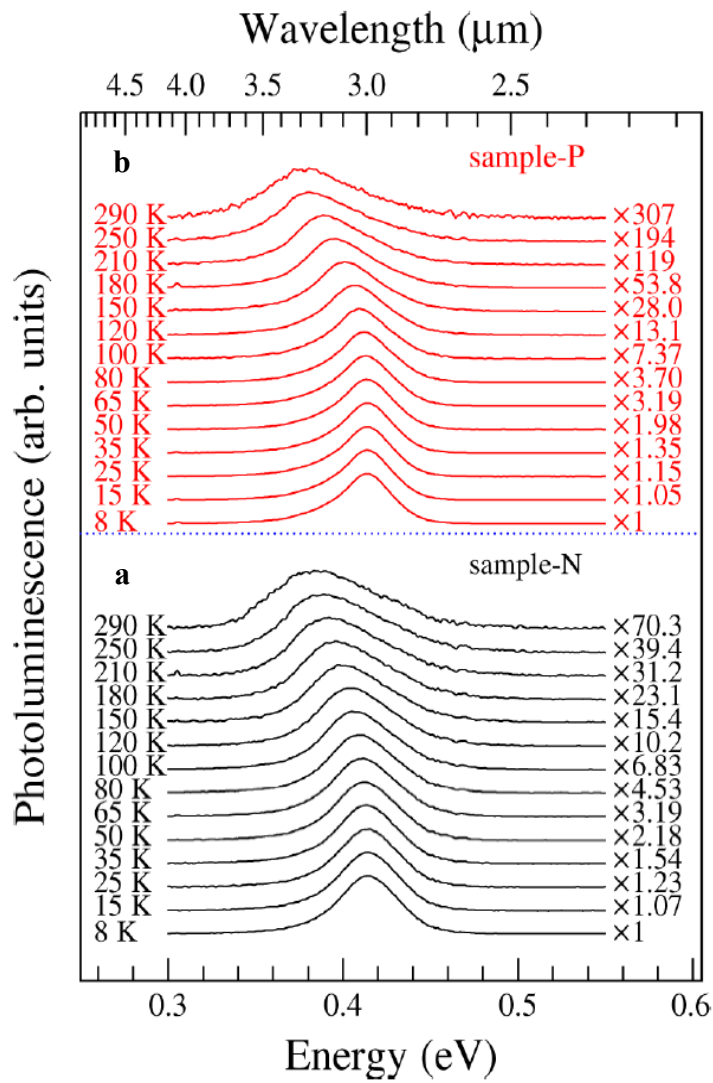


Figure 6.7: Temperature-dependent PL spectra of sample-N (a) and sample-P (b) magnified by particular factors for similar peak heights.

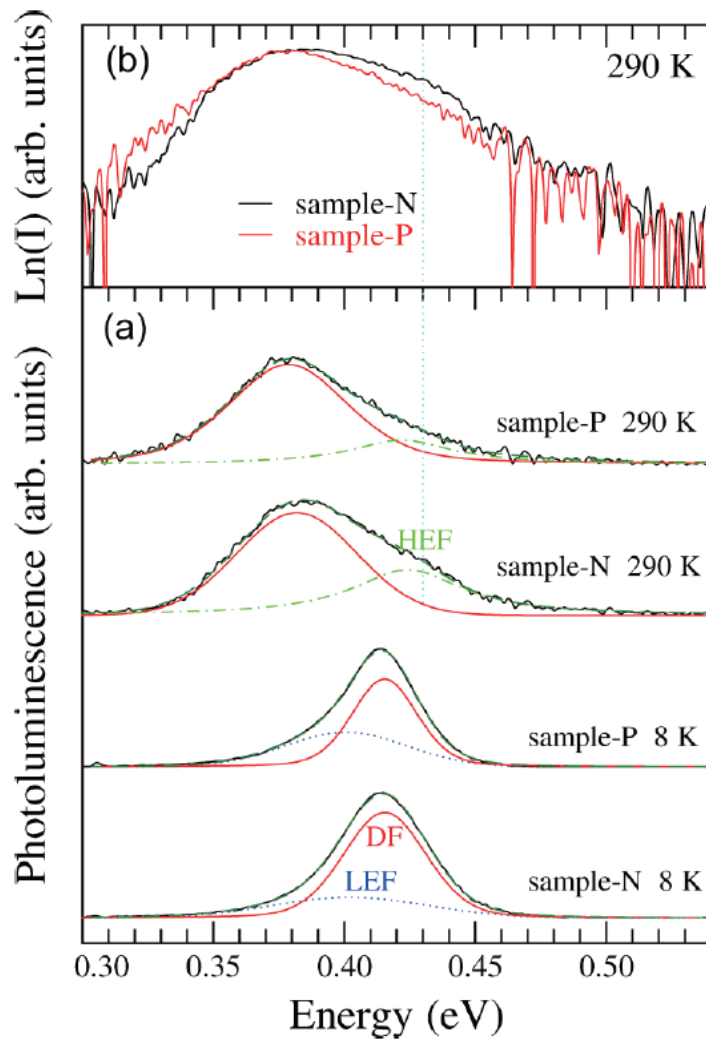


Figure 6.8: (a) Curve fittings of PL spectra for sample-N and sample-P at 8 and 290 K. (b) PL spectra of the two samples at 290 K plotted in Logarithmic intensity.

As the temperature of 290 K is high enough to depress the impurity-related transitions in InAs, the survival of Fig 6.6 Local SEM images of sample-N (a) and sample-P (b) at a scale bar of 500 nm. Single NW manifests upright standing as in (c) and (d) for sample-N and sample-P. (e) TEM image of InAs NWs. The TEM scale bar is 10 nm. The DF and HEF at 290 K indicate the two features to be of Band-to-band-like transitions.

## 6.5 PL of core-shell NWs:

Core-shell NWs have been grown to investigate how the surface passivation will improve the optical properties and to improve device performance. Figure 6.9 shows PL curves for both samples of core-shell NWs at 8k. It is clear that the PL intensity has improved dramatically comparing to that of bare NWs.

PL intensity of both InAs/AlSb core-shell NWs is two times higher than that of sample 821 (InAs). In contrast, InAs/GaSb has lower intensity and narrower FWHM than that of bare InAs NWs. Both core-shell NWs samples show red shift due to band gap shrinkage. InAs/AlSb core-shell NWs has type II bandgap whilst InAs/GaSb core-shell NWs has type III broken bandgap. Fig (6.9c) is PL Gaussian fitting of InAs/GaSb, it composed of two emission peaks, very weak one at 0.356eV (indicated as 2 in Fig 6.9c) and the dominant peak at 0.383 eV. The latter is attributed to the BtB transition. Meanwhile peak 2 is associated to defect or impurities.

In order to elucidate the optical properties of these core-shell NW ensembles, photoluminescence (PL) measurements were performed on the samples of InAs NWs and InAs/AlSb core-shell NWs at various temperatures and excitation powers, and on different positions of the samples. Temperature dependent PL spectra of InAs NWs and InAs/AlSb core-shell NWs are shown in Fig 6.10 (a) and (b), respectively. At 15 K. Both samples show a very strong PL signal, however the peak energy is below the free exciton transition energy in bulk InAs at low temperatures ( $\sim 0.415$  eV). InAs extra peak at the low energy side ( $\sim 0.380$  eV), while the InAs/AlSb NWs exhibit an asymmetric PL band with a dominant peak centred at 0.410 eV and quite symmetric PL band with a peak position at 0.391 eV. With increase of temperature, the emission peak is redshifted due to band gap shrinkage. More importantly, the PL emission persists up to room temperature. We believe the dominant

emission originates from band-to-band transition while the redshift is related to the band bending in the core InAs.

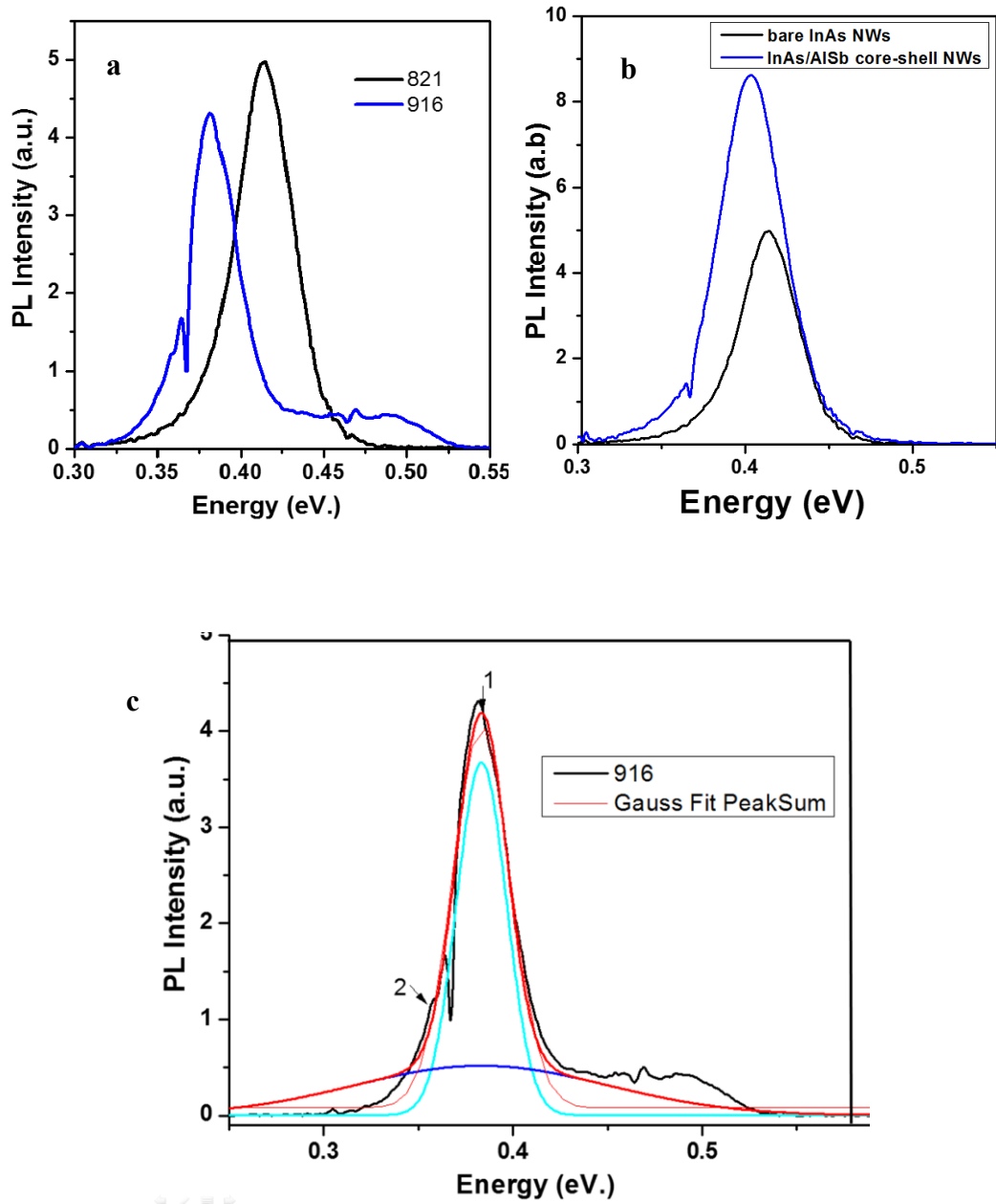


Figure 6.9 Comparison of 8K PL of a- InAs/GaSb core shell NWs and single NWs. b-InAs/AlSb core-shell NWs and single NWs.c) Gaussian fitting of InAs/GaSb core-shell NWs.

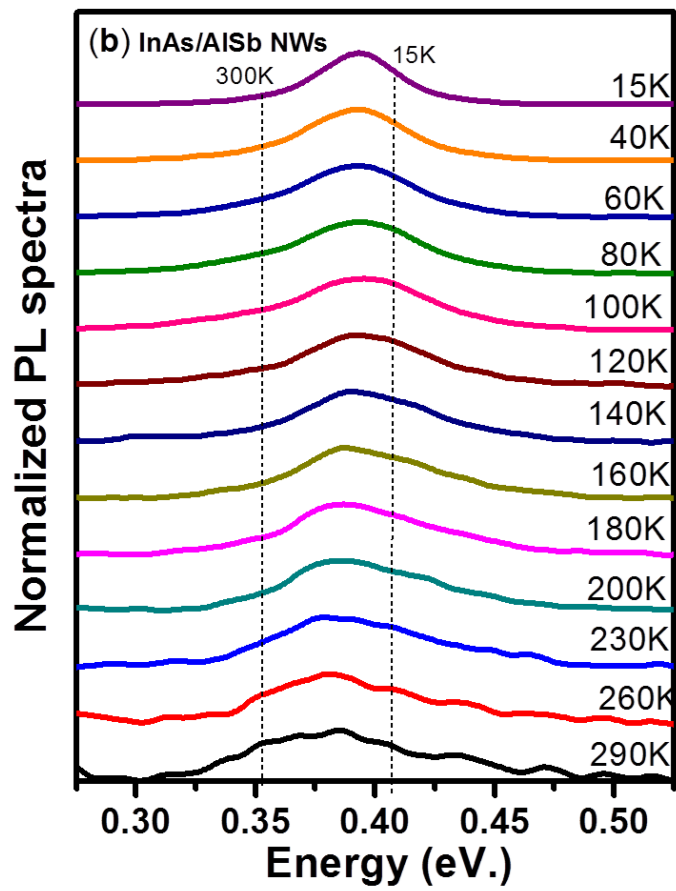
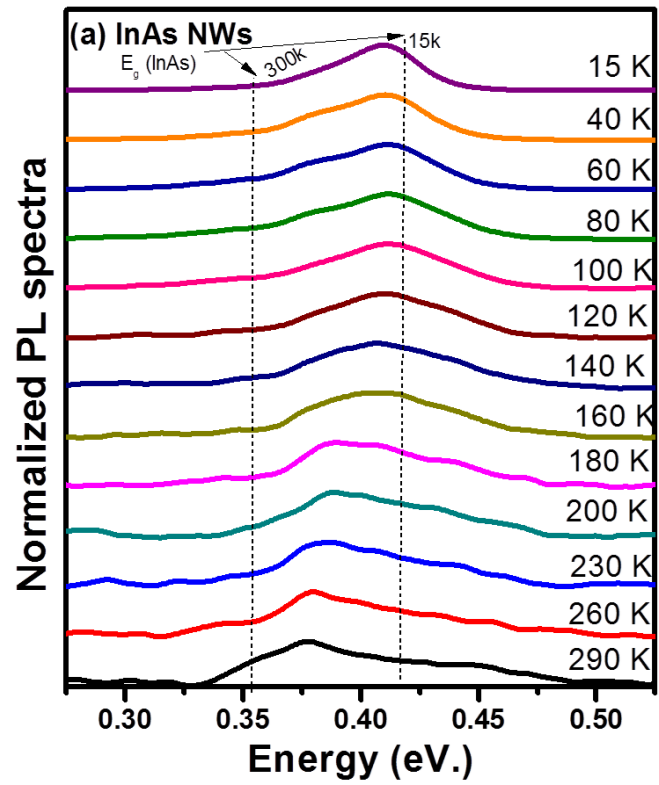


Figure 6.10: Normalized PL spectra for InAs (a) and InAs/AISb (b) NWs obtained at different temperatures. The excitation power was 10 mW and the diameter of laser spot was  $\sim 1$  mm. Vertical dashed grey lines are located at energies corresponding to InAs band gap at 15 and 300 K.

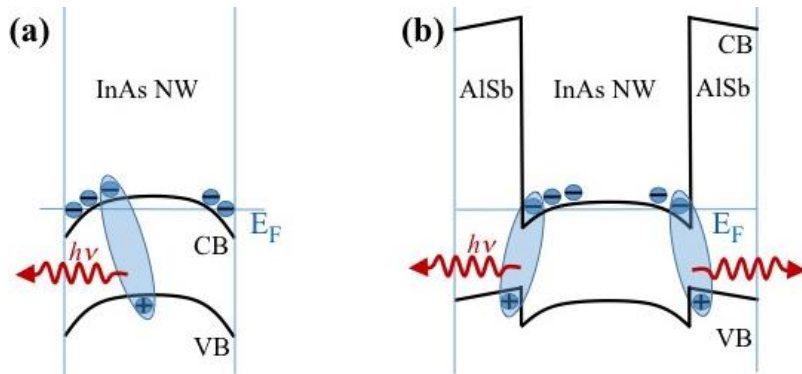


Figure 6.11: Sketch of band bending in InAs (a) and InAs/AlSb (b) NWs. n-type character of InAs material is assumed.

Figure 6.11 shows the band bending with a type II band gap alignment for InAs/AlSb interface and a valence band offset of 0.18 eV. It can be seen that for InAs NWs, the holes are depleted from the surface by a potential barrier. Due to the large band bending, the energy of band-to-band recombination in such NWs can be smaller than InAs band gap (e.g. Stark effect). For the sample of InAs/AlSb core-shell NWs, there is a type II band alignment, which separates the holes and electrons, e.g. the holes trapped in the AlSb region while the electrons remain in the InAs core region. This separation results in a reduced transition energy. Such band bending and type II alignment can also affect emission efficiency. For InAs NWs the photoexcited electron-hole pair can recombine radiatively since the photoexcited hole is separated from the surface and *n*-type carriers (electrons) could occupy surface states to suppress non-radiative recombination via surface states. For InAs/AlSb NWs the photoexcited electron-hole pair are effectively separated, e.g. holes trapped in the AlSb region while the electrons remain in the InAs core region. The separation of the surface states from the photo-excited carriers will lead to a more efficient radiative emission. We believe this feature would favour device

application of InAs/AlSb core-shell NWs in terms of photovoltaic device applications [26].

## 6.6 Summary:

To summarize, few samples of vertically aligned InAs NWs were grown by MBE on Si (111) substrates. The optical properties of our NWs were quite interesting. They had pure crystal phase and reduced stacking faults, which are attributed to the improved crystalline quality of the NWs obtained by the novel technique of droplet-assisted growth and the optimised growth conditions. Multi-peak to single peak, intensity enhancement for simple InAs NWs was observed. The effect of substrate doping type were characterized by infrared PL analysis in a wide temperature range of up to room temperature (290K). The focus of attention was the mechanisms of photoinduced carrier recombination and the effects of doping on the NWs' properties., namely the InAs NWs on p-type Si substrate manifests significantly different non-radiative recombination rate and carrier-phonon interaction in comparison with those on n-type substrate. This is because built-in electric field is generated from P- type doping of the substrate and hence leads to carriers assembling near the WZ-on-ZB interfaces. The WZ-on-ZB interface induces lower optical quality. InAsSb NWs were grown with Sb composition up to 19%. Such InAsSb NWs cover the entire mid-wavelength infrared range i.e. 3.0–5.1  $\mu\text{m}$ . We found that the higher Sb incorporation induces broader Sb fluctuations within single NWs. Nevertheless, Sb incorporation effectively improves the optical properties of the InAsSb NWs. High crystalline quality of our NWs obtained by making use of optimized droplet-assisted epitaxy should be considered novel. This advanced growth technique allowed us, for the first time, to obtain a long wavelength emission of 5.1  $\mu\text{m}$  in InAsSb NWs. The results indicate that significantly enhanced emission

efficiency can be observed in the core-shell NWs as compared to the bare InAs NWs. It had genesis in the efficient passivation of the surface states and the efficient radiative recombination induced by quantum confinement. Two samples of core-shell NWs InAs/AlSb and InAs/GaSb were grown on Si (111) substrate. Their optical properties showed dramatic enhancement in terms of PL intensity compared to that of bare InAs NWs. This improvement in PL intensity was attributed to the successful core NW passivation by shell layer.

## References

- [1] J. Shao, W. Lu, X. Lü, F. Yue, Z. Li, S. Guo, and J. Chu, "Modulated photoluminescence spectroscopy with a step-scan Fourier transform infrared spectrometer," *Review of Scientific Instruments*, vol. 77, no. 6, 2006.
- [2] J. Shao, L. Chen, W. Lu, X. Lü, L. Zhu, S. Guo, L. He, and J. Chu, "Backside-illuminated infrared photoluminescence and photoreflectance: Probe of vertical nonuniformity of HgCdTe on GaAs," *Applied Physics Letters*, vol. 96, no. 12, 2010.
- [3] Q. Zhuang, H. Alradhi, Z. Jin, X. Chen, J. Shao, X. Chen, A. M. Sanchez, Y. Cao, J. Liu, and P. Yates, "Optically efficient InAsSb nanowires for silicon-based mid-wavelength infrared optoelectronics," *Nanotechnology*, vol. 28, no. 10, pp. 105710, 2017.
- [4] Q. D. Zhuang, E. A. Anyebe, R. Chen, H. Liu, A. M. Sanchez, M. K. Rajpalke, T. D. Veal, Z. M. Wang, Y. Z. Huang, and H. D. Sun, "Sb-induced phase control of InAsSb nanowires grown by molecular beam epitaxy," *Nano letters*, vol. 15, no. 2, pp. 1109, 2015.
- [5] M. Möller, M. M. de Lima Jr, A. Cantarero, T. Chiaramonte, M. A. Cotta, and F. Iikawa, "Optical emission of inas nanowires," *Nanotechnology*, vol. 23, no. 37, pp. 375704, 2012.
- [6] M. Sun, E. Leong, A. Chin, C. Ning, G. Cirlin, Y. B. Samsonenko, V. Dubrovskii, L. Chuang, and C. Chang-Hasnain, "Photoluminescence properties of InAs nanowires grown on GaAs and Si substrates," *Nanotechnology*, vol. 21, no. 33, pp. 335705, 2010.
- [7] P. Gladkov, D. Nohavica, Z. ourek, A. P. Litvinchuk, and M. N. Iliev, "Growth and characterization of inas layers obtained by liquid phase epitaxy from bi solvents," *Semiconductor Science and Technology*, vol. 21, no. 4, pp. 544-549, 2006.
- [8] G. Koblmüller, K. Vizbaras, S. Hertenberger, S. Bolte, D. Rudolph, J. Becker, M. Döblinger, M. C. Amann, J. J. Finley, and G. Abstreiter, "Diameter dependent optical emission properties of InAs nanowires grown on Si," *Applied Physics Letters*, vol. 101, no. 5, 2012.
- [9] R. D. Grober, H. Drew, J. I. Chyi, S. Kalem, and H. Morkoc, "Infrared photoluminescence of InAs epilayers grown on GaAs and Si substrates," *Journal of applied physics*, vol. 65, no. 10, pp. 4079-4081, 1989.

- [10] S. Svensson, W. Sarney, H. Hier, Y. Lin, D. Wang, D. Donetsky, L. Shterengas, G. Kipshidze, and G. Belenky, "Band gap of  $\text{InAs}_{1-x}\text{Sb}_x$  with native lattice constant," *Physical Review B*, vol. 86, no. 24, pp. 245205, 2012.
- [11] I. Vurgaftman, J. Meyer, and L. Ram-Mohan, "Band parameters for III–V compound semiconductors and their alloys," *Journal of applied physics*, vol. 89, no. 11, pp. 5815-5875, 2001.
- [12] A. C. Farrell, W.-J. Lee, P. Senanayake, M. A. Haddad, S. V. Prikhodko, and D. L. Huffaker, "High-Quality  $\text{InAsSb}$  Nanowires Grown by Catalyst-Free Selective-Area Metal-Organic Chemical Vapor Deposition," *Nano letters*, vol. 15, no. 10, pp. 6614, 2015.
- [13] M. Yen, R. People, K. Wecht, and A. Cho, "Long-wavelength photoluminescence of  $\text{InAs}_{1-x}\text{Sb}_x$  ( $0 < x < 1$ ) grown by molecular beam epitaxy on (100)  $\text{InAs}$ ," *Applied physics letters*, vol. 52, no. 6, pp. 489-491, 1988.
- [14] Z. Fang, K. Ma, D. Jaw, R. Cohen, and G. Stringfellow, "Photoluminescence of  $\text{InSb}$ ,  $\text{InAs}$ , and  $\text{InAsSb}$  grown by organometallic vapor phase epitaxy," *Journal of Applied Physics*, vol. 67, no. 11, pp. 7034-7039, 1990.
- [15] M. Sourribes, I. Isakov, M. Panfilova, H. Liu, and P. A. Warburton, "Mobility Enhancement by Sb-mediated Minimisation of Stacking Fault Density in  $\text{InAs}$  Nanowires Grown on Silicon," *Nano Letters.*, vol. 14, no. 3, pp. 1643-1650, 2014.
- [16] D. Ercolani, M. Gemmi, L. Nasi, F. Rossi, M. Pea, A. Li, G. Salviati, F. Beltram, and L. Sorba, "Growth of  $\text{InAs}/\text{InAsSb}$  heterostructured nanowires," *Nanotechnology*, vol. 23, no. 11, pp. 115606, 2012.
- [17] P. Albert, and A. A. Harry, "Photonic design principles for ultrahigh-efficiency photovoltaics," *Nature Materials*, vol. 11, no. 3, pp. 174, 2012.
- [18] X. Chen, Q. Zhuang, H. Alradhi, Z. M. Jin, L. Zhu, X. Chen, and J. Shao, "Midinfrared Photoluminescence up to 290 K Reveals Radiative Mechanisms and Substrate Doping-Type Effects of  $\text{InAs}$  Nanowires," *Nano Letters*, vol. 17, no. 3, pp. 1545-1551, 2017.
- [19] M. Murayama, and T. Nakayama, "Chemical trend of band offsets at wurtzite/zinc-blende heterocrystalline semiconductor interfaces," *Physical Review B*, vol. 49, no. 7, pp. 4710-4724, 1994.
- [20] S. Morkotter, S. Funk, M. Liang, M. Doblinger, S. Hertenberger, J. Treu, D. Rudolph, A. Yadav, J. Becker, M. Bichler, G. Scarpa, P. Lugli, I. Zardo, J. Finley, G. Abstreiter, and G. Koblmuller, "Role of microstructure on optical properties in high-uniformity  $\text{In}_{1-x}\text{Ga}_x\text{As}$  nanowire arrays: Evidence of a wider wurtzite band gap," *Physical Review B*, vol. 87, no. 20, pp. 205303, 2013.

- [21] A. De, and C. E. Pryor, “Predicted band structures of III-V semiconductors in the wurtzite phase,” *Physical Review B*, vol. 81, no. 15, pp. 155210, 2010.
- [22] J. Shao, R. Winterhoff, A. Dörnen, E. Baars, and J. Chu, “Ordering effects on optical transitions in  $\text{Ga}_x\text{In}_{1-x}\text{P}/(\text{Al}_{0.66}\text{Ga}_{0.34})_y\text{In}_{1-y}\text{P}$  quantum wells studied by photoluminescence and reflectivity spectroscopy,” *Physical Review B*, vol. 68, no. 16, pp. 165327, 2003.
- [23] X. Chen, Y. Song, L. Zhu, S. M. Wang, W. Lu, S. Guo, and J. Shao, “Shallow-terrace-like interface in dilute-bismuth GaSb/AlGaSb single quantum wells evidenced by photoluminescence,” *Journal of Applied Physics*, vol. 113, no. 15, pp. 153505, 2013.
- [24] J. Shao, Z. Qi, H. Zhao, L. Zhu, Y. Song, X. Chen, F. X. Zha, S. Guo, and S. M. Wang, “Photoluminescence probing of interface evolution with annealing in InGa(N)As/GaAs single quantum wells,” *Journal of Applied Physics*, vol. 118, no. 16, pp. 165305, 2015.
- [25] C. Gogineni, N. A. Riordan, S. R. Johnson, X. Lu, and T. Tiedje, “Disorder and the Urbach edge in dilute bismide GaAsBi,” *Applied Physics Letters*, vol. 103, no. 4, pp. 41110, 2013.
- [26] H. Li, H. Alradhi, Z. Jin, E. A. Anyebe, A. M. Sanchez, W. M. Linhart, R. Kudrawiec, H. Fang, Z. Wang, W. Hu, and Q. Zhuang, “Novel Type- II InAs/AlSb Core– Shell Nanowires and Their Enhanced Negative Photocurrent for Efficient Photodetection,” *Advanced Functional Materials*, vol. 28, no. 8, pp. 1705382, 2018.

# Chapter 7

## InAs-based nanowire device characterisation

### 7.1 Introduction

This chapter presents several infrared (IR) photodetectors containing InAs-based NW materials. One type of device has conventional mesa structure consisting vertical InAs NW ensembles on Si substrate. The other type is based on single InAs and InAs/AlSb core-shell NW field effect transistor (NWFET) device acting as photodetectors. This chapter presents the design of the devices, the geometric features of the devices, and the basic device characterisations.

### 7.2 Conventional InAs NW ensemble photodetectors

#### 7.2.1 Device design and structure

To investigate the optoelectronic properties of as-grown NWs, InAs NW/Si infrared photodetectors with conventional geometry at various mesa diameters of 25–200  $\mu\text{m}$  were fabricated. The InAs NWs were grown on n-type Si substrate by solid-source MBE. Each mesa contains InAs NW ensembles with an estimated number of over 3000 based on the areal density. The devices were processed using standard photolithography fabrication method. Layer of SU8 was deposited by spinning to encapsulate the NWs. The SU8 was hardened in an oven. In order to expose the tips of NWs, the SU8 was thinned by reactive ion etching using a mixture of  $\text{O}_2$  and  $\text{SF}_6$  (35/5 sccm, respectively).

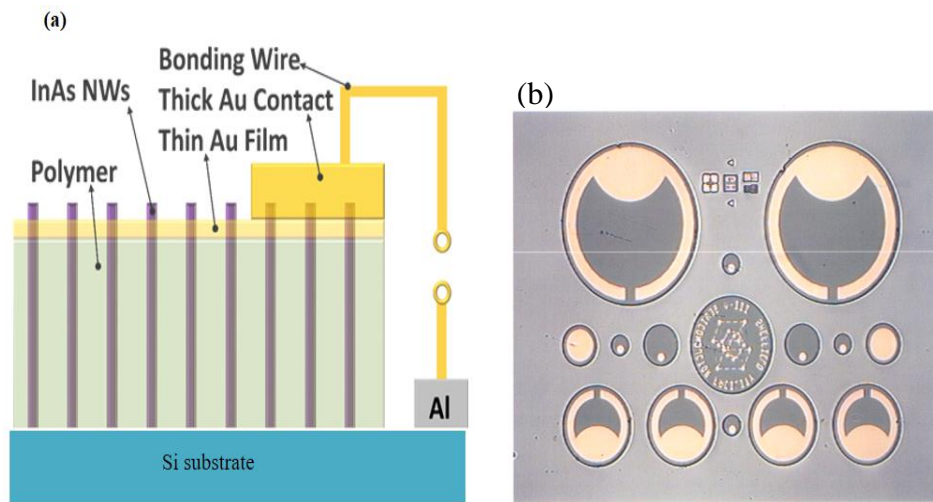


Figure 7.1: Bare InAs NWs photodetector; a) The Schematic of device design (side view). b) Microscopic image of top of the devices with different mesa sizes.

Then a thin gold layer of  $\sim 10\text{nm}$  was deposited on the exposed tips of NWs to connect all the NWs. Different circular sizes were used to define mesa size. To create electrical contacts to these devices a thicker top contact layer of Ti/Au (20/200nm) was made over specific area of the device for Ohmic contact. The back contact was formed on the back of the substrate by depositing a 200nm-thick Al layer. The schematic geometry of the device is shown in Fig 7.1a. Since our NWs was grown via self-catalyst technique, there is always height variation of the NWs. For each mesa size, we deposited different thickness of SU8, e.g. 1, 2.5 and 4.5  $\mu\text{m}$ . This method gives us the devices (with similar size) different number of NWs in the mesa with different length, e.g. thicker SU8 device has less number of NW and long length, while the thinner mesa has more number of NW with shorten length.

## 7.2.2 I-V characterization

Depending on the nature of the interface between the metal and the semiconducting NW, and the Fermi level alignment, the metal – semiconductor contact can either be Ohmic or Schottky barrier. The work function of Si is around 4.0 eV, while it is 4.9 eV for InAs. This difference between work function creates an electrostatic barrier between these two materials. This perspective leads to a downward band bending at the interface of InAs/Si that forms a depletion region for the holes as shown in Fig 7.2. Such a depletion region would enable photodetection.

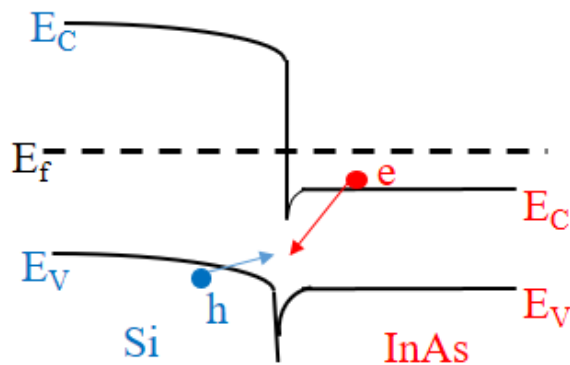


Figure 7.2: Schematic band bending of InAs/Si heterostructure

I-V characteristic of such InAs NW/Si photodetector was tested under room temperature. A typical I-V profile of such device is shown in Fig.7.3a. It can be seen that the I-V profile is very different for the devices with different SU8 thickness. There is a symmetric behavior for the devices with SU8 thicknesses less than 2.5  $\mu\text{m}$ . However, for the devices with a thickness of 4.5  $\mu\text{m}$  show a significant asymmetric I-V profile. The symmetric I-V profile reveals that the mesas having short NW with large number of NWs will not provide a rectifying function though there is a barrier formed between the InAs and the Si. While the thick mesa device shows a strong rectifying

function. We believe the major reason is due to the different number of the NWs in the mesa. It is well known that the surface states in InAs devices always give a large dark current. For the devices with short thickness, there is a large number of NWs, hence the overall dark current is large which would hide the asymmetric behaviour induced by the barrier. On the contrary, the thick mesa device contains much less number of NWs which would have much reduced dark current. In addition, the long NW in the mesa would also reduce the dark current compared to devices with short length under same

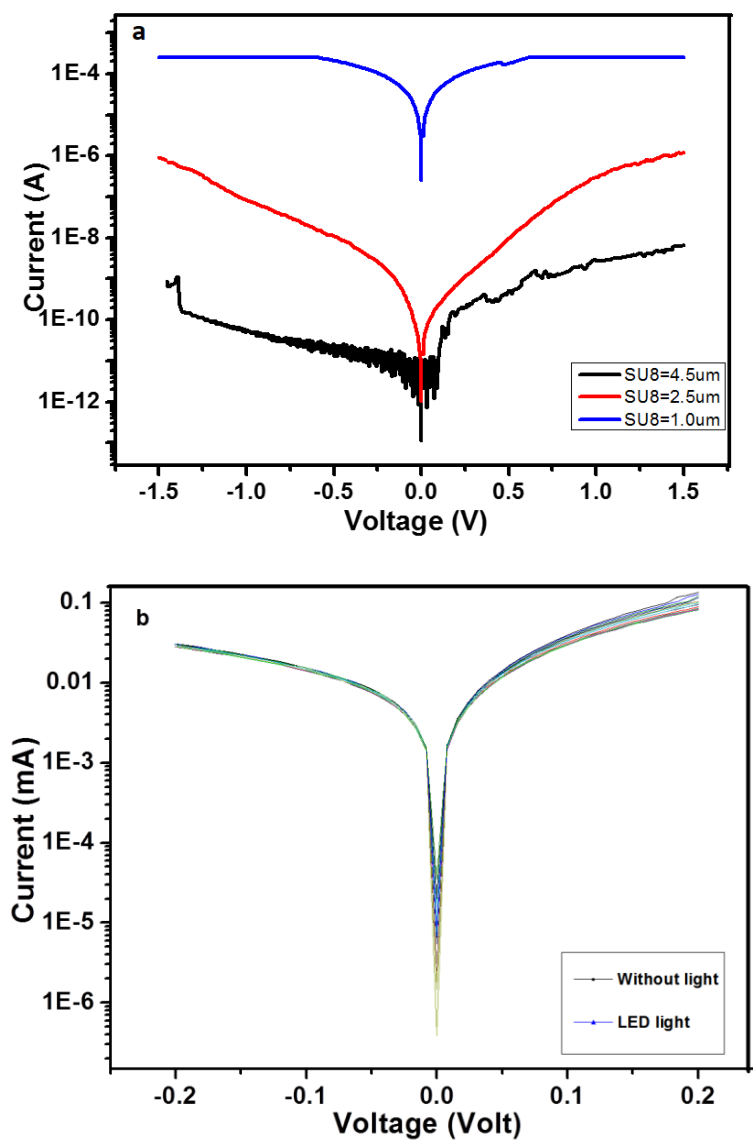


Figure 7.3: I-V profile of the devices with different a) thickness of SU8. b) light power.

external bias. Consequently, the rectifying function should be dominant in the I-V profile. This interpretation can be confirmed from the significant change of the dark current level between the devices with different thickness, e.g. thicker device has much less dark current. It arises from the difference in work function between InAs and Si as mentioned above. This means the dominant mechanism for current injection occurs via thermionic emission. This is because tunnelling current does not play an important role at room temperature especially at low doping level or high barrier. Based on the above analysis, we believe the device with 4.5  $\mu\text{m}$  thick SU8 could work as photodetector. The I-V profile of this device was characterised under illumination of LED light with a wavelength of 452 nm. Figure 7.3b illustrates the I-V curves without illumination and under LED illumination at different powers. It can be seen that under LED illumination, the larger current is present under positive bias. The incoming light is absorbed by the InAs NW, the photo-generated carrier pairs are then separated by the barrier under positive bias. While under negative bias the barrier is enlarged which will not separate the photo-generated carriers. This work indicates that the hybrid structure of InAs NW on Si has a potential to make cost-effective IR photodetectors on well-developed Si platform.

## **7.3 Single InAs and InAs/AlSb core-shell NW phototransistor**

### **7.3.1 Device design and structure**

To investigate the electrical properties and photoresponse of InAs NWs and InAs/AlSb core-shell NWs, single NW Field Effect Transistors (FETs) were fabricated on a  $p^+$ -Si/SiO<sub>2</sub> (300 nm) substrate which were operated as a phototransistor. The single NW phototransistors were fabricated using electron-

beam lithography (EBL) and followed by metallization and lift-off processes. The NWs were firstly transferred onto pre-cleaned P<sup>+</sup>-Si/SiO<sub>2</sub> (300 nm) substrates followed by spin-coated MMA and PMMA. Electron-beam lithography (JEOL 6510 with NPGS System) was used to define the source/drain (S/D) patterns. Before metallization, the NWs were dipped into a 2%HF solution for 15 s to remove the native oxide. We employed Cr/Au (20 nm/40 nm) to form Ohmic S/D electrodes. The schematic geometry of the devices is illustrated in Fig 7.4. The transport characteristics and optoelectronic measurements of the single NW photodetectors were performed on a Lake Shore TTPX Probe Station with Agilent 4155C semiconductor parameter analyzer [1].

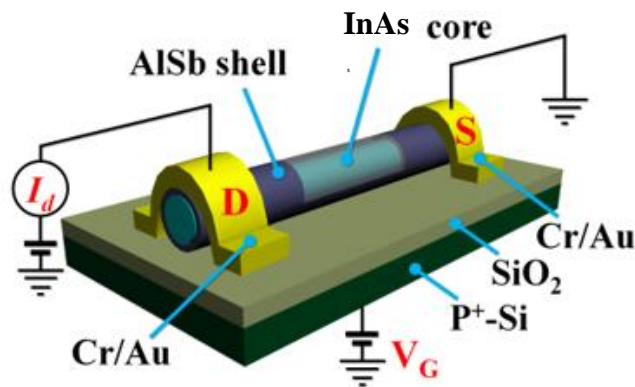


Figure 7.4: Schematic diagram of InAs/AlSb core-shell NW photodetector

### 7.3.2 Device characterization

Figure (7.5) demonstrates the drain-source voltage ( $V_d$ ) and the drain-source current ( $I_d$ ) output characteristics at various gate voltage ( $V_g$ ) of the FET devices. The gate voltage ( $V_g$ ) provides an effective tuning on the drain current as shown in Fig (7.5b).

The resulting single NW devices exhibit a typical drain-source voltage ( $V_{ds}$ ) and drain-source current ( $I_{ds}$ ) output characteristics and the gate voltage ( $V_g$ ) provides an effective tuning on the drain current (Fig 7.5).

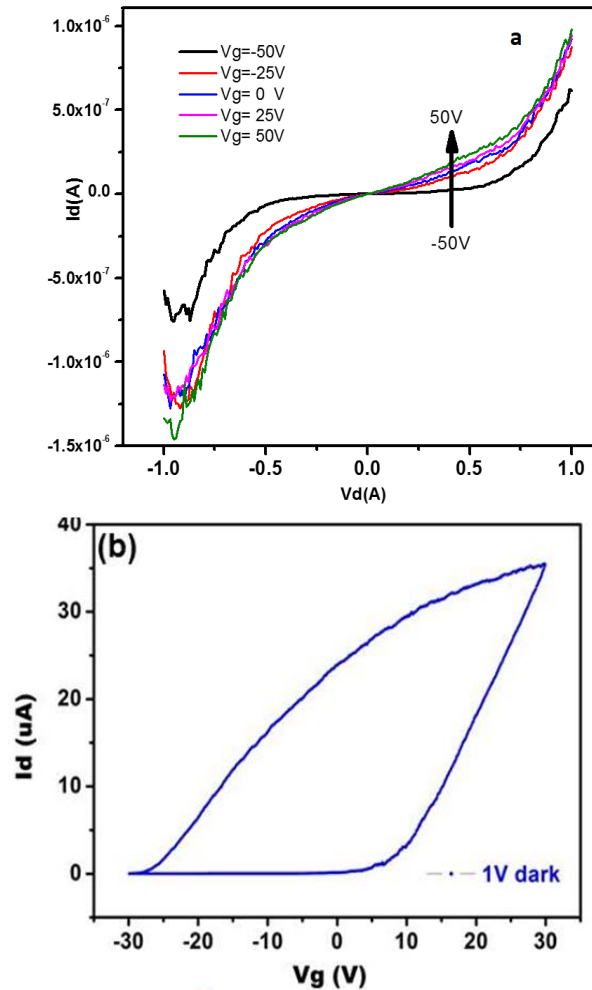


Figure 7.5: Drain voltage ( $V_d$ ) and current ( $I_d$ ) (a), and output characteristics at various gate voltage ( $V_g$ ) (b), of bare nanowire FET device.

Figure 7.6 (a) and (b) present the  $I_{ds} - V_{ds}$  characteristics of as-fabricated InAs NW transistor and InAs/AlSb core-shell NW transistor measured in ambient atmosphere, under dark and illumination with a green laser of 532 nm at power 8 mW/mm<sup>2</sup>. One interesting feature is that the core-shell NW device demonstrates a dramatically reduced dark current (2 orders of magnitude) in comparison with sample InAs NW device. Under  $V_{ds}$  of 0.1 V, the dark current reduces from  $1.5 \times 10^{-6}$  A (InAs NW device) to

$2.8 \times 10^{-8}$  A (InAs/AlSb core-shell NW device). Secondly, there is positive photocurrent  $I_{pc}$  (defined as  $I_{PC} = I_{Light} - I_{Dark}$ ) behavior in the InAs NW FETs while the core-shell NW FET demonstrates a negative photocurrent. For the InAs NW FET, when increasing the current upon light exposure ( $I_{Light}$ ) to a higher level ( $1.7 \times 10^{-6}$  A), gives a photocurrent  $I_{PC} = 0.2 \mu\text{A}$  at  $V_{gs} = 0$  V and  $V_{ds} = 0.1$  V. However, the core-shell NW FET exhibits an anomalous photocurrent behavior, e.g. upon light illumination, the  $I_{Light}$  decreases dramatically to a very low level ( $3.4 \times 10^{-9}$  A) which results in photocurrent  $I_{PC} = -24.6$  nA at  $V_{gs} = 0$  V and  $V_{ds} = 0.1$  V. The core-shell NW FET improves the signal-to-noise ratio (SNR) increases from 13% to 88% [1].

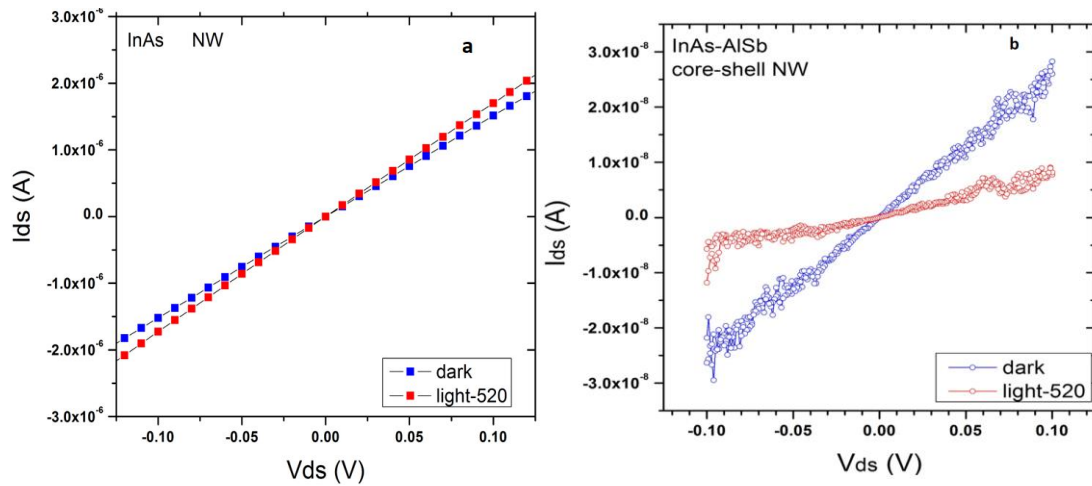


Figure 7.6: The drain current ( $I_{ds}$ ) dark current and photocurrent at different drain voltage ( $V_{ds}$ ) for a) InAs NWFET device b) an InAs/AlSb core-shell NWFET device.

The observed significantly suppressed dark current in the core-shell NW FET could be attributed to the surface passivation induced by the AlSb shell layer which has been reported in several other NW systems [2, 3]. It is believed the surface states on NW surface result in large current [4, 5], the shell layer dramatically reduces the surface states consequently results in much smaller dark current. Several other surface passivation techniques have been reported for NW devices, including surface treatment, coating with polymers etc [6-8]. Compared with these techniques, the use of core-shell

structures offers quantum-confinement and bandgap engineering that improve quantum efficiency. In addition, the in-situ growth circumvents the risk of contamination in the materials fabrication. These advances improve the sensitivity of the devices in core-shell NW FETs.

The observed anomalous photocurrent can be associated with the bandgap alignment formed between the core and the shell regions. Such behavior has been observed in several NW photodetectors. For instance, anomalous photocurrent was observed in InAs NW FETs [9] and negative photoconductance was reported in InAs NW photodetectors [10, 11]. These anomalous photo-responses were attributed to different mechanisms. Firstly, photogating effect which is associated with the trapping centers formed on the surface of the InAs NW to be filled light assisted hot electrons leading to a depletion of conduction channels [10, 12-14]. Secondly, the gas adsorption of oxygen or molecules on the surface [7], or reduced carriers mobility in the core NW region due to the increased photoexcitation scattering centers charged with hot carrier in the native oxide layer [8]. Another possible reason of getting negative photocurrent is that, the photocurrent decreases with increasing voltage due to small NWs diameter. As the surface states are very strong in thin NWs. That means when the photon incident on the NWs (device) it will generate E-h pair. Once e-h generated they recombine again due to surface states. Consequently, they will not contribute to the external current of the circuits instead; they lead to increase the dark current as they form phonons or noise inside the NWs [15].

In our devices, the core NW was passivated by a shell of AlSb, we believe that the gas adsorption has no effect (or negligible effect), so we assign the origin of the negative photocurrent to the general photogating effect and reduced mobility of the carriers in the core NW region. Both effects are associated with the carriers' separation at the

interface of the shell and the core NW induced by the type II confinement. The shell region has mixture of AlSb and oxidized AlSb. This mixture of the shell layer acting as a trapping center to the light assisted hot electrons, meanwhile, due to the type II band alignment the remaining AlSb in the shell layer also acts as a trapping centre to the holes that generated in the InAs core NW. Under illumination, the photo-generated holes will be swept into the AlSb regions in the shell layer hence attracts the electrons in the core region towards the interface between the core and the shell. In addition, some of the hot-electrons will be trapped in the shell region. This separation reduces the number of photo-generated holes in the core NW region. Meanwhile, the photo-generated electrons mobility will be reduced due to the scattering from the interface and the hole-electron pairs in the shell region. This slows down the photo-generated electrons transport in the core region. Fig 7.7 shows the trapping of shell to holes which recombine with electrons that confined in the core. In NW geometry, the diameter is extremely small in comparison with the transport length. Under light illumination (Fig 7b) electron -holes pair generated, we believe the effect of this reduction to the photocurrent is more significant compared with the increase of the overall photo-generated electrons. Together with the swept photo-generated holes in the core region, the device gives a smaller photocurrent under illumination. It should be noted that the separation of photo-generated carriers theoretically could increase the lifetime that can lead to a positive photocurrent. The anomalous photocurrent was reported in many single InAs NWs photodetectors [7, 8, 10, 11, 16] which mentioned in details in chapter 3 of this thesis. However, in our NW FET devices, the carriers transport distance ( $>3 \mu\text{m}$ ) is much larger in comparison to its diameter ( $\sim 45 \text{ nm}$ ), we believe the photogating and the mobility reduction effects would be dominant. This behavior could be maximised through engineering the bandgap at the core-shell interface by varying the

thickness and combination of different materials. Together with the significantly suppressed dark current, the type II core-shell NW structure has potential to fabricate infrared photodetectors with high detectivity on silicon platform. All the measurements of the devices are primarily, more parameters measurements of these devices are needed to be done in the future as mentioned in the future work in chapter 8 of this thesis.

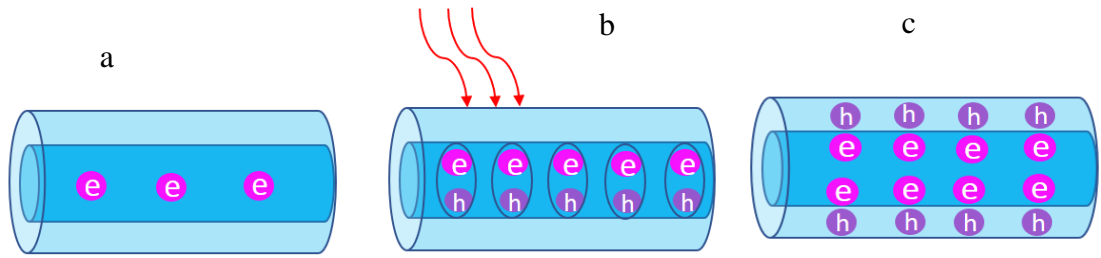


Figure 7.7: schematic diagram illustrates photogating effect. a) InAs/AlSb core-shell NWs without elimination where few electrons are in the core. b) The incident photons generate electron-hole pairs in InAs core. c) AlSb shell traps holes which recombine with electrons that are confined inside InAs. This process slows down and reduces e-h pairs that contribute to the external circuit as a result photocurrent is reduced and becomes negative.

## 7.4 Summary

In this chapter mesa device was fabricated from bare InAs NWs to act as photodetector the resultant device was proved that it is a working device despite its high dark current. The photodetection process resulted by the interfacial between InAs and Si which created barrier, which in turn separates electron in the conduction band of InAs and holes in Si valence band. When these carriers recombine, they will generate dark current, which explains the reason of getting high dark current in such device.

Single InAs photodetector was fabricated and examined to compare its performance with the photodetector of InAs/AlSb core-shell NWs. The latter exhibited lower dark current than that of bare NWs with enhanced signal to noise ratio. These enhanced properties were correlated with the eliminated surface states, which passivated by the shell layer representing by AlSb shell that wrapped InAs core

## References

- [1] H. Li, H. Alradhi, Z. Jin, E. A. Anyebe, A. M. Sanchez, W. M. Linhart, R. Kudrawiec, H. Fang, Z. Wang, W. Hu, and Q. Zhuang, "Novel Type - II InAs/AlSb Core-Shell Nanowires and Their Enhanced Negative Photocurrent for Efficient Photodetection," *Advanced Functional Materials*, vol. 28, no. 8, pp. 1705382, 2018.
- [2] Q. Hang, F. Wang, P. D. Carpenter, D. Zemlyanov, D. Zakharov, E. A. Stach, W. E. Buhro, and D. B. Janes, "Role of molecular surface passivation in electrical transport properties of InAs nanowires," *Nano letters*, vol. 8, no. 1, pp. 49, 2008.
- [3] A. Adhikari, J. K. Eliason, J. Sun, R. Bose, D. J. Flannigan, and O. F. Mohammed, "Four-dimensional ultrafast electron microscopy: Insights into an emerging technique," *ACS applied materials & interfaces*, vol. 9, no. 1, pp. 3-16, 2017.
- [4] N. Han, F. Wang, J. J. Hou, S. P. Yip, H. Lin, F. Xiu, M. Fang, Z. Yang, X. Shi, G. Dong, T. F. Hung, and J. C. Ho, "Tunable Electronic Transport Properties of Metal - Cluster - Decorated III-V Nanowire Transistors," *Advanced Materials*, vol. 25, no. 32, pp. 4445-4451, 2013.
- [5] H.-Y. Cheung, S. Yip, N. Han, G. Dong, M. Fang, Z.-X. Yang, F. Wang, H. Lin, C.-Y. Wong, and J. C. Ho, "Modulating Electrical Properties of InAs Nanowires via Molecular Monolayers," *ACS nano*, vol. 9, no. 7, pp. 7545, 2015.
- [6] J. Miao, W. Hu, N. Guo, Z. Lu, X. Zou, L. Liao, S. Shi, P. Chen, Z. Fan, J. C. Ho, T.-X. Li, X. S. Chen, and W. Lu, "Single InAs nanowire room-temperature near-infrared photodetectors," *ACS nano*, vol. 8, no. 4, pp. 3628, 2014.
- [7] Y. Han, X. Zheng, M. Fu, D. Pan, X. Li, Y. Guo, J. Zhao, and Q. Chen, "Negative photoconductivity of InAs nanowires," *Physical Chemistry and Chemical Physics*, vol. 18, no. 2, pp. 818-826, 2015.
- [8] Y. Han, M. Fu, Z. Tang, X. Zheng, X. Ji, X. Wang, W. Lin, T. Yang, and Q. Chen, "Switching from negative to positive photoconductivity toward intrinsic photoelectric response in InAs nanowire," *ACS Applied Materials and Interfaces*, vol. 9, no. 3, pp. 2867-2874, 2017.
- [9] N. Guo, W. Hu, L. Liao, S. Yip, J. C. Ho, J. Miao, Z. Zhang, J. Zou, T. Jiang, S. Wu, X. Chen, and W. Lu, "Anomalous and Highly Efficient InAs Nanowire Phototransistors Based on Majority Carrier Transport at Room Temperature," *Advanced Materials*, vol. 26, no. 48, pp. 8203-8209, 2014.

- [10] Y. Yang, X. Peng, H.-S. Kim, T. Kim, S. Jeon, H. K. Kang, W. Choi, J. Song, Y.-J. Doh, and D. Yu, "Hot Carrier Trapping Induced Negative Photoconductance in InAs Nanowires toward Novel Nonvolatile Memory," *Nano letters*, vol. 15, no. 9, pp. 5875, 2015.
- [11] H. Fang, W. Hu, P. Wang, N. Guo, W. Luo, D. Zheng, F. Gong, M. Luo, H. Tian, X. Zhang, C. Luo, X. Wu, P. Chen, L. Liao, A. Pan, X. Chen, and W. Lu, "Visible Light-Assisted High-Performance Mid-Infrared Photodetectors Based on Single InAs Nanowire," *Nano letters*, vol. 16, no. 10, pp. 6416, 2016.
- [12] J. R. Weber, A. Janotti, and C. G. Van de Walle, "Intrinsic and extrinsic causes of electron accumulation layers on InAs surfaces," *Applied Physics Letters*, vol. 97, no. 19, 2010.
- [13] Noguchi, Hirakawa, and Ikoma, "Intrinsic electron accumulation layers on reconstructed clean InAs(100) surfaces," *Physical review letters*, vol. 66, no. 17, pp. 2243, 1991.
- [14] N. Han, F. Wang, J. J. Hou, F. Xiu, S. Yip, A. T. Hui, T. Hung, and J. C. Ho, "Controllable p–n Switching Behaviors of GaAs Nanowires via an Interface Effect," *ACS Nano*, vol. 6, no. 5, pp. 4428-4433, 2012.
- [15] K. F. Brennan, *The physics of semiconductors : with applications to optoelectronic devices*, Cambridge ; New York: Cambridge University Press, 1999.
- [16] N. Guo, W. Hu, L. Liao, S. Yip, C. Ho Johnny, J. Miao, Z. Zhang, J. Zou, T. Jiang, S. Wu, X. Chen, and W. Lu, "Anomalous and Highly Efficient InAs Nanowire Phototransistors Based on Majority Carrier Transport at Room Temperature," *Advanced Materials*, vol. 26, no. 48, pp. 8203-8209, 2014.

# Chapter 8

## Conclusion

### 8.1 Summary of achievements

The key achievements of this work were as follows:

- Modifying new growth method including two-steps growth.
- Growing two structures of core-shell NWs one of them is considered as novel (InAs/AlSb) core-shell NWs as their device reduced the leakage current.
- Obtaining room temperature PL for InAs NWs.
- Obtaining long wavelength emission of 5.1  $\mu\text{m}$  from InAsSb NWs.

### 8.2 Structural and optical characterization

In this study several NW based semiconductor quantum materials were synthesised and optimised. InAs NWs were grown by innovated MBE technology with a newly developed growth technique of two-steps droplet-assisted growth. Our new modified growth involved three steps: Firstly, starting with low growth rate (0.1  $\mu\text{m}/\text{h}$ ) to enable initiating NWs. Secondly, initiating NWs. Thirdly, the growth rate ramped up to the highest value (0.3  $\mu\text{m}/\text{h}$ ). This developed growth method successfully improved NWs morphology and defect free crystal structure. Furthermore, this growth technique provides much quicker axial growth rate for the NWs. This overcomes the typical problem in the general NW growth method that requires extremely low nominal growth rate, which lead to costly and time consuming synthesis of the materials. In addition, through growth optimisation, the optical properties of our NWs were improved massively. Our technique provides a route towards cost-effective fabrication for NW

containing devices. PL intensity up to 290K was obtained for first time. PL measurements demonstrated improvement in terms of intensity peak numbers since PL became single peak after being multi-peak curve.

It is very challenging to grow InAsSb with high Sb content, which leads to the failure of NW growth with high Sb incorporating. InAsSb has been reported with 100% Sb, however, it suffered from poor crystalline quality. By using droplet-assisted epitaxy, we obtained InAsSb directly grown on Si substrate with Sb up to 19%. In our growth, we suppressed the Sb surfactant effect by optimizing flux ratio V/III to increase the Sb incorporation in the NWs. More importantly, the successfully obtained InAsSb NWs demonstrate extended PL emission wavelength up to 5.1  $\mu\text{m}$ , which is the longest wavelength, reported yet. We examined the effect of Sb composition ratio on the optical properties of InAsSb NWs by a detailed PL study. It was found that the dominant peak is BtB transition, which shows a significant red shift with increasing Sb content. We correlated this with the bandgap shrinkage with the presence of Sb. The NWs with 19% Sb has very low bandgap energy this was attributed to the fluctuation of Sb in the segment (see table 6.1), which creates type II alignment. This in turn caused a transition energy lower than the bandgap energy of the corresponding bulk materials. PL emission up to 120 °C was obtained for the sample with 16% Sb with peak energy of 0.304 eV.

Due to the large surface to volume ratio NWs suffer from surface states which negatively affect devices optical and electrical properties. One of the possible solutions for this issue is passivating NWs with different materials. In this thesis two samples of core-shell NWs were grown, InAs/AlSb core-shell NWs and InAs/GaSb core-shell NWs. The core was firstly grown at pre optimized temperature i.e. 420-500 °C, The NWs were grown for 3hrs, two hours and half for InAs/AlSb, InAs/GaSb , respectively.

Both samples were grown with 0.1  $\mu\text{m}$  /hr growth rate. After stopping the core growth, the growth temperature reduced to start growing the shell layer.

InAs/AlSb core-shell NWs has overall diameter of  $75\pm 15$  nm core width  $\sim 35$  nm, length of  $2.1\pm 1.0$   $\mu\text{m}$ , and density of  $13.3\pm 1.1 \times 10^8$   $\text{cm}^{-2}$ . The NWs exhibited two different morphologies; vertically aligned and bent NWs. The reason of bent NWs is because of non-uniform shell thickness which causes asymmetric strain distribution around the NWs which confirmed by HRTEM and EDX. X-ray diffraction showed distinct angle for the core InAs and small angle for AlSb. Temperature dependent PL 15-290K was performed at 10mW laser excitation power. The PL exhibited a strong intensity with a symmetric band. The dominant peak is about 0.391 eV and it is attributed to BtB transition. There is a slight redshift in the PL emission as temperature increases due to type II band gap alignment in this type of band alignment the carriers are separated; holes are confined in the AlSb region while electrons trapped in InAs core. This separation leads to reduction in the transition energy. This type of band alignment and shell insertion will illuminate surface states effect on the radiative recombination causing enhanced and efficient radiative emission.

InAs/GaSb core-shell NWs were also grown successfully at the growth conditions mentioned above. SEM scan demonstrated that the NW has zig-zag appearance with a tapered top with hexagonal shape. The NWs has a wide diameter of  $241.2\pm 31.7$  nm, length of  $2.0\pm 1.0$   $\mu\text{m}$  with a density of  $7.0\times 10^8$   $\text{cm}^{-2}$ . The shell of this structure is relatively thick about  $59.7\pm 14.7$  nm. Due to thick shell X-ray pattern did not reveal any presence of InAs, the XRD just showed reflection angle related to GaSb layer. HRTEM and EDX verified that the NWs have core and shell structure with hexagonal cross-section. The reason of the zig-zag shape is related to the 30 degree twisted of shell layer growth direction from  $\langle 111 \rangle_A$  to  $\langle 111 \rangle_B$ . This twisting in direction occurs due to the

fast growth rate in the  $\langle 111 \rangle_A$  direction in comparison with  $\langle 111 \rangle_B$ . PL at 8K was performed for this sample. There was a strong redshift compared to bare InAs NWs this attributed to type III bandgap. The dominant peak was associated with BtB transition. Both core-shell NWs InAs/AlSb and InAs/GaSb are dislocation free due to very low lattice mismatch between the core and the shell 1.18 % and 0.6% respectively.

### 8.3 Device characterisation

Photodetector mesa device fabricated using bare InAs NWs grown on n-type Si substrate. Ti/Au (20/200nm) was made to act as the electrodes of device for Ohmic contact. Room temperature I-V measurements demonstrated asymmetric behavior, which means that the contact is Schottky contact. Such a contact results from the difference in work function of Si 4 eV and InAs 4.9 eV. This difference in work function causes band bending in the interface of InAs/Si such a band bending causes photodetection.

Laser power dependent I-V measurements were performed. It was found that the device has high sensitivity for a small change in power. This proves that the device is a working device.

Two different photodetectors were also designed by using bare InAs NWs and InAs/AlSb core-shell NWs. The latter structures were fabricated into field effect transistor on  $P^+$ -Si/SiO<sub>2</sub> (300nm) substrate. The I-V characterisation demonstrated that core-shell NWs device has lower dark current of  $2.8 \times 10^{-8}$  A than that of bare NWs device ( $1.5 \times 10^{-6}$  A) at drain voltage of 0.1 V. Bare InAs NW device revealed positive photocurrent whilst it is negative for core-shell NW device at gate voltage of 0 V and 0.1 V drain voltage. The core-shell NW FET device exhibited high signal-to-noise ratio it increased from 13% to 88%. The reason of the enhanced parameters of the core-shell

photodetector belongs to the successful core passivation, which vanished the surface states effect.

## **8.4 Outlook and future suggestions**

In this thesis novel growth technique were modified. However, further work have to be done for samples grown by this technique e.g, structural characterizations such as HRTEM to exam the NWs crystal phase and polytypism. As well as, performing temperature dependence PL measurements to make sure that the NWs still have single peak feature.

Although core-shell NWs successfully grown and characterized, further growth is required to enhance growth quality and control shell uniformity to prevent bending in NWs. InAs/GaSb core-shell NWs need more structural investigations to determine the exact reasons of the saw-tooth shape , twisting in the shell layer and to know the the exact crystal phase.

More device measurements required to have full picture of the fabricated devices such as, I-V measurements laser and temperature dependence, spectral response, sensitivity and efficiency. As well as, fabricating new structure of photodetector NW devices for example by etching shell or design p-i-n photodetector to obtain higher, positive photocurrent. Hence, i-layer enhances light absorption or using NWs with relatively wide diameter to supress negative photocurrent phenomenon.